University of Alberta

Analysis of Displacement in an Elastic Solid with a Mode-III Crack in the Presence of Surface Elasticity

by

Tamran Hughen Lengyel

A thesis submitted to the Faculty of Graduate Studies and Research
in partial fulfillment of the requirements for the degree of

Master of Science

Department of Mechanical Engineering

Fall 2011
Edmonton, Alberta

This dissertation is dedicated to someone very special to me.

You know who you are!

Abstract

The focus of this work is the study of anti-plane deformations of an elastic solid containing a crack. A more comprehensive model of the mechanism of fracture was found by incorporating surface mechanics on the face of the crack. Included are comparisons between the refined model and the classical model with appropriate conclusions drawn about the effect of the surface on the displacement field in the entire solid.

A boundary value problem for the displacement is developed for the case when Mode-III stresses are applied. In particular it was shown that the ensuing (refined) model is well-posed. The displacement and stresses were numerically determined using various input stresses and surface parameters.

With the incorporation of surface mechanics, it is shown that the refined model is more stable and convergent than in the classical case. From the numerical solutions, approximations for adjusted deformation and stress concentration values are provided for future use.

Acknowledgements

I would like to acknowledge the following people for the various ways they propelled me to complete this work.

To my friend and mentor, Dr. Mioduchowski: Thank you for all your advice and mentoring over the years. Above all, thank you for always “keeping it real” with me.

To my supervisor, Dr. Schiavone: Thank you for your leadership, advice, high standards, tutelage and project funding. When I needed someone with authority to make things happen, you were there promptly and without question. This enabled me to focus on what matters most - the work itself.

To Dr. Nadler: Our discussions during the time you were in the department were always thought provoking. I always appreciated your first principals approach to problem modeling and numerical methods. Using the same approach has yielded a much higher quality in the formulation of this work.

To the support staff in the department office and the other graduate students: Thank you for making the everyday interactions so memorable. It was easy to stay motivated given the high standards set by those around me.

Contents

I Preliminaries 1

1 Introduction 2

1.1 Purpose . . . 2

1.2 Contribution . . . 2

2 Constitutive Models 6

2.1 Continuum Mechanics Preliminaries . . . 6

2.2 Classical Constitutive Model . . . 9

2.2.1 Body Equations . . . 9

2.2.2 Boundary Conditions . . . 10

2.3 Surface Effects . . . 11

II Problem Formulation 16

3 Mode-III Crack Problem 17

3.1 General Anti-Plane Displacement . . . 17

3.2 Classical Anti-Plane Crack Model . . . 19

3.3 Anti-Plane Shear with Surface Effects . . . 20

3.4 Uniqueness of Solution . . . 22

3.5 Normalized Problem . . . 26

4 Complex Variables Analysis 28

4.1 The Complex Plane . . . 28

4.2 Boundary Conditions . . . 30

4.3 The Hilbert Problem . . . 32

4.4 Integral Equation Formulation . . . 36

4.5 Body Displacements and Gradients . . . 40

III Solution and Results 42

5 Numerical Model 43

5.1 Numerical Integral Equation Formulation 43
5.2 Numerical Integration of Input Functions 48
5.3 Crack Face Displacement 49
5.4 Crack Face Derivatives 50
5.5 Bulk Displacement 53
5.6 Gradient in Bulk Material 55

6 Results 56

6.1 Comparison to Classical Solution ($\gamma = 0$) 56
6.2 Effect of Input Load Profiles ($\tilde{P}(x)$) 60
6.3 Effect of Surface Parameter (γ) 70
6.4 Numerical Convergence and Accuracy 87

IV Conclusions 91

7 Conclusions 92

7.1 Boundary Value Problem 92
7.2 Approximations from This Study 94
7.3 Summary of Surface Effect Model 96
7.4 Effect of Input Parameters 97

8 Suggested Future Work 98

8.1 Clamped Ends and Natural Boundary Condition 98
8.2 Realistic Values of γ for Various Materials 100
8.3 Analytical Solutions 101
8.4 Other Problems of Interest 104
8.4.1 Bonded Surface Problems 104
8.4.2 Three Dimensional Problem 105
8.4.3 Dynamic Problems 105

V References 107

List of Figures

1.1 Crack Mode Loading Types 4

2.1 Illustration of the GM model 11

3.1 Finite Body with Smooth Boundaries 23

6.1 Displacement and Slope on Crack Face, where: $\tilde{P} = -1$, $\gamma = 0$ 59
6.2 Comparison of classic anti-plane crack displacement and the numerical solution with no surface effects ($\gamma = 0$), where: $P_o = -1$ 61
6.3 Crack face displacement and slope ($\tilde{P} = -1$ and various γ) . . 62
6.4 Applied and Adjusted Input Stress ($\tilde{P} = -1$ and various γ) . . 63
6.5 Crack face displacement and slope ($\tilde{P} = x^2 - 1$ and various γ) 64
6.6 Applied and Adjusted Input Stress ($\tilde{P} = x^2 - 1$ and various γ) 65
6.7 Crack face displacement and slope ($\tilde{P} = -\frac{3\sqrt{3}}{2}x(x-1)(x+1)$ and various γ) 66
6.8 Applied and Adjusted Input Stress ($\tilde{P} = -\frac{3\sqrt{3}}{2}x(x-1)(x+1)$ and various γ) 67
6.9 Crack face displacement and slope ($\tilde{P} = x^2\,(x-1)\,(x+1)$ and various γ) 68
6.10 Applied and Adjusted Input Stress ($\tilde{P} = 4x^2\,(x-1)\,(x+1)$ and various γ) 69
6.11 Crack Face and Body Displacement ($\tilde{P} = -1+2H(x)$, $\gamma = 0.1$, $N = 128$) 71
6.12 Gradient components in body ($\tilde{P} = -1 + 2H(x)$, $\gamma = 0.1$, $N = 128$) 72
6.13 Effect of Surface Parameter (γ) on maximum crack face displacement with constant stress input ($\tilde{P} = \pm 1$). 74

6.14 Effect of Surface Effect Parameter (γ) on crack face displacement (shape) with constant stress input ($\tilde{P} = \pm 1$). 76
6.15 Plot of the inverse of maximum slope versus surface effect parameter 78
6.16 Displacement and Unit Stress Magnitude in Body Material ($\tilde{P} = -1$, $\gamma = 0$, $N = 128$) 80
6.17 Displacement and Unit Stress Magnitude in Body Material ($\tilde{P} = -1$, $\gamma = 0.5$, $N = 128$) 81
6.18 Displacement and Unit Stress Magnitude in Body Material ($\tilde{P} = -1$, $\gamma = 1$, $N = 128$) 82
6.19 Displacement and Unit Stress Magnitude in Body Material ($\tilde{P} = -1$, $\gamma = 2$, $N = 128$) 83
6.20 Effect of γ on the Stress Outside a Crack Tip 84
6.21 Curve Fit Coefficients From the Effect of γ on the Stress Outside a Crack Tip 86
6.22 Numerical Convergence With Constant Stress Input ($\tilde{P} = -1$) and various values of γ. 88
6.23 Accuracy of θ'_{max} and Convergence of θ_y on the Crack Face . 90

8.1 Plane Bonding Problems of Interest 104

List of Symbols

The defined symbols used in this work are summarized in the table below. Other symbols used in the following sections that are not summarized in this table should be considered arbitrary.

List of Symbols

Symbol	Units	Description
$\boldsymbol{x}$	m	Spacial Coordinate Vector $(= x_i \boldsymbol{e_i}, i = 1, 2, 3)$
x_1, x_2, x_3	m	Spacial Coordinate Magnitudes
$\boldsymbol{e_1}, \boldsymbol{e_2}, \boldsymbol{e_3}$	-	Unit Directional Vectors along x_1, x_2, x_3 axes
$\boldsymbol{I}$	-	Identity Tensor
∇	-	Spacial Gradient Operator
$\otimes$	-	Tensor Product Operator
δ_{ij}	-	Kronecker Delta
$Tr\left\{\boldsymbol{T}\right\}$	-	Trace of Tensor $\boldsymbol{T}$ (Sum of Diagonal Terms)
$\boldsymbol{u}$	m	Body Displacement Vector $(= u_i \boldsymbol{e_i}, i = 1, 2, 3)$
$\boldsymbol{\sigma}$	N/m^2	Cauchy Stress Tensor
$\boldsymbol{\epsilon}$	m/m	Strain Tensor
λ	N/m^2	Bulk Modulus of Body Material
μ	N/m^2	Shear Modulus of Body Material

Continued on Next Page...

List of Symbols (Continued)

Symbol	Units	Description
$\boldsymbol{n}$	-	Surface Normal Vector
$\boldsymbol{t}$	N/m^2	Input Traction Vector ($= \boldsymbol{\sigma n}$)
w	m	Anti-Plane Displacement Magnitude ($\equiv u_3(x_1, x_2)$)
a	m	Half Crack Length
$\boldsymbol{P}$	-	Tangential Projection Tensor
$\boldsymbol{S}$	J/m^2	Stress Tensor in Surface Material
$\boldsymbol{\epsilon}^s$	m/m	Strain Tensor in Surface Material
∇_s	-	Surface Gradient Operator
λ^s	J/m^2	Modified Surface Material Bulk Modulus
μ^s	J/m^2	Modified Surface Material Shear Modulus
σ_0	J/m^2	Material Surface Tension
α	J/m^2	Surface Effect Constant ($\equiv \lambda^s + \sigma_0$)
β	J/m^2	Surface Effect Constant ($\equiv \mu^s - \sigma_0$)
$\hat{h}$	m	Interface Layer Thickness
P	N/m^2	Input Mode-III Stress on Crack ($= \sigma_{23}$)
P_o	N/m^2	Root Mean Squared Value of Input Stress on Crack
$\tilde{P}$	-	Normalized Input Stress on Crack ($= P/P_o$)
ζ_1, ζ_2	-	Integrated Input Stress Functions
x, y	-	Normalized Planar Coordinates ($= x_1/a, x_2/a$)
ϑ	m	Stress Parameter ($= aP_o/\mu$)
γ	-	Surface Parameter ($= \beta/a\mu$)
u	-	Unit Anti-Plane Displacement ($= w/\vartheta$)
z	-	Complex Number Coordinate ($= x + iy$)

Continued on Next Page...

List of Symbols (Continued)

Symbol	Units	Description
$\mathfrak{Re}\{F(z)\}$	-	Real Part of Complex Function $F(z)$
$\mathfrak{Im}\{F(z)\}$	-	Imaginary Part of Complex Function $F(z)$
$\phi(z)$	-	Complex Anti-Plane Displacement Function ($u(x,y) = \mathfrak{Re}\{\phi(z)\}$)
$\theta(x)$	-	Unit Crack Face Anti-Plane Displacement ($= u(x, 0^+)$)
$\theta_y(x)$	-	Unit Crack Face Adjusted Input Stress ($= \tilde{P}(x) - \gamma\theta''(x)$)
$\theta_o(x)$	-	Unit Crack Face Anti-Plane Displacement With No Surface Effects
e	-	Element Index ($1 \leq e \leq N$)
$\theta^e(x)$	-	Discretized Anti-Plane Displacement on Crack Face for Element e
$M_n^e(x)$	-	The n^{th} Lagrange Interpolation Function for Element e
$\psi_n^e(x)$	-	The n^{th} Logarithmic Integral Function for Element e
$H_n^e(x)$	-	The n^{th} Logarithmic Interpolation Function for Element e
N	-	Number of Elements Used in Discretization
h_e	-	Element Length ($\equiv \mathrm{x}_{e+1} - \mathrm{x}_e$)
G	-	Gauss Points for Numerical Integration
$\boldsymbol{\Theta}$	-	Subspace Approximation Vector for $\theta(x)$

Continued on Next Page. . .

List of Symbols (Continued)

Symbol	Units	Description
Θ_n	-	Components for Subspace Approximation Vector $\boldsymbol{\Theta}$ $(1 \le n \le N+1)$
$\boldsymbol{\Theta}'$	-	Subspace Approximation for $\theta'(x)$
Θ'_n	-	Components for Subspace Approximation Vector $\boldsymbol{\Theta}'$ $(1 \le n \le N+1)$
$\mathbf{x}$	-	Subspace Discretization Locations for $\boldsymbol{\Theta}$ and $\boldsymbol{\Theta}'$
x_n	-	Components for Subspace Approximation Vector $\mathbf{x}$ $(1 \le n \le N+1)$
$\boldsymbol{\Theta}''$	-	Finite Difference Subspace Approximation for $\theta''(x)$
Θ''_n	-	Components for Subspace Approximation Vector $\boldsymbol{\Theta}''$ $(1 \le n \le N)$
$\mathbf{x}'$	-	Subspace Discretization Locations for $\boldsymbol{\Theta}''$
x'_n	-	Components for Subspace Approximation Vector $\mathbf{x}'$ $(1 \le n \le N)$
τ	-	Unit Shear Stress Magnitude ($= \lvert\nabla u\rvert$)
$\overline{R}$	-	Unit Radius of Effect
R_s	m	Radius of Effect ($= a\overline{R}$)
Υ, Υ'	%	Refinement Parameters (Desired Accuracy) for $\theta(x)$ and $\theta'(x)$
$\tilde{\varepsilon}, \tilde{\varepsilon}'$	%	Computed Accuracy for $\theta(x)$ and $\theta'(x)$

Part I

Preliminaries

1 - Introduction

1.1 Purpose

The purpose of this work was to study surface layer effects on an elastic solid. In order to quantify these effects a Mode-III stress, anti-plane crack problem was formulated from both the classical constitutive model and one using a different surface material description from the body material. Well-posedness of the refined model is proven and the differences between displacements and stresses from the two models are quantified. In addition, numerical convergence and stability was studied for both models, showing that the refined model was more convergent and stable than the Classical model.

1.2 Contribution

The classical constitutive model for displacements under load in an isotropic solid has been well studied and details can be found in the works of Chou and Pagano [1], Sokolnikoff [2], Love [3], Gurtin [4], England [5] amongst others. The classical constitutive model (summarized in Section 2.2) yields reasonable results for smooth boundaries with small (linearized) displacements. However, when the surface curvature becomes high or boundaries lack smoothness (for example cusps or crack tips), singularities in both stress and strain are found. These singularities are not physically realistic and call for model refinement.

Surface energy models merge nano-molecular effects into the standard constitutive model and provide a path forward utilizing standard continuum mechanics theory. Extensive work has been done using surface effect models and a comprehensive summary has been published by Wang et. al [6].

The Gurtin and Murdoch model of surface elasticity [7, 8] (GM model) allows such a merging of nano-molecular effects of the boundary surface material into the classical continuum mechanics model. This method has grown in popularity in the last decade, as can be seen in the works by Kim et. al [9, 10, 11], Sharma et. al [12], Vardoulakis [13] and Antipov [14]. A simplified interpretation of the GM model will be presented in Section 2.3.

In order to keep things manageable, the focus of this study was on the effect of the GM model on a linear, planar crack with Mode-III loading. The three types of stress modes on cracks are shown in Figure 1.1 [15]. Mode-I and Mode-II loading (Figures 1.1a and 1.1b respectively) give in-plane displacements, where Mode-III loading (Figure 1.1c) yields anti-plane (perpendicular to the plane) [16] displacements. In this work, Mode-III loads and anti-plane displacement as shown in Figure 1.1c were only considered.

In Section 3.1, the general assumptions for anti-plane displacement are reviewed. Section 3.2 provides a formulation from first principals of the classical anti-plane displacement boundary value problem with a straight crack in an infinite plane. Section 3.3 provides a refined formulation of the anti-plane displacement problem utilizing the GM model discussed in Section

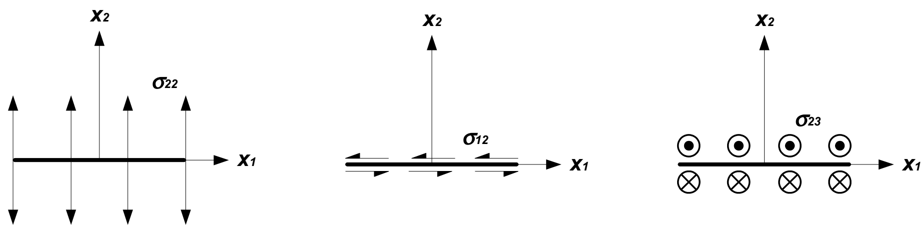

(a) Mode-I (in plane) (b) Mode-II (in plane) (c) Mode-III (anti-plane)

Figure 1.1: Crack Mode Loading Types

2.3. A comparison shows that the GM model collapses to the classical case when the surface effects are eliminated. The proof of uniqueness for the solution of the refined boundary value problem with surface effects is given in Section 3.4. An equivalent non-dimensional problem is formulated in Section 3.5, where a linear boundary value problem with just one constant (the surface parameter) emerges.

Since the two problems formulated in Chapter 3 are planar, complex variable analysis can be used to formulate a one dimensional problem on the crack face. A summary of the applicable complex variable rules and assumptions utilized are given in Section 4.1. Application of these assumptions to the boundary conditions of the formulated anti-plane displacement problem are given in Sections 4.2 and 4.3. This application leads to three single variable integral equations [17, 18, 19] for displacement and gradient components on the crack face (Section 4.4). A formulation (in the form of a complex Cauchy Integral [20, 21]) for the displacement and gradient components in the body material is outlined in Section 4.5.

Chapter 5 provides an outline of the numerical method used to solve the integral equations derived in Chapter 4. Section 5.1 provides a numerical formulation for solving the general form of a Fredholm Equation of the Second Kind [22, 17, 18, 23], and Section 5.2 outlines a procedure for numerically integrating the input stress functions. Using these foundations, numerical approximations of the anti-plane displacement and gradient components (which are linearly related to the stresses) on the crack face are outlined in Sections 5.3 and 5.4 respectively. Formulations for numerical approximation of the displacement and gradients inside the body material are given in Sections 5.5 and 5.6.

The numerical model was tested using different input stress functions and surface parameters. The analytical solution to the classic case is formulated in Section 6.1 and comparisons to the numerical results with surface parameters eliminated shows that the formulated solution in this work collapses to the classical case. The effect of different input stress functions across the crack face is discussed in Section 6.2. Generalizations and approximations of displacement and opposing shear stress versus the surface parameter via curve fitting are provided in Section 6.3. These approximations can be used as "quick check" adjustment equations for future use. A brief discussion of accuracy and refinement convergence of the numerical model is outlined in Section 6.4 and it was determined that the model was finite, convergent and stable for resultant displacement and opposing shear stress.

Chapter 7 provides some distinct conclusions from this study. The model presented in this work is proven well posed, and provides finite and stable results. This gives leeway to some future problems of related interest and potential refinements of this work in Chapter 8.

2 - Constitutive Models

2.1 Continuum Mechanics Preliminaries

In the following sections, it will be assumed that standard, linear Continuum Mechanics rules apply. A deeper review can be found in any text on the subject [4, 24]. A summary of the continuum mechanics rules, assumptions and notation related to this work is summarized in the following statements.

1. All vector spaces are assumed linear.

2. Unless otherwise stated, all vector and tensor components in this work are Cartesian.

3. Unless otherwise stated, Indicial/Einstein Summation Notation [4, 24] shall be assumed everywhere. Given this, summation symbols ($\sum$) may be omitted when summation is required.

4. The transpose [4] of any tensor ($\boldsymbol{A}$) is defined by the relation:

$$\boldsymbol{a} \cdot \boldsymbol{A}\boldsymbol{b} = \boldsymbol{b} \cdot \boldsymbol{A}^T\boldsymbol{a} \tag{2.1.1}$$

   Where $\boldsymbol{a}$ and $\boldsymbol{b}$ are arbitrary, constant vectors.

5. The Tensor Product operator ($\otimes$) has the following property for any set of vectors ($\boldsymbol{a}, \boldsymbol{b}, \boldsymbol{c}$):

$$(\boldsymbol{a} \otimes \boldsymbol{b})\, \boldsymbol{c} = (\boldsymbol{b} \cdot \boldsymbol{c})\, \boldsymbol{a} \tag{2.1.2}$$

6. Any vector ($\boldsymbol{v}$) or tensor ($\boldsymbol{A}$) field can be expressed in cartesian coordinates as:

$$\boldsymbol{v} \equiv v_i \boldsymbol{e_i}, \qquad i = 1, 2, 3 \tag{2.1.3}$$

$$\boldsymbol{A} \equiv A_{ij} \boldsymbol{e_i} \otimes \boldsymbol{e_j}, \qquad i, j = 1, 2, 3 \tag{2.1.4}$$

Where: the vector $\boldsymbol{e_i}$ is the unit directional vector along the positive x_i axis; and v_i, A_{ij} represent the components of the vector ($\boldsymbol{v}$) and tensor ($\boldsymbol{A}$) respectively.

7. The Identity Tensor ($\boldsymbol{I}$) is defined as:

$$\boldsymbol{I} \equiv \delta_{ij} \boldsymbol{e_i} \otimes \boldsymbol{e_j}, \qquad i, j = 1, 2, 3 \tag{2.1.5}$$

And the Kronecker delta function (δ_{ij}) is defined as:

$$\delta_{ij} \equiv \begin{cases} 1, & i = j \\ 0, & i \neq j \end{cases} \qquad i, j = 1, 2, 3 \tag{2.1.6}$$

8. The Spacial Gradient Operator in cartesian coordinates is defined as:

$$\nabla \equiv \frac{\partial}{\partial x_i} \boldsymbol{e_i}, \qquad i = 1, 2, 3 \tag{2.1.7}$$

And the gradient of any scalar (f) or vector ($\boldsymbol{v}$) follows the differential relations:

$$df \equiv \nabla f \cdot d\boldsymbol{x} \tag{2.1.8}$$

$$d\boldsymbol{v} \equiv (\nabla \boldsymbol{v})\, d\boldsymbol{x} \tag{2.1.9}$$

Hence, the gradients of any scalar (f) or vector ($\boldsymbol{v}$) in cartesian coordinates is:

$$\nabla f = \left(\frac{\partial f}{\partial x_i}\right) \boldsymbol{e_i}, \qquad i = 1, 2, 3 \tag{2.1.10}$$

$$\nabla \boldsymbol{v} = \left(\frac{\partial v_i}{\partial x_j}\right) \boldsymbol{e_i} \otimes \boldsymbol{e_j}, \qquad i, j = 1, 2, 3 \tag{2.1.11}$$

9. The divergence ($\text{div}(*) \equiv \nabla \cdot (*)$) of any vector ($\boldsymbol{v}$) or tensor ($\boldsymbol{A}$) field has the following properties:

$$\nabla \cdot \boldsymbol{v} = Tr\left\{\nabla \boldsymbol{v}\right\} \tag{2.1.12}$$

$$\boldsymbol{a} \cdot (\nabla \cdot \boldsymbol{A}) = \nabla \cdot \left(\boldsymbol{A}^T \boldsymbol{a}\right) \tag{2.1.13}$$

Where: $\boldsymbol{a}$ is any arbitrary, constant vector; and the the trace ($Tr\left\{\boldsymbol{A}\right\}$) is defined as the sum of the diagonal components, or:

$$Tr\left\{\boldsymbol{A}\right\} \equiv \sum_{i=1}^{3} \sum_{j=1}^{3} A_{ij}\delta_{ij} = A_{ij}\delta_{ij} = A_{ii}, \qquad i = 1, 2, 3 \tag{2.1.14}$$

So, the divergence of any vector ($\boldsymbol{v}$) or tensor ($\boldsymbol{A}$) in cartesian coordinates is:

$$\nabla \cdot \boldsymbol{v} = \frac{\partial v_i}{\partial x_i}, \qquad i = 1, 2, 3 \tag{2.1.15}$$

$$\nabla \cdot \boldsymbol{A} = \frac{\partial A_{ij}}{\partial x_j} \boldsymbol{e_i}, \qquad i, j = 1, 2, 3 \tag{2.1.16}$$

Using these basic rules, the constitutive relations in the following sections can be utilized.

2.2 Classical Constitutive Model

2.2.1 Body Equations

The linearized constitutive model for the static deformation of an isotropic solid in three dimensions is [1, 4, 2, 24, 5]:

$$\boldsymbol{\epsilon} = \frac{1}{2}\left(\nabla \boldsymbol{u} + (\nabla \boldsymbol{u})^T\right) \tag{2.2.1}$$

$$\boldsymbol{\sigma} = \lambda Tr\left\{\boldsymbol{\epsilon}\right\} \boldsymbol{I} + 2\mu\boldsymbol{\epsilon} \tag{2.2.2}$$

$$\nabla \cdot \boldsymbol{\sigma} + \boldsymbol{b} = \boldsymbol{0} \tag{2.2.3}$$

Equations 2.2.1 and 2.2.2 represent the definitions of strain ($\boldsymbol{\epsilon}$) and Cauchy Stress ($\boldsymbol{\sigma}$) tensors respectively for linear deformation of an isotropic solid. Equation 2.2.3 represents a force balance anywhere in the body material. In these equations: $\boldsymbol{u}$ is the displacement vector of the body, and $\boldsymbol{b}$ represents the externally applied body forces. Note that:

$$\boldsymbol{\epsilon} = \frac{1}{2}\left(\nabla \boldsymbol{u} + (\nabla \boldsymbol{u})^T\right) = \frac{1}{2}\frac{\partial u_i}{\partial x_j}\left(\boldsymbol{e_i} \otimes \boldsymbol{e_j} + \boldsymbol{e_j} \otimes \boldsymbol{e_i}\right)$$

So:

$$Tr\left\{\boldsymbol{\epsilon}\right\} = \frac{1}{2}\left(Tr\left\{\frac{\partial u_i}{\partial x_j}\boldsymbol{e_i} \otimes \boldsymbol{e_j}\right\} + Tr\left\{\frac{\partial u_i}{\partial x_j}\boldsymbol{e_j} \otimes \boldsymbol{e_i}\right\}\right) = \sum_{i=1}^{3}\frac{\partial u_i}{\partial x_i} = \nabla \cdot \boldsymbol{u}$$

Therefore, in terms of displacement ($\boldsymbol{u}$), the Cauchy Stress Tensor is:

$$\boldsymbol{\sigma} = \lambda\left(\nabla \cdot \boldsymbol{u}\right)\boldsymbol{I} + \mu\left[\nabla \boldsymbol{u} + (\nabla \boldsymbol{u})^T\right] \tag{2.2.4}$$

Further simplification yields the Cauchy Stress Tensor components (in Cartesian):

$$\sigma_{ij} = \lambda \left(\sum_{k=1}^{3} \frac{\partial u_k}{\partial x_k} \right) \delta_{ij} + \mu \left[\frac{\partial u_i}{\partial x_j} + \frac{\partial u_j}{\partial x_i} \right], \qquad i, j = 1, 2, 3 \tag{2.2.5}$$

Given 2.2.4:

$$\begin{aligned} \nabla \cdot \boldsymbol{\sigma} &= \nabla \cdot \left(\lambda \left(\nabla \cdot \boldsymbol{u} \right) \boldsymbol{I} + \mu \left[\nabla \boldsymbol{u} + \left(\nabla \boldsymbol{u} \right)^T \right] \right) \\ &= \lambda \nabla \left(\nabla \cdot \boldsymbol{u} \right) + \mu \nabla \cdot \left(\nabla \boldsymbol{u} \right) + \mu \nabla \cdot \left(\nabla \boldsymbol{u} \right)^T \end{aligned}$$

Which yields the following equations for body deflection:

$$(\lambda + \mu) \frac{\partial^2 u_i}{\partial x_j \partial x_i} + \mu \frac{\partial^2 u_i}{\partial x_j^2} + b_i = 0, \qquad i, j = 1, 2, 3 \tag{2.2.6}$$

2.2.2 Boundary Conditions

The boundary conditions are determined by assuming a prescribed stress vector ($\boldsymbol{t}$), which has the surface force balance:

$$\boldsymbol{t} = \boldsymbol{\sigma} \boldsymbol{n} \tag{2.2.7}$$

Where $\boldsymbol{n}$ is the surface normal vector of a boundary curve ($f(x_1, x_2, x_3)$) and is defined by:

$$\boldsymbol{n} \equiv \frac{\nabla f}{|\nabla f|} = n_i \boldsymbol{e_i}, \qquad i = 1, 2, 3 \tag{2.2.8}$$

Using Equations 2.2.5 and 2.2.7, the stress vector has the following components:

$$t_i = \left[\lambda \left(\sum_{k=1}^{3} \frac{\partial u_k}{\partial x_k} \right) \delta_{ij} + \mu \left(\frac{\partial u_i}{\partial x_j} + \frac{\partial u_j}{\partial x_i} \right) \right] n_j, \qquad i, j = 1, 2, 3 \tag{2.2.9}$$

The quantities t_i in Equation 2.2.9 are then equated to the known, applied stress vector components on the surface to get the boundary condition equations.

2.3 Surface Effects

The classical model in Section 2.2 does not take into account atom interaction on the material surface. When the ratio between surface area and material volume increases these interactions become more dominant and the physics requires an adjustment. Atomic interactions are incorporated into the GM model as a thin surface layer on the free boundary under some initial surface tension. The assumption is that this layer has behavior similar to a surface tension on water [7], or a thin layer of netting or tape that disperses energy on the boundary. A visual illustration of this idea is shown in Figure 2.1.

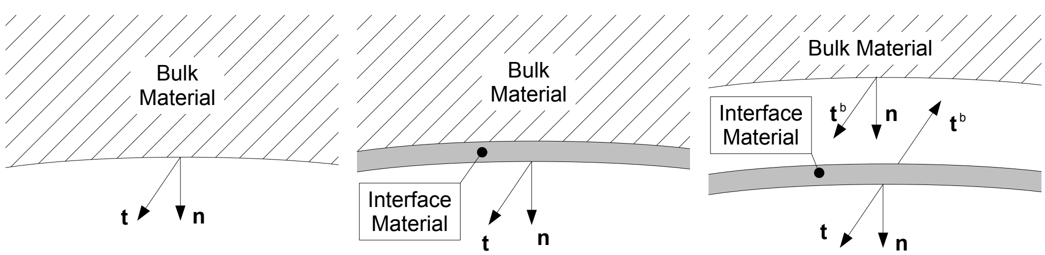

(a) Traction applied directly to material surface. Without surface effects, this defaults to the classical model.

(b) Interface material with a thin surface layer under tension with external traction unchanged.

(c) Adjusted traction on body surface from force balance across interface layer material ($\boldsymbol{t}^b = \boldsymbol{t} - \boldsymbol{t}^s$).

Figure 2.1: Illustration of the GM model

Figure 2.1a shows traction on the boundary with surface effects ignored, which is the classical model from Section 2.2. The traction applied to the boundary is direct with no energy dispersion from surface effects. When the boundary curvature is moderate, then this model is well accepted. Figure

2.1b shows the boundary with a thin surface layer with energy dissipation [7, 11, 12]. When the curvature of the boundary becomes more extreme, this thin layer will have a more pronounced effect [8, 11].

Figure 2.1c shows the force balance across this interface layer, where the surface stress on the bulk material boundary is reduced due to absorption of surface energy from the boundary layer. Denote this reduction as $\boldsymbol{t}^s$ (the surface effect adjustment). Since the interface material layer behaves like a "coating" under pre-stress, the adjustment required on the input load can by quantified by "projecting" this interface layer upon the bulk surface boundary with adjusted tangential surface traction. Given this, the GM model is constructed with the assumption that this interface layer only has a surface tangential component [7], hence lies in "tangent space" with no surface normal properties ($\boldsymbol{t}^s \cdot \boldsymbol{n} = 0$). The Tangential Projection Tensor ($\boldsymbol{P}$) - which can be used to project any vector or tensor field this tangent space - is defined as [12]:

$$\boldsymbol{P} \equiv \boldsymbol{I} - \boldsymbol{n} \otimes \boldsymbol{n} \tag{2.3.1}$$

Where $\boldsymbol{n}$ is the normal vector of the material surface. Note that regardless of the coordinate system, $\boldsymbol{P} = \boldsymbol{P}^T = \boldsymbol{P}^2$. Using the Tangential Projection Tensor, the Surface Gradient [7, 12, 11] operator is defined as:

$$\nabla_s(*) = \nabla(*)\boldsymbol{P} \tag{2.3.2}$$

Therefore the "Surface Divergence" of any vector ($\boldsymbol{v}$) or tensor ($\boldsymbol{T}$) field has the following properties [7, 8, 12, 11]:

$$
\begin{aligned}
\nabla_s \cdot \boldsymbol{v} &= Tr\left\{\nabla_s \boldsymbol{v}\right\} \\
\boldsymbol{a} \cdot \left(\nabla_s \cdot \boldsymbol{T}\right) &= \nabla_s \cdot \left(\boldsymbol{T}^T \boldsymbol{a}\right)
\end{aligned}
\tag{2.3.3}
$$

Where $\boldsymbol{a}$ is any arbitrary, constant vector. Because the interfacial stress tensor ($\boldsymbol{S}$ - a symmetric tensor for isotropic materials) is an absorbtion of surface energy due to tension, it must be tangential to the material surface (or, resides in Tangent Space). So, $\boldsymbol{S}$ is required to have the following property [7]:

$$
\boldsymbol{S}\boldsymbol{n} = \mathbf{0} \tag{2.3.4}
$$

Assuming an isotropic material with small (linear) deformations, then applying a force balance across the material sufrace/interface material layer yeilds [7, 8, 12, 11]:

$$
[\boldsymbol{\sigma}\boldsymbol{n}] + \nabla_s \cdot \boldsymbol{S} = \mathbf{0} \tag{2.3.5}
$$

Where: $[\boldsymbol{\sigma}\boldsymbol{n}]$ denotes the jump in traction across the interface material, or alternatively, the adjusted value of traction on the boundary. So, Equation 2.3.5 has the equivalent form as a function of the adjusted boundary traction on the body ($\boldsymbol{t}^b$) and the externally applied boundary traction ($\boldsymbol{t}$), being:

$$
\boldsymbol{t}^b = \boldsymbol{t} - \nabla_s \cdot \boldsymbol{S} \tag{2.3.6}
$$

Here: $\boldsymbol{t}^b$ represents the adjusted surface traction, $\boldsymbol{t}$ represents the externally applied traction (without surface effects) and $\nabla_s \cdot \boldsymbol{S}$ ($= \boldsymbol{t}^s$ from Figure 2.1c) represents the surface effect adjustment due to the surface energy dispersion. This adjustment is always tangent to the boundary normal with surface tension on the interface material, which translates as a reduction of shear stress on the body surface. For an isotropic solid with "small" (linear) deformations, the interface material has a stress tensor in the form [12, 11].

$$\boldsymbol{S} = (\sigma_o + (\lambda^s + \sigma_o)\, Tr\, \{\boldsymbol{\epsilon}^s\})\, \boldsymbol{P} + 2\, (\mu^s - \sigma_o)\, \boldsymbol{\epsilon}^s \tag{2.3.7}$$

Where σ_o represents an interfacial "surface tension" of the interface material with units J/m^2. The modified Lame's constants (μ^s and λ^s) have the same units of σ_o and have the transformations [12]:

$$\mu^s = \mu\hat{h} \tag{2.3.8}$$

$$\lambda^s = \frac{2\lambda\mu\hat{h}}{\lambda + \mu} \tag{2.3.9}$$

Where $\hat{h}$ is the average thickness of the assumed interface layer. Sharma et. al have worked this out to be between 1 and 2 lattice spacings (usually measured in Angstrom) [12]. If the surface effect constants α and β are defined as:

$$\alpha \equiv \lambda^s + \sigma_o \tag{2.3.10}$$

$$\beta \equiv \mu^s - \sigma_o \tag{2.3.11}$$

Using Equations 2.3.10 and 2.3.11, Equation 2.3.7 has the simplified form:

$$\boldsymbol{S} = (\sigma_o + \alpha Tr\, \{\boldsymbol{\epsilon}^s\})\, \boldsymbol{P} + 2\beta\boldsymbol{\epsilon}^s \tag{2.3.12}$$

Given that the interface material and body surface are considered "compliant" in the constitutive model [7, 8], the strains must be equivalent. However, the strain tensor must also be projected to tangent space to give a material strain tensor ($\boldsymbol{\epsilon}^s$) and has the relation to the body strain tensor ($\boldsymbol{\epsilon}$) through the following projection relation [12, 11, 10, 9]:

$$\boldsymbol{\epsilon}^s = \boldsymbol{P}\boldsymbol{\epsilon}\boldsymbol{P} \tag{2.3.13}$$

To use this model, the body displacement in the body (bulk) material follows the same relations as Section 2.2.1, however the boundary conditions must be adjusted using Equations 2.3.6, 2.3.12 and 2.3.13.

Part II

Problem Formulation

3 - Mode-III Crack Problem

3.1 General Anti-Plane Displacement

Anti-plane displacement is the displacement component along the x_3 axis (u_3) as a function of the planar coordinates x_1 and x_2 [16]. The main assumption used in the following problem formulations is that the planar displacement components (u_1 and u_2) are much smaller in magnitude than the anti-plane displacement (u_3) magnitude. So the problem is simplified by assuming $u_1, u_2 \simeq 0$. Define (for convenience) the anti-plane displacement magnitude $u_3 \equiv w = w(x_1, x_2)$. The normal vector (from Equation 2.2.8) of any boundary in the plane then becomes a function of the planar coordinates such that:

$$\boldsymbol{n} = n_1 \boldsymbol{e_1} + n_2 \boldsymbol{e_2} \tag{3.1.1}$$

Using the assumptions above along with Equation 2.2.6, anti-plane displacement in the body material follows Laplace's Equation in the plane:

$$\frac{\partial^2 w}{\partial x_1^2} + \frac{\partial^2 w}{\partial x_2^2} = 0 \tag{3.1.2}$$

The Cauchy Stress and Strain Tensors defined in Equations 2.2.2 and 2.2.1 respectively for anti-plane displacement are:

$$\boldsymbol{\epsilon} = \frac{1}{2}\left[\frac{\partial w}{\partial x_1}\left(\boldsymbol{e_1}\otimes\boldsymbol{e_3}+\boldsymbol{e_3}\otimes\boldsymbol{e_1}\right)+\frac{\partial w}{\partial x_2}\left(\boldsymbol{e_2}\otimes\boldsymbol{e_3}+\boldsymbol{e_3}\otimes\boldsymbol{e_2}\right)\right] \tag{3.1.3}$$

$$\boldsymbol{\sigma} = \mu\left[\frac{\partial w}{\partial x_1}\left(\boldsymbol{e_1}\otimes\boldsymbol{e_3}+\boldsymbol{e_3}\otimes\boldsymbol{e_1}\right)+\frac{\partial w}{\partial x_2}\left(\boldsymbol{e_2}\otimes\boldsymbol{e_3}+\boldsymbol{e_3}\otimes\boldsymbol{e_2}\right)\right] \tag{3.1.4}$$

Given Equations 3.1.3 and 3.1.4, the relation to stress and strain tensors for the anti-plane case simplifies to:

$$\boldsymbol{\sigma} = 2\mu\boldsymbol{\epsilon} \tag{3.1.5}$$

Where the only components of stress and strain in the anti-plane case are:

$$\sigma_{13} \equiv \mu\frac{\partial w}{\partial x_1} \qquad \sigma_{23} \equiv \mu\frac{\partial w}{\partial x_2} \tag{3.1.6}$$

$$\epsilon_{13} \equiv \frac{1}{2}\frac{\partial w}{\partial x_1} \qquad \epsilon_{23} \equiv \frac{1}{2}\frac{\partial w}{\partial x_2} \tag{3.1.7}$$

Using Equations 2.2.9, 3.1.1 and 3.1.4 the anti-plane traction vector is:

$$\boldsymbol{t} = \mu\left(\frac{\partial w}{\partial x_1}n_1+\frac{\partial w}{\partial x_2}n_2\right)\boldsymbol{e_3} = \mu\left(\nabla w\cdot\boldsymbol{n}\right)\boldsymbol{e_3} = \mu\frac{\partial w}{\partial \boldsymbol{n}}\boldsymbol{e_3} \tag{3.1.8}$$

Anti-plane displacement with Mode-III loads also have the property that [16]:

$$w^+ = -w^- \tag{3.1.9}$$

Where the positive ($w^+ = w(x_1, x_2)$) and negative ($w^- = w(x_1, -x_2)$) regions of the body are given the superscript (+) and (−) respectively. From this, a result which will be useful later is:

$$\frac{\partial^n w^+}{\partial x_1^n} = -\frac{\partial^n w^-}{\partial x_1^n}, \qquad n > 1 \tag{3.1.10}$$

$$\frac{\partial^n w^+}{\partial x_2^n} = (-1)^{n+1}\frac{\partial^n w^-}{\partial x_2^n}, \qquad n > 1 \tag{3.1.11}$$

3.2 Classical Anti-Plane Crack Model

Assume a straight crack along the x_1-axis of length $2a$ and centered at the origin defined by L, such that:

$$L \in x_1, x_2 = [-a, a], 0^{\pm} \tag{3.2.1}$$

It shall also be assumed that the crack size is significantly smaller than the body material extents, and therefore the plane can be assumed infinitely large. The normal vector on the crack face (L) becomes:

$$\boldsymbol{n}^{\pm} = \mp \boldsymbol{e_2} \tag{3.2.2}$$

The Stress Vector (from Equation 3.1.8) along the crack face is:

$$\boldsymbol{t}^{\pm} = \mp \mu \frac{\partial w}{\partial x_2}^{\pm} \boldsymbol{e_3}, \qquad \text{on } L \tag{3.2.3}$$

The prescribed Mode-III stress loading on the crack line shall be defined as:

$$\sigma_{23}(x_1, 0^{\pm}) \equiv P(x_1) \tag{3.2.4}$$

So the surface traction from Equation 3.2.3 also has the form:

$$\boldsymbol{t}^{\pm} = \mp P(x_1) \boldsymbol{e_3}, \qquad \text{on } L \tag{3.2.5}$$

Using Equations 3.2.3 and 3.2.5, the classical case for anti-plane shear has the boundary condition on the crack face (L):

$$\mu \frac{\partial w}{\partial x_2}^{\pm} = P(x_1), \qquad \text{on } L \tag{3.2.6}$$

For simplicity, it shall also be assumed that there is no stress at the extents of the plane or externally applied inside the body material ($\therefore \boldsymbol{b} = \boldsymbol{0}$). This leads to the classical anti-plane displacement boundary value problem, given by Equations 3.2.7 through 3.2.9.

$$\frac{\partial^2 w}{\partial x_1^2} + \frac{\partial^2 w}{\partial x_2^2} = 0 \qquad \text{in } \mathbb{R}^2 \backslash L \tag{3.2.7}$$

$$\mu \frac{\partial w}{\partial x_2}^{\pm} = P(x_1) \qquad \text{on } L \tag{3.2.8}$$

$$\left| \frac{\partial w}{\partial \boldsymbol{n}} \right| \to 0 \qquad \text{as } |\boldsymbol{x}| \to \infty \tag{3.2.9}$$

3.3 Anti-Plane Shear with Surface Effects

Assuming the same input loading and crack geometry as the classical case in Section 3.2, then the Projection Tensor from Equation 2.3.1 becomes:

$$\boldsymbol{P} = \boldsymbol{e_1} \otimes \boldsymbol{e_1} + \boldsymbol{e_3} \otimes \boldsymbol{e_3} \tag{3.3.1}$$

Using Equations 3.1.3 and 3.3.1, the surface material strain tensor from Equation 2.3.13 is:

$$\boldsymbol{\epsilon}^s = \frac{1}{2} \frac{\partial w}{\partial x_1} \left(\boldsymbol{e_1} \otimes \boldsymbol{e_3} + \boldsymbol{e_3} \otimes \boldsymbol{e_1} \right) \tag{3.3.2}$$

Note that the surface strain ($\boldsymbol{\epsilon}^s$) in Equation 3.3.2 has no diagonal terms ($\therefore Tr \left\{ \boldsymbol{\epsilon}^s \right\} = 0$), hence the Surface Strain tensor from Equation 2.3.12 for an anti-plane crack is:

$$\boldsymbol{S} = \sigma_o \left(\boldsymbol{e_1} \otimes \boldsymbol{e_1} + \boldsymbol{e_3} \otimes \boldsymbol{e_3} \right) + \beta \frac{\partial w}{\partial x_1} \left(\boldsymbol{e_1} \otimes \boldsymbol{e_3} + \boldsymbol{e_3} \otimes \boldsymbol{e_1} \right) \tag{3.3.3}$$

It is worthwhile to note the differences (and similarities) between the surface stress tensor in Equation 3.3.3 ($\boldsymbol{S}$) and the bulk material stress tensor in Equation 3.1.4 ($\boldsymbol{\sigma}$). The two major differences are that the normal components (in the direction of $\boldsymbol{e_2}$) for $\boldsymbol{\sigma}$ are eliminated and replaced with a tangential and uniform surface tension (σ_o). In this particular case (for an anti-plane crack), the two tensors are merely joined by the projection relation similar to the strain tensor relation, but with an added surface tension:

$$\boldsymbol{S} = \boldsymbol{P}\left(\sigma_o \boldsymbol{I} + \frac{\beta}{\mu}\boldsymbol{\sigma}\right)\boldsymbol{P} \tag{3.3.4}$$

Using Equation 2.3.3, the surface divergence of $\boldsymbol{S}$ simplifies to:

$$\nabla_s \cdot \boldsymbol{S} = \beta \frac{\partial^2 w}{\partial x_1^2}\boldsymbol{e_3} \tag{3.3.5}$$

The force balance from Equation 2.3.6 yields the adjusted boundary conditions with surface effects:

$$\boldsymbol{t}^b = \boldsymbol{t} - \beta \frac{\partial^2 w}{\partial x_1^2}\boldsymbol{e_3}$$

With the same prescribed traction along the crack as in Equation 3.2.4 the adjusted boundary conditions with surface effects on the crack face (L) is:

$$\mu \frac{\partial w}{\partial x_2}^{\pm} = P(x_1) \mp \beta \frac{\partial^2 w}{\partial x_1^2}^{\pm}, \qquad \text{on } L \tag{3.3.6}$$

This leads to the boundary value problem for anti-plane displacement with surface effects, given by Equations 3.3.7 through 3.3.9.

$$\frac{\partial^2 w}{\partial x_1^2} + \frac{\partial^2 w}{\partial x_2^2} = 0 \qquad \text{in } \mathbb{R}^2 \backslash L \tag{3.3.7}$$

$$\mu \frac{\partial w}{\partial x_2}^{\pm} = P(x_1) \mp \beta \frac{\partial^2 w}{\partial x_1^2}^{\pm} \qquad \text{on } L \tag{3.3.8}$$

$$\left|\frac{\partial w}{\partial \boldsymbol{n}}\right| \to 0 \qquad \text{as } |x| \to \infty \tag{3.3.9}$$

The problem definition above is identical to the classic case (Equations 3.2.7 through 3.2.9) with exception of the surface effect. Note that when the surface constant $\beta \to 0$, the problem in Equations 3.3.7 through 3.3.9 collapses to the classic case.

3.4 Uniqueness of Solution

The difference between two separate solutions of the boundary value problem in Equations 3.3.7 through 3.3.9 is defined as:

$$v(x_1, x_2) \equiv w_2(x_1, x_2) - w_2(x_1, x_2) \tag{3.4.1}$$

This yields the zero-stress problem for $v(x_1, x_2)$ given by:

$$\frac{\partial^2 v}{\partial x_1^2} + \frac{\partial^2 v}{\partial x_2^2} = 0 \qquad \text{in } \mathbb{R}^2 \backslash L \tag{3.4.2}$$

$$\mu \frac{\partial v}{\partial x_2}^{\pm} = \mp \beta \frac{\partial^2 v}{\partial x_1^2}^{\pm} \qquad \text{on } L \tag{3.4.3}$$

$$\left|\frac{\partial v}{\partial \boldsymbol{n}}\right| \to 0 \qquad \text{as } |\boldsymbol{x}| \to \infty \tag{3.4.4}$$

Given that the geometry of the crack tips $(x_1, x_2 = \pm a, 0)$ is only piecewise continuous, the derivatives there are indeterminate. This lack of smoothness gives rise to debate about the surface energies there and poses issues with uniqueness. However, methods by Krutitskii [25, 26] and Knowles [27] provide insight. Using these methods, begin by redefining the geometry of the problem.

Consider a finite planar area (B) of radius R that encompasses a "smooth" inner boundary ($\partial\Omega$) around the crack at a distance defined as ε ($a+\varepsilon \ll R$). A visualization is shown in Figure 3.1.

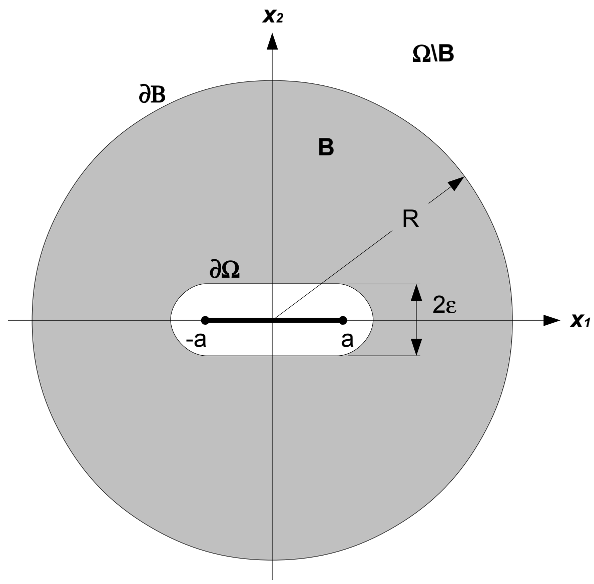

Figure 3.1: Finite Body with Smooth Boundaries

The boundary of the outer circular area and inner area encompassing the crack are denoted by ∂B and $\partial\Omega$ respectively. The extents of the plane is denoted by $\partial\Omega_\infty$, which represents the limit as $|x| \to \infty$ (or $\mathbb{R}^2$). Define the values of v on the boundary of $\partial\Omega$ to be:

$$v_\varepsilon^\pm \equiv v(x_1, \pm\varepsilon) \qquad \text{on } \partial\Omega_{1,2}, \tag{3.4.5}$$

$$v_r \equiv v(\mp a + \varepsilon\cos(\varphi), \varepsilon\sin(\varphi)) \qquad \text{on } \partial\Omega_{3,4} \tag{3.4.6}$$

Where: $\partial\Omega_1$ and $\partial\Omega_2$ are the upper ($x_2 = +\varepsilon$) and lower ($x_2 = -\varepsilon$) portions of the straight part of $\partial\Omega$ respectively ($\partial\Omega_{1,2} \in x_1 = [-a, a], x_2 = \pm\varepsilon$); $\partial\Omega_3$ ($\pi/2 \leq \varphi \leq 3\pi/2$) and $\partial\Omega_4$ ($-\pi/2 \leq \varphi \leq \pi/2$) are the left and right curved portions of $\partial\Omega$ respectively (in cylindrical coordinates) and the boundary

$\partial\Omega = \bigcup_{i=1}^{4} \partial\Omega_i$. Using this geometry, Green's 1st Identity [18] yields:

$$\int_B |\nabla v|^2 \, dA = \oint_{\partial B} v \frac{\partial v}{\partial \boldsymbol{n}} ds - \oint_{\partial\Omega} v \frac{\partial v}{\partial \boldsymbol{n}} ds \tag{3.4.7}$$

Given 3.4.4, it must hold that $v = O\left(R^{-1}\right) + C_\infty$ (C_∞ is a constant) as $R \to \infty$. Hence, $\frac{\partial v}{\partial \boldsymbol{n}} = O\left(R^{-2}\right)$ as $R \to \infty$. Therefore:

$$\lim_{R\to\infty} \oint_{\partial B} v \frac{\partial v}{\partial \boldsymbol{n}} ds = \int_0^{2\pi} \left[O\left(R^{-1}\right) + C_\infty\right]\left[O\left(R^{-2}\right)\right] R d\theta = 0$$

Where: $B \to \Omega$ as $R \to \infty$. Using this result along with Equations 3.2.2, 3.4.5 and 3.4.6, then Equation 3.4.7 becomes:

$$\begin{aligned}
\int_\Omega |\nabla v|^2 \, dA &= -\oint_{\partial\Omega} v \frac{\partial v}{\partial \boldsymbol{n}} ds = -\sum_{i=1}^{4} \int_{\partial\Omega_i} v \frac{\partial v}{\partial \boldsymbol{n}} ds \\
&= -\int_{-a}^{a} v_\varepsilon^+ \left(\nabla v_\varepsilon^+ \cdot (-\boldsymbol{e_2})\right)(-dx_1) - \int_{-a}^{a} v_\varepsilon^- \left(\nabla v_\varepsilon^- \cdot \boldsymbol{e_2}\right) dx_1 \\
&\quad - 2\varepsilon \int_{-\frac{\pi}{2}}^{\frac{\pi}{2}} v_r \left(\nabla v_r \cdot (-\boldsymbol{e_r})\right) d\theta \\
&= -\int_{-a}^{a} v_\varepsilon^+ \frac{\partial v_\varepsilon}{\partial x_2}^+ dx_1 - \int_{-a}^{a} v_\varepsilon^- \frac{\partial v_\varepsilon}{\partial x_2}^- dx_1 + 2\varepsilon \int_{-\frac{\pi}{2}}^{\frac{\pi}{2}} v_r \frac{\partial v_r}{\partial r} d\theta \\
&= -I_1 - I_2 + 2\varepsilon I_3
\end{aligned}$$

The integrals I_1 and I_2 are determined using the boundary condition Equation 3.4.3, and noting that $v^+ = -v^-$ for anti-plane displacement (Equation 3.1.9). As $\varepsilon \to 0$:

$$\begin{aligned}
\lim_{\varepsilon\to 0} I_1 &= \lim_{\varepsilon\to 0} \int_{-a}^{a} v_\varepsilon^+ \frac{\partial v_\varepsilon}{\partial x_2}^+ dx_1 = \int_{-a}^{a} v^+ \frac{\partial v}{\partial x_2}^+ dx_1 = -\frac{\beta}{\mu} \int_{-a}^{a} v^+ \frac{\partial^2 v}{\partial x_1^2}^+ dx_1 \\
\lim_{\varepsilon\to 0} I_2 &= \lim_{\varepsilon\to 0} \int_{-a}^{a} v_\varepsilon^- \frac{\partial v_\varepsilon}{\partial x_2}^- dx_1 = \int_{-a}^{a} v^- \frac{\partial v}{\partial x_2}^- dx_1 = \frac{\beta}{\mu} \int_{-a}^{a} v^- \frac{\partial^2 v}{\partial x_1^2}^- dx_1 \\
&= \frac{\beta}{\mu} \int_{-a}^{a} v^+ \frac{\partial^2 v}{\partial x_1^2}^+ dx_1 = -\lim_{\varepsilon\to 0} I_1
\end{aligned}$$

Given that the function w (and therefore v) is piecewise continuous (the crack tips are joined), it follows from the Hölder Condition [19, 18] that the product of v and it's derivatives ($\frac{\partial v}{\partial \boldsymbol{n}}$) are finite [25, 27, 19] such that:

$$\lim_{\varepsilon\to 0}|I_3| = \lim_{\varepsilon\to 0}\left|\int_{-\frac{\pi}{2}}^{\frac{\pi}{2}} v_r\frac{\partial v_r}{\partial r}d\theta\right| = \left|\int_{-\frac{\pi}{2}}^{\frac{\pi}{2}} v(\pm a,0)\frac{\partial v}{\partial \boldsymbol{n}}(\pm a,0)d\theta\right|$$
$$\leq \int_{-\frac{\pi}{2}}^{\frac{\pi}{2}} |v(\pm a,0)\nabla v(\pm a,0)|\, d\theta = \int_{-\frac{\pi}{2}}^{\frac{\pi}{2}} V_o^2 d\theta = \pi V_o^2$$

Where V_o^2 is some positive and finite value. Taking the limit as $\varepsilon \to 0$ on the right hand side of Equation 3.4.7 then yields:

$$\lim_{\varepsilon\to 0}(I_1 - I_2 - 2\varepsilon I_3) = \cancel{\lim_{\varepsilon\to 0}(I_1)} - \cancel{\lim_{\varepsilon\to 0}(I_1)} + \cancel{\lim_{\varepsilon\to 0}(2\varepsilon I_3)}^{0} = 0$$

Which gives the following result:

$$\int_\Omega |\nabla v|^2\, dA = 0 \tag{3.4.8}$$

Hence, by localization $|\nabla v| \equiv 0$ in Ω and $v = const$ in Ω $(= \mathbb{R}^2\backslash L)$. This means that any two solutions differ by only a constant (rigid body displacement), however given that $v^+ = -v^-$ for anti-plane displacement the values at the crack tips yield the condition that $v(-a,0) = v(a,0) = 0$. It is then concluded that $v \equiv 0$ (or, $w_2 = w_1$) and any solution for the problem in Equations 3.3.7 through 3.3.9 is unique.

It should also be noted that by using the same method for the classical case (when $\beta \to 0$) given by Equations 3.2.7 through 3.2.9 yields the same result.

3.5 Normalized Problem

The number of constants in the boundary value problem given by Equations 3.3.7 through 3.3.9 can be reduced from three (a, μ and β) to one by normalizing the variables. Begin by applying the spacial transformation of the independent coordinates so that $x_1, x_2 \to x, y$, where:

$$x \equiv \frac{x_1}{a} \quad \text{and} \quad y \equiv \frac{x_2}{a} \tag{3.5.1}$$

This yields a dimensionless set of spacial coordinates in the plane. Applying this transformation to the derivatives of $w(x_1, x_2)$ gives the following relations ($n > 1$):

$$\frac{\partial^n w}{\partial x_1^n} = \left(\frac{1}{a}\right)^n \frac{\partial^n w}{\partial x^n} \quad \text{and} \quad \frac{\partial^n w}{\partial x_2^n} = \left(\frac{1}{a}\right)^n \frac{\partial^n w}{\partial y^n} \tag{3.5.2}$$

The dimensionless input function $\tilde{P}$ shall be defined such that:

$$\tilde{P}(x) \equiv \frac{P(x_1)}{P_o} = \frac{P(ax)}{P_o} \tag{3.5.3}$$

Where P_o is defined as the root mean squared value of the input stress along the crack face:

$$P_o \equiv \sqrt{\frac{1}{2a}\int_{-a}^{a} (P(t))^2 \, dt} \tag{3.5.4}$$

The dimensionless, unit anti-plane displacement ($u(x, y)$) can then be defined as:

$$u(x, y) \equiv \frac{w(x_1, x_2)}{\vartheta} \tag{3.5.5}$$

Where the stress parameter (ϑ) is:

$$\vartheta \equiv a\left(\frac{P_o}{\mu}\right) \tag{3.5.6}$$

Putting this all together yields the following normalized equivalent to the boundary value problem in Equations 3.3.7 through 3.3.9:

$$\frac{\partial^2 u}{\partial x^2} + \frac{\partial^2 u}{\partial y^2} = 0, \qquad \text{in } \mathbb{R}^2 \backslash L \tag{3.5.7}$$

$$\frac{\partial u^{\pm}}{\partial y} = \tilde{P} \mp \gamma \frac{\partial^2 u^{\pm}}{\partial x^2} \qquad \text{on } L \tag{3.5.8}$$

$$\left|\frac{\partial u}{\partial \boldsymbol{n}}\right| \to 0 \qquad \text{as } |\boldsymbol{x}| \to \infty \tag{3.5.9}$$

Where the dimensionless surface parameter (γ) is defined as:

$$\gamma \equiv \frac{\beta}{a\mu} = \frac{\mu^s - \sigma_o}{a\mu} \tag{3.5.10}$$

These transformations are all invertible except for the cases when the constants a (half the crack length), P_o (input stress magnitude) or μ (modulus of rigidity) are zero, which are not points of interest for the boundary value problem.

4 - Complex Variables Analysis

4.1 The Complex Plane

Using complex variables analysis, any planar coordinate (x, y) can be transformed into a function of one variable by defining the complex coordinate (z) in the plane and it's complex conjugate $(\overline{z})$ as [20]:

$$z \equiv x + iy \qquad \text{and} \qquad \overline{z} \equiv x - iy \tag{4.1.1}$$

Where the complex number $i \equiv \sqrt{-1}$. Define $\phi(z)$ as the Complex Anti-Plane Displacement Function, such that:

$$\phi(z) \equiv u(x, y) + iv(x, y) \tag{4.1.2}$$

Where: $u(x, y)$ is the unit displacement defined in Section 3.5 and $v(x, y)$ is the complex conjugate to $u(x, y)$. Since $u(x, y)$ follows Laplace's Equation (Equation 3.5.7) in the body, then $\phi(z)$ is an analytic (or holomorphic) function in the body (not including the crack) and the functions $u(x, y)$ and $v(x, y)$ follow the Cauchy-Riemann Conditions [20] in $\mathbb{R}^2 \backslash L$:

$$\frac{\partial u}{\partial x} = \frac{\partial v}{\partial y} \qquad \text{and} \qquad \frac{\partial u}{\partial y} = -\frac{\partial v}{\partial x} \tag{4.1.3}$$

The complex conjugate [20, 21] of the function $\phi(z)$ is defined as:

$$\overline{\phi(z)} = \overline{\phi}(\overline{z}) \equiv u(x,y) - iv(x,y) \tag{4.1.4}$$

Since $\phi(z)$ is analytic in the body, it follows the reflection principal [21, 19, 20]:

$$\overline{\phi}(z) = \overline{\phi(\overline{z})} = u(x,-y) - iv(x,-y) \tag{4.1.5}$$

Define the positive $(+)$ and negative $(-)$ regions of the function $\phi(z)$ to be:

$$\phi^{\pm}(z) \equiv u(x,\pm y) + iv(x,\pm y) \tag{4.1.6}$$

This reveals an important conclusion to be used later:

$$\overline{\phi^{\pm}(z)} = \overline{\phi^{\mp}}(z) \tag{4.1.7}$$

Given that the function $\phi(z)$ is analytic in the body, the first derivative of $\phi(z)$ is given by [20]:

$$\phi'(z) = \frac{\partial u}{\partial x} + i\frac{\partial v}{\partial x} \tag{4.1.8}$$

Using 4.1.3, the derivative of $\phi(z)$ in terms of the function $u(x,y)$ is:

$$\phi'(z) = \frac{\partial u}{\partial x} - i\frac{\partial u}{\partial y} \tag{4.1.9}$$

Finally, utilizing Equation 4.1.8 once more, the second derivative of $\phi(z)$ is:

$$\phi''(z) = \frac{\partial^2 u}{\partial x^2} - i\frac{\partial^2 u}{\partial x \partial y} \tag{4.1.10}$$

The above framework satisfies the body Equation 3.5.7 (the harmonic condition). Application of this framework to the boundary condition Equations 3.5.8 and 3.5.9 is given in the following sections.

4.2 Boundary Conditions

The boundary condition from Equation 3.5.8 can be transformed into functions of $\phi(z)$ and it's derivatives by noting:

$$\frac{\partial u}{\partial x} = \frac{1}{2}\left(\phi'(z) + \overline{\phi'(z)}\right) = \mathfrak{Re}\left\{\phi'(z)\right\} \tag{4.2.1}$$
$$\frac{\partial u}{\partial y} = \frac{i}{2}\left(\phi'(z) - \overline{\phi'(z)}\right) = -\mathfrak{Im}\left\{\phi'(z)\right\} \tag{4.2.2}$$
$$\frac{\partial^2 u}{\partial x^2} = \frac{1}{2}\left(\phi''(z) + \overline{\phi''(z)}\right) = \mathfrak{Re}\left\{\phi''(z)\right\} \tag{4.2.3}$$

Since the normal vector is arbitrary at the plane extents, the boundary condition in Equation 3.5.9 is equivalent to:

$$\lim_{|z|\to\infty} \phi'(z) = 0 \tag{4.2.4}$$

Using Equations 4.2.1 through 4.2.3, Equation 3.5.8 can be re-written as:

$$\frac{i}{2}\left[\phi'(t) - \overline{\phi'(t)}\right]^{\pm} = \tilde{P}(t) \mp \frac{\gamma}{2}\left[\phi''(t) + \overline{\phi''(t)}\right]^{\pm} \tag{4.2.5}$$

Where t is defined as a real coordinate anywhere on the crack face such that $t \in x = [-1, 1]$. Proceeding further, Equations 3.1.11 and 4.2.2 gives the result:

$$\left[\phi'(z) - \overline{\phi'(z)}\right]^{+} = \left[\phi'(z) - \overline{\phi'(z)}\right]^{-} \tag{4.2.6}$$

Applying Equation 4.1.7 (reflection principal) to 4.2.6 gives:

$$
\begin{aligned}
& [\phi'(z)]^+ - \left[\overline{\phi'}(z)\right]^- = [\phi'(z)]^- - \left[\overline{\phi'}(z)\right]^+ \\
\therefore \qquad & [\phi'(z)]^+ + \left[\overline{\phi'}(z)\right]^+ = [\phi'(z)]^- + \left[\overline{\phi'}(z)\right]^- \equiv \Phi(z)
\end{aligned}
$$

This means that $\Phi(z)$ is invariant across the crack (L) and is analytic everywhere in the complex plane. Using Louivilles Theorem [20], then $\Phi(z)$ must be a constant ($\equiv \Phi_o$).

$$\Phi(z) = \phi'(z) + \overline{\phi'}(z) \equiv \Phi_o$$

However, given the boundary condition Equation 4.2.4, it is clear that $\Phi_o \equiv 0$. Hence:

$$\overline{\phi'}(z) = -\phi'(z) \tag{4.2.7}$$

Similarly, the general case (n^{th} derivative) leads to the following conclusion:

$$\left[\overline{\phi^{(n)}(z)}\right]^{\pm} = \left[\overline{\phi^{(n)}}(z)\right]^{\mp} = -\left[\phi^{(n)}(z)\right]^{\mp} \tag{4.2.8}$$

Adding both boundary conditions in Equation 4.2.5 (the $(+)$ and $(-)$ cases) yields:

$$
\begin{aligned}
\frac{i}{2}\left(\left[\phi'(t) - \overline{\phi'(t)}\right]^+ + \left[\phi'(t) - \overline{\phi'(t)}\right]^-\right) &= 2\tilde{P}(t) \\
&- \frac{\gamma}{2}\left(\left[\phi''(t) + \overline{\phi''(t)}\right]^+ - \left[\phi''(t) + \overline{\phi''(t)}\right]^-\right) \\
\therefore \frac{i}{2}\left([\phi'(t)]^+ + [\phi'(t)]^- + [\phi'(t)]^+ + [\phi'(t)]^-\right) &= 2\tilde{P}(t) \\
&- \frac{\gamma}{2}\left([\phi''(t)]^+ - [\phi''(t)]^- - [\phi''(t)]^- + [\phi''(t)]^+\right)
\end{aligned}
$$

Adding like terms provides a final equation encompassing all the boundary conditions (Equations 3.5.8 and 3.5.9) as a function of $\phi(t)$:

$$i\left([\phi'(t)]^{+}+[\phi'(t)]^{-}\right)+\gamma\left([\phi''(t)]^{+}-[\phi''(t)]^{-}\right)=2\tilde{P}(t) \tag{4.2.9}$$

4.3 The Hilbert Problem

The boundary condition in Equation 4.2.9 is not useful in it's current form. However, the Hilbert Problem [21] and it's known solution can be utilized. If there is a multi-valued function in the complex plane, such that the "jump" in value across a line (or crack, L) is given by:

$$F^{+}(t)-F^{-}(t)=h(t) \tag{4.3.1}$$

Then the solution of the problem in Equation 4.3.1 is given by [21]:

$$F(z)=\frac{1}{2\pi i}\int_{L}\frac{h(t)}{t-z}dt+F_{\infty} \tag{4.3.2}$$

Where F_{∞} is a constant and L denotes the crack extents ($L\in t=[-1,1]$). This result can be applied to Equation 4.2.9 such that:

$$\phi'(z)=\frac{1}{2\pi i}\int_{L}\frac{f(t)}{t-z}dt \tag{4.3.3}$$

Is the solution to the problem:

$$f(t)\equiv[\phi'(t)]^{+}-[\phi'(t)]^{-} \tag{4.3.4}$$

Here: $f(t)$ is an unknown function, where if provided would lead directly to analytical solution to $\phi'(z)$ using Equation 4.3.3. Also, if the function $g(t)$ is defined such that:

$$g(t) \equiv [\phi(t)]^+ - [\phi(t)]^- \tag{4.3.5}$$

Then $\phi(z)$ has the following solution:

$$\phi(z) = \frac{1}{2\pi i} \int_L \frac{g(t)}{t-z} dt + \phi_o \tag{4.3.6}$$

Where ϕ_o is a complex constant which can be interpreted as some form of a rigid body displacement. A more direct comparison of Equations 4.3.4 and 4.3.5 is found by considering:

$$g'(t) = \frac{d}{dt} \left([\phi(t)]^+ - [\phi(t)]^- \right) = [\phi'(t)]^+ - [\phi'(t)]^-$$

Then the function $f(t)$ is defined as the derivative of the function $g(t)$:

$$f(t) \equiv g'(t) \tag{4.3.7}$$

Also, taking the derivative of Equation 4.3.5 directly provides another relation between $f(t)$ and $g(t)$:

$$\begin{aligned}
\phi'(z) &= \frac{1}{2\pi i} \frac{d}{dz} \left[\int_L \frac{g(t)}{t-z} dt \right] + \cancelto{0}{\frac{d\phi_o}{dz}} = \frac{1}{2\pi i} \int_L \frac{g(t)}{(t-z)^2} \\
&= \frac{1}{2\pi i} \left[- \left. \frac{g(t)}{t-z} \right|_{t=-1}^{t=1} + \int_L \frac{g'(t)}{t-z} dt \right]
\end{aligned}$$

Therefore:

$$\int_L \frac{f(t)}{t-z} dt = - \left. \frac{g(t)}{t-z} \right|_{t=-1}^{t=1} + \int_L \frac{g'(t)}{t-z} dt \tag{4.3.8}$$

Hence, using the relation in Equation 4.3.7 it must hold true that:

$$\frac{g(1)}{1-z} + \frac{g(-1)}{1+z} = 0 \tag{4.3.9}$$

Using Equations 4.3.4 and 3.1.11, then:

$$\begin{aligned} f(t) = [\phi'(t)]^+ - [\phi'(t)]^- &= \lim_{x,y \to t, 0+} \left(\frac{\partial u}{\partial x} - i \frac{\partial u}{\partial y} \right) - \lim_{x,y \to t, 0-} \left(\frac{\partial u}{\partial x} - i \frac{\partial u}{\partial y} \right) \\ &= \left(\frac{\partial u^+}{\partial t} - \frac{\partial u^-}{\partial t} \right) - i \left(\cancel{\frac{\partial u^+}{\partial y}} - \cancel{\frac{\partial u^-}{\partial y}} \right) \end{aligned}$$

Finally, applying Equations 3.1.6 and 3.5.5, a physical interpretation of the function $f(t)$ emerges:

$$f(t) = g'(t) = \frac{\partial u^+}{\partial t} - \frac{\partial u^-}{\partial t} = \frac{1}{P_o} \left(\sigma_{13}^+ - \sigma_{13}^- \right) \tag{4.3.10}$$

Equation 4.3.10 demonstrates that the function $f(t)$ (or $g'(t)$) is defined as the jump in the gradient component of anti-plane displacement in the x direction across the crack face. Furthermore, $f(t)$ is linearly proportional to the jump in shear stress σ_{13} across the crack face. Using the Fundamental Theorem of Calculus [28]:

$$g(1) - g(-1) = \int_{-1}^{1} g'(t) dt \tag{4.3.11}$$

Then:

$$\begin{aligned} g(1) - g(-1) = \int_{-1}^{1} f(t) dt &= \int_{-1}^{1} \left(\frac{\partial u^+}{\partial t} - \frac{\partial u^-}{\partial t} \right) dt \\ &= \big(u(1, 0^+) - u(-1, 0^+) \big) - \big(u(1, 0^-) - u(-1, 0^-) \big) \\ &= \big(u(1, 0^+) - u(1, 0^-) \big) - \big(u(-1, 0^+) - u(-1, 0^-) \big) \end{aligned}$$

Note that $t = \pm 1$ is actually the point where the $(+)$ and $(-)$ regions of the crack join. Given this, it must hold that $u(1,0^+) = u(1,0^-)$ and $u(-1,0^+) = u(-1,0^-)$. Hence:

$$g(-1) - g(1) = 0$$

Or, alternatively:

$$g(-1) = g(1) \equiv g_o \tag{4.3.12}$$

Where g_o is a real valued constant. Also, the function $f(t)$ must be anti-symmetric and follows the relation:

$$\int_{-1}^{1} f(t)dt = 0 \tag{4.3.13}$$

Using Equation 4.3.9 with 4.3.12 gives:

$$g_o\left(\frac{1}{1-z} + \frac{1}{1+z}\right) = 0$$

Hence, the constant $g_o \equiv 0$. So:

$$g(1) = g(-1) = 0 \tag{4.3.14}$$

Furthermore, taking any arbitrary point s, where $-1 < s < 1$, then:

$$g(1) - g(s) = \big(u(1,0^+) - u(s,0^+)\big) - \big(u(1,0^-) - u(s,0^-)\big)$$
$$g(s) - g(-1) = \big(u(s,0^+) - u(-1,0^+)\big) - \big(u(s,0^-) - u(-1,0^-)\big)$$

Subtract these two equations to get:

$$g(s) = u(s,0^+) - u(s,0^-) \tag{4.3.15}$$

It is then concluded that the function $g(t)$ is defined as the jump in unit displacement (u) across the crack face.

4.4 Integral Equation Formulation

Given Equations 4.3.3 and 4.3.6, utilize the Plemelj Formula [21]:

$$[\phi(t)-\phi_o]^{\pm} = \pm\frac{1}{2}g(t) + \frac{1}{2\pi i}\int_L \frac{g(s)}{s-t}ds \tag{4.4.1}$$

Since ϕ_o is a constant, an alternate form Equation 4.4.1 is:

$$[\phi(t)]^{\pm} = \pm\frac{1}{2}g(t) + \phi_o + \frac{1}{2\pi i}\int_L \frac{g(s)}{s-t}ds \tag{4.4.2}$$

Taking the n^{th} derivative of 4.4.1 directly yields:

$$\left[\phi^{(n)}(t)\right]^{\pm} = \pm\frac{1}{2}g^{(n)}(t) + \frac{1}{2\pi i}\frac{d^n}{dt^n}\left[\int_L \frac{g(s)}{s-t}ds\right], \qquad n \geq 1 \tag{4.4.3}$$

Using Equation 4.4.3 with Equation 4.2.9, the following integro-differential equation emerges:

$$\frac{1}{\pi}\frac{d}{dt}\left[\int_L \frac{g(s)}{s-t}ds\right] + \gamma g''(t) = 2\tilde{P}(t) \tag{4.4.4}$$

Note that the variables t and s are along the crack and lie on the real axis between $-1 \leq t, s \leq 1$. So Equation 4.4.4 is a real (not complex) integro-differential equation and satisfies all boundary conditions on the crack.

Using Equation 4.3.14, an alternate form of 4.4.4 in terms of $f(t)$ can be found by noting:

$$\frac{d}{dt}\left[\int_L \frac{g(s)}{s-t}ds\right] = \int_L \frac{g(s)}{(s-t)^2}ds = \int_L \frac{g'(s)}{s-t}ds - \cancelto{0}{\left[\frac{g(s)}{s-t}\right]_{s=-1}^{s=1}}$$

Since $f(t) = g'(t)$, then:

$$\frac{1}{\pi}\left[\int_L \frac{f(s)}{s-t}ds\right] + \gamma f'(t) = 2\tilde{P}(t) \qquad (4.4.5)$$

Integrating Equations 4.4.4 and 4.4.5 with respect to t yields:

$$\gamma g'(t) + \frac{1}{\pi}\int_L \frac{g(s)}{s-t}ds = 2\zeta_1(t) - C_1 \qquad (4.4.6)$$

$$\gamma f(t) - \frac{1}{\pi}\int_L f(s)\ln|s-t|ds = 2\zeta_1(t) - C_1' \qquad (4.4.7)$$

Where C_1 and C_1' are real constants of integration and the function $\zeta_1(x)$ is defined as:

$$\zeta_1(x) \equiv \int_0^x \tilde{P}(t)dt \qquad (4.4.8)$$

Integrating Equation 4.4.4 a second time with respect to t yields:

$$\gamma g(t) - \frac{1}{\pi}\int_L g(s)\ln|s-t|dt = 2\zeta_2(t) - C_1 t - C_2 \qquad (4.4.9)$$

Where C_2 is a second constant of integration and $\zeta_2(x)$ is defined as:

$$\zeta_2(x) \equiv \int_0^x \int_0^t \tilde{P}(s)dsdt \qquad (4.4.10)$$

Note that Equations 4.4.7 and 4.4.9 are identical with exception of the integration order of the input function and the number of constants. Depending on whether the displacement or stress (which are linearly proportional to the gradient elements) magnitudes are desired, they are both solutions of the same integral equation. If function $\theta(x)$ is defined as:

$$\theta(x) \equiv \lim_{y \to 0^+} u(x,y) \tag{4.4.11}$$

Then θ is a direct, unit anti-plane displacement on the crack face where:

$$u(x,0^{\pm}) = \pm\theta(x) \tag{4.4.12}$$

Also noting that $u^+ = -u^-$ (Equation 3.1.9), then:

$$g(x) = u(x,0^+) - u(x,0^-) = \theta(x) - (-\theta(x))$$

Hence:

$$g(x) = 2\theta(x) \tag{4.4.13}$$

$$f(x) = 2\theta'(x) \tag{4.4.14}$$

Using Equations 4.4.9, 4.4.7, 4.4.13, and 4.4.14, then re-arranging the variables the integral equations for $\theta'(x)$ and $\theta(x)$ are:

$$\gamma\theta'(x) - \frac{1}{\pi}\int_L \theta'(t)\ln|t-x|dt = \zeta_1(x) - C_1' \tag{4.4.15}$$

$$\gamma\theta(x) - \frac{1}{\pi}\int_L \theta(t)\ln|t-x|dt = \zeta_2(x) - C_1x - C_2 \tag{4.4.16}$$

Where: $-1 \leq x, t \leq 1$. Equations 4.4.15 and 4.4.16 are Fredholm Equations of the second kind [17, 18]. Given Equation 4.3.14, the required boundary conditions on the crack tips are:

$$\theta(-1) = \theta(1) = 0 \tag{4.4.17}$$

Using Equation 4.3.13 and 4.4.14, the required slope condition (anti-symmetry requirement) is:

$$\int_{-1}^{1} \theta'(x)dx = 0 \tag{4.4.18}$$

The constants C_1, C_1' and C_2 from the Fredholm Equations 4.4.15 and 4.4.16 are determined by the boundary conditions at the crack tips from Equation 4.4.17 and the anti-symmetry requirement in Equation 4.4.18. From the solutions of Equations 4.4.15 and 4.4.16, the anti-plane displacement (w) and corresponding stress (σ_{13}) on the crack face are retrievable using the inverse transformations from Section 3.5.

Taking these formulations further, it is possible to calculate the adjusted input stress (σ_{23}) due to the surface effect directly by interpreting Equation 3.3.8 in a different way. Note that:

$$\frac{\partial u}{\partial y} = \frac{\sigma_{23}}{P_o} \tag{4.4.19}$$

Using this result along with Equation 3.3.8, the adjusted unit input stress along the (+) crack face (define as $\theta_y(x)$) has the form:

$$\theta_y(x) \equiv \frac{\partial u}{\partial y}(x, 0^+) = \tilde{P}(x) - \gamma\theta''(x) \tag{4.4.20}$$

Also, taking the derivative of Equation 4.4.15 gives:

$$\gamma\theta''(x) - \frac{1}{\pi}\int_L \frac{\theta'(t)}{t-x}dt = \tilde{P}(x)$$

However:

$$\frac{d}{dt}\left[\theta'(t)\ln|t-x|\right] = \theta''(t)\ln|t-x| + \frac{\theta'(t)}{t-x}$$

Hence, the integral equation for $\theta''(x)$ is:

$$\gamma\theta''(x) - \frac{1}{\pi}\int_L \theta''(t)\ln|t-x|dt = \tilde{P}(x) - \left[\frac{1}{\pi}\theta'(t)\ln|t-x|\right]_{t=-1}^{t=1} \qquad (4.4.21)$$

Again, note the similarities between the left hand side of Equation 4.4.21 compared to Equations 4.4.15 and 4.4.16. If the magnitude of corresponding stresses at the crack tips ($\sigma_{13} \propto \theta'(\pm 1)$) are finite and non zero, then the right hand side of Equation 4.4.21 can not be. Given this, the adjusted input stresses at the crack tips ($\sigma_{23} \propto \theta_y(\pm 1)$) are not finite with this model, even if the externally applied stress function ($\tilde{P}$) is.

4.5 Body Displacements and Gradients

Assuming a solution can be found for $\theta(x)$ from Equation 4.4.16, the unit displacement anywhere in the bulk material is the real part of Equation 4.3.6:

$$u(x,y) = \mathfrak{Re}\left\{\frac{1}{\pi i}\int_L \frac{\theta(t)}{t-z}dt\right\} + u_o \qquad (4.5.1)$$

Where u_o is a real constant and is defined as the real part of ϕ_o such that:

$$\phi_o \equiv u_o + iv_o \qquad (4.5.2)$$

To further investigate the value of u_o, note that using 4.4.2 gives:

$$[\phi(t)]^+ + [\phi(t)]^- = 2\phi_o + \frac{1}{\pi i}\int_L \frac{g(s)}{s-t}ds \qquad (4.5.3)$$

Using $t = 0$ in Equation 4.5.3, and again noting that $u^+ = -u^-$:

$$[\phi(0)]^+ + [\phi(0)]^- = [\cancel{u(0,0)} + iv(0,0)]^+ + [\cancel{u(0,0)} + iv(0,0)]^-$$
$$\therefore i\left(v(0,0^+) + v(0,0^-)\right) = 2u_o + i\left(2v_o - \frac{1}{\pi}\int_L \frac{g(s)}{s}ds\right)$$

Hence, the constant $u_o = 0$. The value of $u(x, y)$ anywhere in the body is then:

$$u(x,y) = \mathfrak{Re}\left\{\phi(z)\right\} = \mathfrak{Im}\left\{\frac{1}{\pi}\int_L \frac{\theta(t)}{t-z}dt\right\} \tag{4.5.4}$$

Similarly, Equations 4.3.3 and 4.1.9 provide the gradient elements anywhere in the body:

$$\frac{\partial u}{\partial x} = \mathfrak{Re}\left\{\phi'(z)\right\} = \mathfrak{Im}\left\{\frac{1}{\pi}\int_L \frac{\theta'(t)}{t-z}dt\right\} \tag{4.5.5}$$
$$\frac{\partial u}{\partial y} = -\mathfrak{Im}\left\{\phi'(z)\right\} = \mathfrak{Re}\left\{\frac{1}{\pi}\int_L \frac{\theta'(t)}{t-z}dt\right\} \tag{4.5.6}$$

Where $\theta'(x)$ is the solution of Equation 4.4.15.

Part III

Solution and Results

5 - Numerical Model

5.1 Numerical Integral Equation Formulation

The displacement and slope on the crack face can be found by solving the Fredholm Equations 4.4.15 and 4.4.16, which both have the general form:

$$\gamma\theta(x) - \frac{1}{\pi}\int_{-1}^{1}\theta(t)\ln|t-x|dt = \zeta(x), \quad -1 \leq x \leq 1 \tag{5.1.1}$$

Various methods (such as Collocation and Neumann Series Expansions [22]) were successfully implemented to solve Equation 5.1.1. However, using some creative analytical tricks before computation a discretized residual model can be used for approximation. This method (similar to finite element method) is proven stable and convergent. Examples of such numerical procedures for various singular integral equations are laid out in the works of Atkinson [23] and Delves & Mohamed [22]. Discretization and meshing used is from standard Finite Element Analysis [29, 30] theory. The full procedure used to approximate the solution for Equation 5.1.1 is as follows.

Start by discretizing x $(-1 < x < 1)$ into N elements with p points per element, and define the spacial length of each element as:

$$h_e \equiv x_p^e - x_1^e \tag{5.1.2}$$

This gives a subspace of solutions for $\theta(x)$, such that:

$$\theta(x) \equiv \begin{cases} \theta^1(x) & , x_1^1 \leq x \leq x_p^1 \\ \theta^2(x) & , x_1^2 \leq x \leq x_p^2 \\ \quad\vdots & \\ \theta^e(x) & , x_1^e \leq x \leq x_p^e \\ \quad\vdots & \\ \theta^N(x) & , x_1^N \leq x \leq x_p^N \end{cases} \tag{5.1.3}$$

In this case, $x_1^1 = -1$ and $x_p^N = 1$ (the endpoints). To enforce continuity of the solution between elements, it is required that $x_p^e = x_1^{e+1}$ and $\theta(x_p^e) = \theta(x_1^{e+1})$. Each element solution shall be approximated as a Lagrange Polynomial [29, 30]:

$$\theta^e(x) \simeq \sum_{n=1}^{p} \theta_n^e M_n^e(x) \tag{5.1.4}$$

Where: θ_n^e are the values of $\theta(x_n^e)$, and the interpolating functions $(M_n^e(x))$ are defined as polynomial shape functions:

$$M_n^e(x) \equiv \prod_{\substack{a=1 \\ a\neq n}}^{p} \left[\frac{x - x_a^e}{x_n^e - x_a^e}\right] \tag{5.1.5}$$

Define the kernel integral function from Equation 5.1.1 as:

$$k(x) \equiv \int_{-1}^{1} \theta(t) \ln|t - x| dt = \sum_{e=1}^{N} k^e(x) \tag{5.1.6}$$

Let the kernel integral for each element $(k^e(x))$ be defined as:

$$k^e(x) \equiv \int_{x_1^e}^{x_p^e} \theta^e(t) \ln|t - x| dt \tag{5.1.7}$$

Using Equations 5.1.3, 5.1.4 and 5.1.7, the kernel integral function for each element has the approximation:

$$
\begin{aligned}
k^e(x) &= \int_{x_1^e}^{x_p^e} \theta^e(t) \ln|t-x| dt \simeq \int_{x_1^e}^{x_p^e} \left(\sum_{n=1}^{p} \theta_n^e M_n^e(t) \right) \ln|t-x| dt \\
&= \sum_{n=1}^{p} \theta_n^e \int_{x_1^e}^{x_p^e} M_n^e(t) \ln|t-x| dt = \sum_{n=1}^{p} \theta_n^e \psi_n^e(x)
\end{aligned}
$$

Where $\psi_n^e(x)$ is defined as the element logarithmic interpolation integral:

$$
\psi_n^e(x) \equiv \int_{x_1^e}^{x_p^e} M_n^e(t) \ln|t-x| dt \tag{5.1.8}
$$

Solving $\psi_n^e(x)$ numerically is problematic due to the singular nature of the natural log term. However, since the Lagrange interpolation functions are polynomials it is convenient to define the element logarithmic interpolation function as:

$$
H_k^e(x) \equiv \int_{x_1^e - x}^{x_p^e - x} s^{k-1} \ln|s| ds = \left[\frac{s^k}{k} \left(\ln|s| - \frac{1}{k} \right) \right]_{x_1^e - x}^{x_p^e - x}, \qquad k \geq 1 \tag{5.1.9}
$$

Before proceeding, the following must be considered:

1. When $s \to 0$ in Equation 5.1.9 (or alternatively when $x \to x_p^e, x_1^e$), there is a computational issue of $\ln|s| \to \pm\infty$. This can be mitigated numerically by noting that:

$$
\lim_{s \to 0} \frac{s^k}{k} \left(\ln|s| - \frac{1}{k} \right) = 0, \qquad k \geq 1
$$

   Instead of attempting computation at the element endpoints, manually apply the relations:

$$H_k^e(x_1^e) = \frac{h_e^k}{k}\left(\ln(h_e) - \frac{1}{k}\right) \tag{5.1.10}$$

$$H_k^e(x_p^e) = (-1)^{k+1}\frac{h_e^k}{k}\left(\ln(h_e) - \frac{1}{k}\right) \tag{5.1.11}$$

2. Elements with more than 2 points ($p > 2$) can can produce significant computational errors when evaluating the value of H_k^e close to the element endpoints ($x \cong x_1^e, x_p^e$). If each element is kept "simple" by enforcing the constraint $p = 2$, then <u>only</u> the endpoints are used and using Equations 5.1.10 and 5.1.11 significantly reduces this error. Given this, each element will be approximated as a linear function ($p = 2$) and only h-refinement [29, 30] (increasing N) will be pursued.

With $p = 2$, the continuity conditions yield the global relations: $x_1^e \equiv \mathrm{x}_e$, $x_2^e \equiv \mathrm{x}_{e+1}$, $\theta_1^e \equiv \Theta_e$, and $\theta_2^e \equiv \Theta_{e+1}$. The approximated solution for $\theta(x)$ and discretized locations are then subspace vectors in the form:

$$\boldsymbol{\Theta} = \langle \Theta_1, \Theta_2, \ldots, \Theta_n, \ldots, \Theta_{N+1} \rangle \tag{5.1.12}$$

$$\mathbf{x} = \langle \mathrm{x}_1, \mathrm{x}_2, \ldots, \mathrm{x}_n, \ldots, \mathrm{x}_{N+1} \rangle \tag{5.1.13}$$

The interpolating functions for each element are:

$$M_1^e(x) = \frac{x - \mathrm{x}_{e+1}}{\mathrm{x}_e - \mathrm{x}_{e+1}} = -\frac{x - \mathrm{x}_{e+1}}{h_e} \tag{5.1.14}$$

$$M_2^e(x) = \frac{x - \mathrm{x}_e}{\mathrm{x}_{e+1} - \mathrm{x}_e} = \frac{x - \mathrm{x}_e}{h_e} \tag{5.1.15}$$

The function $\psi_1^e(x)$ can now be determined analytically:

$$\begin{aligned}\psi_1^e(x) &= \int_{\mathrm{x}_e}^{\mathrm{x}_{e+1}} M_1^e(t) \ln|t - x| dt = -\frac{1}{h_e}\int_{\mathrm{x}_e}^{\mathrm{x}_{e+1}} (t - \mathrm{x}_{e+1}) \ln|t - x| dt \\ &= -\frac{1}{h_e}\left[\int_{\mathrm{x}_e}^{\mathrm{x}_{e+1}} t \ln|t - x| dt - \mathrm{x}_{e+1}\int_{\mathrm{x}_e}^{\mathrm{x}_{e+1}} \ln|t - x| dt\right]\end{aligned}$$

$$= -\frac{1}{h_e}\left[\int_{\mathrm{x}_e - x}^{\mathrm{x}_{e+1}-x} (s+x)\ln|s|ds - \mathrm{x}_{e+1}\int_{\mathrm{x}_e - x}^{\mathrm{x}_{e+1}-x} \ln|s|ds\right]$$
$$= -\frac{1}{h_e}\left[\int_{\mathrm{x}_e - x}^{\mathrm{x}_{e+1}-x} s\ln|s|ds + (x - \mathrm{x}_{e+1})\int_{\mathrm{x}_e - x}^{\mathrm{x}_{e+1}-x} \ln|s|ds\right]$$

Finally, using Equation 5.1.9 yields:

$$\psi_1^e(x) = -\frac{1}{h_e}\left[H_2^e(x) + (x - \mathrm{x}_{e+1})\, H_1^e(x)\right] \tag{5.1.16}$$

Similarly, for $\psi_2^e(x)$:

$$\psi_2^e(x) = \frac{1}{h_e}\left[H_2^e(x) + (x - \mathrm{x}_{e})\, H_1^e(x)\right] \tag{5.1.17}$$

Using this discretization, Equation 5.1.1 has the approximation:

$$\gamma\left[\sum_{i=1}^{2} M_i^e(x)\Theta_e\right] - \frac{1}{\pi}\sum_{k=1}^{N}\left[\psi_1^k(x)\Theta_k + \psi_2^k(x)\Theta_{k+1}\right] = \zeta(x) \tag{5.1.18}$$

Also note that when $p = 2$, the interpolation functions at the node points have the following properties:

$$M_1^e(\mathrm{x}_e) = 1 \qquad M_1^e(\mathrm{x}_{e+1}) = 0$$
$$M_2^e(\mathrm{x}_e) = 0 \qquad M_2^e(\mathrm{x}_{e+1}) = 1$$

Using each location from the vector $\mathbf{x}$ provides $N+1$ linear equations for $N+1$ unknowns $(\Theta_1, \Theta_2, \ldots, \Theta_{N+1})$:

$$\gamma\Theta_e - \frac{1}{\pi}\sum_{k=1}^{N}\left[\psi_1^k(\mathrm{x}_e)\Theta_k + \psi_2^k(\mathrm{x}_e)\Theta_{k+1}\right] = \zeta(\mathrm{x}_e), \qquad e = 1, 2, \ldots, N+1$$

Or, alternatively:

$$\mathbf{K\Theta} = \mathbf{F} \tag{5.1.19}$$

Where **K** and **F** are defined as the stiffness matrix and forcing vector respectively. The solution of this set then has the relation:

$$\mathbf{\Theta} = \mathbf{K}^{-1}\mathbf{F} \tag{5.1.20}$$

Here, convergence is assumed (and discussed more in Section 6.4), meaning:

$$\lim_{N\to\infty} \mathbf{\Theta} = \theta(x)$$

5.2 Numerical Integration of Input Functions

Recall the integrated unit input stress functions (ζ_1 and ζ_2 from Equations 4.4.8 and 4.4.10 respectively):

$$\zeta_1(x) \equiv \int_0^x \tilde{P}(t)dt$$
$$\zeta_2(x) \equiv \int_0^x \int_0^t \tilde{P}(s)dsdt$$

These integrals can be computed numerically using the Gauss Quadrature Method [29, 30] assuming that the unit input stress function ($\tilde{P}(x)$) is not singular in the range of $-1 \leq x \leq 1$. First, transform s, t to ξ, η such that:

$$s \equiv \frac{t}{2}(\xi + 1) \qquad \text{and} \qquad t \equiv \frac{x}{2}(\eta + 1) \tag{5.2.1}$$

The integrals from 4.4.8 and 4.4.10 can then be transformed into the variable space ξ and η as follows:

$$ds = \frac{t}{2}d\xi \qquad \text{and} \qquad dt = \frac{x}{2}d\eta$$
$$\therefore \qquad s = \frac{1}{2}\left[\frac{x}{2}\eta + \frac{x}{2}\right]\zeta + \frac{1}{2}\left[\frac{x}{2}\eta + \frac{x}{2}\right] = \frac{x}{4}(\xi+1)(\eta+1)$$

$$ds = \frac{t}{2} d\xi = \frac{1}{2}\left[\frac{x}{2}\eta + \frac{x}{2}\right] d\xi = \frac{x}{4}\left(\eta + 1\right) d\xi$$

Plugging these back into Equations 4.4.8 and 4.4.10 yields:

$$\zeta_1(x) = \frac{x}{2}\int_{-1}^{1} \tilde{P}\left(\frac{x}{2}\left[\eta + 1\right]\right) d\eta \tag{5.2.2}$$

$$\zeta_2(x) = \frac{x^2}{8}\int_{-1}^{1}\int_{-1}^{1} \left(\eta + 1\right) \tilde{P}\left(\frac{x}{4}\left[\xi + 1\right]\left[\eta + 1\right]\right) d\xi d\eta \tag{5.2.3}$$

Define the number of Gauss Points [30] for each integral as G, such that the functions ζ_1 and ζ_2 have the numerical approximations at any point x:

$$\zeta_1(x) \simeq \frac{x}{2}\sum_{i=1}^{G} W_i \tilde{P}\left(\frac{x}{2}\left[\eta_i + 1\right]\right) \tag{5.2.4}$$

$$\zeta_2(x) \simeq \frac{x^2}{8}\sum_{j=1}^{G+1}\sum_{i=1}^{G} W_i W_j \left(\eta_i + 1\right) \tilde{P}\left(\frac{x}{4}\left[\xi_j + 1\right]\left[\eta_i + 1\right]\right) \tag{5.2.5}$$

Where W_i, W_j are the Gauss Weights and η_i, ξ_j are the Gauss Points. If $\tilde{P}(x)$ is a polynomial of order k, then the approximations in Equations 5.2.4 and 5.2.5 are exact (neglecting numerical error) if [29, 30]:

$$G \geq \frac{1}{2}\left(k + 1\right), \qquad\qquad GP \in \mathbb{I} \tag{5.2.6}$$

If the function $\tilde{P}(x)$ is not a polynomial, then increasing the number of Gauss Points increases accuracy.

5.3 Crack Face Displacement

Use Equation 5.1.20 as a base for an approximation to 4.4.16, where:

$$\gamma\theta(x) - \frac{1}{\pi}\int_{-1}^{1} \theta(t) \ln|t - x| dt + C_1 x + C_2 = \zeta_2(x)$$

The global system of equations is then given by:

$$\mathbf{K\Theta} + \mathbf{C}_1 + \mathbf{C}_2 = \mathbf{F}_2 \tag{5.3.1}$$

Where the stiffness matrix $\mathbf{K}$ is same as in Equation 5.1.20. The vectors $\mathbf{C}_1$, $\mathbf{C}_2$ and $\mathbf{F}_2$ are defined as:

$$\mathbf{C}_1 = C_1 \langle \mathrm{x}_1, \mathrm{x}_2, \ldots, \mathrm{x}_n, \ldots, \mathrm{x}_{N+1} \rangle \tag{5.3.2}$$

$$\mathbf{C}_2 = C_2 \langle 1, 1, \ldots, 1, \ldots, 1 \rangle \tag{5.3.3}$$

$$\mathbf{F}_2 = \langle \zeta_2(\mathrm{x}_1), \zeta_2(\mathrm{x}_2), \ldots, \zeta_2(\mathrm{x}_n), \ldots, \zeta_2(\mathrm{x}_{N+1}) \rangle \tag{5.3.4}$$

The function $\zeta_2(x)$ is computed through the approximation in Equation 5.2.5. The constants C_1 and C_2 require using Equation 4.4.17, which become:

$$\Theta_1 = 0 \qquad \text{and} \qquad \Theta_{N+1} = 0 \tag{5.3.5}$$

This gives a total of $N+3$ linear equations for $N+3$ unknowns (Θ_1, Θ_2, …, Θ_{N+1}, C_1 and C_2).

5.4 Crack Face Derivatives

It is useful to compute the crack face derivatives ($\theta'(x)$ and $\theta''(x)$) because they are linearly proportional to the stresses and strains on the crack face. Taking the same approach from Section 5.3, the solution to Equation 4.4.15 is formulated using the approximation from 5.1.20 as a base. Start with:

$$\gamma\theta'(x) - \frac{1}{\pi}\int_{-1}^{1} \theta'(t) \ln|t - x| dt + C_1' = \zeta_1(x)$$

This yields the system of global equations:

$$\mathbf{K}\boldsymbol{\Theta}' + \mathbf{C}_1' = \mathbf{F}_1 \tag{5.4.1}$$

The stiffness matrix $\mathbf{K}$ is same as in Equation 5.1.20. Also, the vector subspace solution is defined as:

$$\boldsymbol{\Theta}' = \left\langle \Theta_1', \Theta_2', \ldots, \Theta_n', \ldots, \Theta_N', \Theta_{N+1}' \right\rangle \tag{5.4.2}$$

Using Equation 5.2.4, the vectors $\mathbf{C}_1'$ and $\mathbf{F}_1$ are defined as:

$$\mathbf{C}_1' = C_1' \langle 1, 1, \ldots, 1, \ldots, 1 \rangle \tag{5.4.3}$$

$$\mathbf{F}_1 = \langle \zeta_1(\mathrm{x}_1), \zeta_1(\mathrm{x}_2), \ldots, \zeta_1(\mathrm{x}_n), \ldots, \zeta_1(\mathrm{x}_{N+1}) \rangle \tag{5.4.4}$$

$\theta'(x)$ for each linear element ($p = 2$) is approximated by using Equations 5.1.4, 5.1.14, and 5.1.15 ($\mathrm{x}_e \leq x \leq \mathrm{x}_{e+1}$):

$$\frac{d\theta^e}{dx} \simeq \frac{1}{h_e} \left[\left(\Theta_{e+1}' - \Theta_e' \right) x - \left(\Theta_{e+1}' \mathrm{x}_e - \Theta_e' \mathrm{x}_{e+1} \right) \right]$$

Because of the constant C_1', Equation 4.3.13 is also required. Note that:

$$\begin{aligned}
\int_{\mathrm{x}_e}^{\mathrm{x}_{e+1}} \frac{d\theta^e}{dx} dx &\simeq \frac{1}{h_e} \int_{\mathrm{x}_e}^{\mathrm{x}_{e+1}} \left[\left(\Theta_{e+1}' - \Theta_e' \right) x - \left(\Theta_{e+1}' \mathrm{x}_e - \Theta_e' \mathrm{x}_{e+1} \right) \right] dx \\
&= \frac{1}{2} \left(\Theta_{e+1}' - \Theta_e' \right) \left(\mathrm{x}_{e+1} + \mathrm{x}_e \right) - \left(\Theta_{e+1}' \mathrm{x}_e - \Theta_e' \mathrm{x}_{e+1} \right) \\
&= \frac{h_e}{2} \left(\Theta_{e+1}' + \Theta_e' \right)
\end{aligned}$$

Which gives the final equation:

$$\sum_{e=1}^{N} h_e \left(\Theta_{e+1}' + \Theta_e' \right) = 0 \tag{5.4.5}$$

This yields a total of $N + 2$ linear equations for $N + 2$ unknowns (Θ_1', Θ_2',

$\ldots$, Θ'_{N+1} and C'_1).

Instead of directly attempting to solve Equation 4.4.21 (which is singular at the end points), $\theta''(x)$ can be approximated using the finite difference method [29]. For each element, assume the approximation:

$$\frac{d^2\theta^e}{dx^2} \simeq \frac{\Theta'_{e+1} - \Theta'_e}{\mathrm{x}_{e+1} - \mathrm{x}_e} \equiv \Theta''_e \tag{5.4.6}$$

Note that this approximation for $\theta''(x)$ is an average across the elements and does not give a continuous solution. Also, there is one less value in this subspace (N components). However, assuming a center finite difference (the discretization is the average point of each element) then:

$$\mathrm{x}'_e \equiv \tfrac{1}{2}\left(\mathrm{x}_{e+1} + \mathrm{x}_e\right) \tag{5.4.7}$$

This yields a vector subspace approximation defined as:

$$\mathbf{\Theta}'' = \langle \Theta''_1, \Theta''_2, \ldots, \Theta'_n, \ldots, \Theta''_N \rangle \tag{5.4.8}$$

$$\mathbf{x}' = \langle \mathrm{x}'_1, \mathrm{x}'_2, \ldots, \mathrm{x}'_n, \ldots, \mathrm{x}'_N \rangle \tag{5.4.9}$$

Using the boundary condition in Equation 3.5.8, the y-component of the gradient on the crack face is:

$$\frac{\partial u}{\partial y}(x, 0^+) \equiv \theta_y(x) = \tilde{P}(x) - \gamma\theta''(x)$$

Which provides an approximation for $\theta_y(x)$ in each element:

$$\theta^e_y(\mathrm{x}'_e) \simeq \tilde{P}(\mathrm{x}'_e) - \gamma\Theta''_e \tag{5.4.10}$$

Given that the approximation in Equation 5.4.6 and 5.4.7 are averages across the elements and that the values of $\theta_y(\pm 1)$ are not finite (see Section 4.4), then the values computed for the function $\theta_y(x)$ will not be convergent near these points.

5.5 Bulk Displacement

Using Equation 4.5.4, the unit displacement anywhere in the body was determined to be:

$$u(x, y) = \mathfrak{Re}\left\{\phi(z)\right\} = \mathfrak{Im}\left\{\frac{1}{\pi}\int_{-1}^{1}\frac{\theta(t)}{t-z}dt\right\}$$

Where:

$$\phi(z) = \frac{1}{\pi i}\int_{-1}^{1}\frac{\theta(t)}{t-z}dt$$

Using the same discretization for $\theta(x)$ as Equation 5.1.3, the function $\phi(z)$ has the approximation:

$$\phi(z) \simeq \frac{1}{\pi i}\sum_{e=1}^{N}\int_{\mathrm{x}_e}^{\mathrm{x}_{e+1}}\frac{\theta^e(t)}{t-z}dt = \frac{1}{\pi i}\sum_{e=1}^{N} I^e(z)$$

Where the function I^e is defined as:

$$I^e(z) \equiv \int_{x_e}^{x_{e+1}}\frac{\theta^e(t)}{t-z}dt \tag{5.5.1}$$

Utilizing the subspace approximation for $\theta(x)$ from Equation 5.1.12, note that each element approximation for $\theta^e(x)$ is a linear function of the form:

$$\theta^e(x) \simeq \frac{1}{h_e}\left[\left(\Theta_{e+1} - \Theta_e\right)x - \left(\Theta_{e+1}\mathrm{x}_e - \Theta_e\mathrm{x}_{e+1}\right)\right]$$

If the element constants are defined as:

$$m_e \equiv \frac{\Theta_{e+1} - \Theta_e}{\mathrm{x}_{e+1} - \mathrm{x}_e} \qquad \text{and} \qquad b_e \equiv \frac{\Theta_e \mathrm{x}_{e+1} - \Theta_{e+1} \mathrm{x}_e}{\mathrm{x}_{e+1} - \mathrm{x}_e}$$

Then, $I^e(z)$ from Equation 5.5.1 becomes:

$$I^e(z) = \int_{\mathrm{x}_e}^{\mathrm{x}_{e+1}} \frac{m_e t + b_e}{t - z} dt = \int_{\mathrm{x}_e - z}^{\mathrm{x}_{e+1} - z} \left(m_e + \frac{m_e z + b_e}{s} \right) ds$$

Therefore, after some simplification:

$$I^e(z) = m_e h_e + (m_e z + b_e) \log \left(\frac{\mathrm{x}_{e+1} - z}{\mathrm{x}_e - z} \right) \tag{5.5.2}$$

So, the function $\phi(z)$ has the approximation:

$$\phi(z) \simeq \frac{1}{\pi i} \sum_{e=1}^{N} \left[m_e h_e + (m_e z + b_e) \log \left(\frac{\mathrm{x}_{e+1} - z}{\mathrm{x}_e - z} \right) \right] \tag{5.5.3}$$

Finally, using Equation 4.5.4, the unit displacement ($u(x, y)$) anywhere in the body is approximated to be:

$$u(x, y) \simeq \sum_{e=1}^{N} \mathfrak{Im} \left\{ \left[\frac{\Theta_{e+1} z_e - \Theta_e z_{e+1}}{\pi h_e} \right] \log \left(\frac{z_{e+1}}{z_e} \right) \right\} \tag{5.5.4}$$

Where: $z_e \equiv z - \mathrm{x}_e$ and $z_{e+1} \equiv z - \mathrm{x}_{e+1}$. The relation in Equation 5.5.4 holds anywhere in the body except along the crack face ($x, y = [-1, 1], 0$). However, the values for displacement along the crack face ($\theta(x)$) is already formulated and re-computation is not required. It should be noted that the largest numerical error will occur when evaluating $\phi(z)$ near the crack. The required accuracy is achieved by using h-refinement (decrease h_e, or conversely increasing N). Discussion of accuracy and refinement is given in Section 6.4.

5.6 Gradient in Bulk Material

The logic in this section is identical to Section 5.5. Using Equations 4.5.5 and 4.5.6, the displacement gradients are:

$$\frac{\partial u}{\partial x} = \mathfrak{Re}\left\{\phi'(z)\right\} = \mathfrak{Im}\left\{\frac{1}{\pi}\int_L \frac{\theta'(t)}{t-z}dt\right\}$$
$$\frac{\partial u}{\partial y} = -\mathfrak{Im}\left\{\phi'(z)\right\} = \mathfrak{Re}\left\{\frac{1}{\pi}\int_L \frac{\theta'(t)}{t-z}dt\right\}$$

Where:

$$\phi'(z) = \frac{1}{\pi i}\int_{-1}^{1} \frac{\theta'(t)}{t-z}dt$$

Using the same technique as in the formulation for Equation 5.5.3 and the approximation for $\theta'(x)$ from Section 5.4, the function $\phi'(z)$ has the approximation:

$$\phi'(z) \simeq \sum_{e=1}^{N} \frac{1}{\pi i}\left[\left(\Theta'_{e+1} - \Theta'_e\right) + \left(\frac{\Theta'_{e+1}z_e - \Theta'_e z_{e+1}}{h_e}\right)\log\left(\frac{z_{e+1}}{z_e}\right)\right] \quad (5.6.1)$$

This directly yields an approximation for the gradients in the bulk material:

$$\frac{\partial u}{\partial x} \simeq \sum_{e=1}^{N} \mathfrak{Im}\left\{\left[\frac{\Theta'_{e+1}z_e - \Theta'_e z_{e+1}}{\pi h_e}\right]\log\left(\frac{z_{e+1}}{z_e}\right)\right\} \quad (5.6.2)$$
$$\frac{\partial u}{\partial y} \simeq \sum_{e=1}^{N} \frac{1}{\pi}\left[\Theta'_{e+1} - \Theta'_e + \mathfrak{Re}\left\{\left(\frac{\Theta'_{e+1}z_e - \Theta'_e z_{e+1}}{h_e}\right)\log\left(\frac{z_{e+1}}{z_e}\right)\right\}\right] \quad (5.6.3)$$

Similar to Equation 5.5.4, the approximations in Equations 5.6.1 through 5.6.3 hold anywhere in the body except on the crack face. The values of the gradient components are already formulated as functions $\theta'(x)$ and $\theta_y(x)$. The required accuracy is achieved by using h-refinement (decrease h_e, or conversely increasing N) where the largest error is near the crack itself.

6 - Results

6.1 Comparison to Classical Solution ($\gamma = 0$)

The solution to the classical anti-plane crack problem has been worked out by Muskhelishvili [21, 19] and Sih [31]. Starting with Equation 4.2.9 and letting the surface parameter (γ) equal zero, there should be convergence to the solution of the classic boundary value problem from Section 3.2. The equivalent problem can be stated as Equation 4.2.9 with $\gamma = 0$, such that:

$$[\phi'(t)]^+ + [\phi'(t)]^- = -2i\tilde{P}(t) \tag{6.1.1}$$

Alternatively, use Equation 4.4.16 with $\gamma = 0$ to get a Fredholm Equation of the First Kind [23]:

$$-\frac{1}{\pi}\int_{-1}^{1} \theta_o(t) \ln|t - x| dt = \zeta_2(x) - C_1 x - C_2 \tag{6.1.2}$$

Where θ_o is defined as θ with no surface effects. The known analytical solution of Equation 6.1.1 is [21, 19]:

$$\phi'(z) = -\frac{1}{\pi}\int_L \tilde{P}(t)\sqrt{\frac{t^2-1}{z^2-1}}\frac{dt}{t-z} \tag{6.1.3}$$

Note that:

$$\int_{-1}^{1} \frac{\sqrt{t^2-1}}{t-z} dt = \pi i \left(\sqrt{z^2-1} - z\right) \tag{6.1.4}$$

Then the direct solution for Equation 6.1.3 with a constant input function (assume $\tilde{P} = -1$ for convenience) is:

$$\phi'(z) = i\left[1 - \frac{z}{\sqrt{z^2-1}}\right] \tag{6.1.5}$$

Using the relation from Equation 4.1.9, the gradient components are:

$$\frac{\partial u}{\partial x} = \mathfrak{Re}\left\{\phi'(z)\right\} = \mathfrak{Im}\left\{\frac{z}{\sqrt{z^2-1}}\right\} \tag{6.1.6}$$

$$\frac{\partial u}{\partial y} = -\mathfrak{Im}\left\{\phi'(z)\right\} = -1 - \mathfrak{Re}\left\{\frac{z}{\sqrt{z^2-1}}\right\} \tag{6.1.7}$$

The displacement is found by integrating Equation 6.1.5 once more:

$$\phi(z) = \int \phi'(z)dz = i\left[\int dz - \int \frac{z}{\sqrt{z^2-1}}dz\right] = i\left[z - \sqrt{z^2-1}\right] + C$$

Where C is a complex constant of integration. Note that the constant C must be purely complex since at $z = \pm 1$, $\mathfrak{Re}\left\{\phi(\pm 1)\right\} = 0$. So, the displacement anywhere in the plane is given by:

$$u(x,y) = \mathfrak{Re}\left\{\phi(z)\right\} = -\mathfrak{Im}\left\{z - \sqrt{z^2-1}\right\} \tag{6.1.8}$$

The unit displacement on the crack face (when $z = x + i0^+$ and $|x| \leq 1$) has a circular/elliptical shape:

$$u(x,0^+) = \theta_o(x) = \sqrt{1-x^2}, \qquad -1 \leq x \leq 1 \tag{6.1.9}$$

The result in Equation 6.1.9 also matches the result by Broberg [32] for the shape of a crack face for quasi-static anti-plane displacement with no surface effects. The gradient components on the crack face are:

$$\frac{\partial u}{\partial x}(x, 0^+) \equiv \theta_o'(x) = -\frac{x}{\sqrt{1-x^2}}, \qquad -1 < x < 1 \tag{6.1.10}$$

$$\frac{\partial u}{\partial y}(x, 0^+) \equiv \theta_{oy}(x) = -1, \qquad -1 < x < 1 \tag{6.1.11}$$

Note the singularities in both gradient components at the crack tips (when $z = \pm 1$). This limits the use of these formulations and highlights the major problem with the classical case. The classical case does show realistic values for displacement across the crack and in the body, however the singularities in the gradient elements (which are linearly proportional to the stresses) make it impossible to evaluate stresses at, or near the crack tips. Even though this inconsistency exists, the classical model is useful in highlighting that there are stress concentrations at crack tips.

Plotting Equations 6.1.9 and 6.1.10 against the numerical solutions from Sections 5.3 and 5.4 respectively (using $\gamma = 0$ and $\tilde{P} = -1$) shows a strong correlation using just 16 elements for the displacement and 64 elements for the slope - see Figure 6.1. It should also be noted that Equations 5.4.10 and 6.1.11 produce the same result when $\gamma = 0$, including the singularity at the crack tips. This singularity for $\theta_o(\pm)$ is there regardless of the value of γ, as proven in Section 4.4. Given these results, it is concluded that the function in Equation 6.1.9 is the analytical solution of the Fredholm Equation 6.1.2 and the following limits hold:

$$\begin{aligned} &\lim_{\gamma \to 0} \theta^{(n)}(x) = \theta_o^{(n)}(x) \\ &\lim_{\gamma \to 0} \theta_y(x) = \theta_{oy}(x) \end{aligned} \tag{6.1.12}$$

See Figure 6.2 for a comparison of contour displacement plots in the positive complex plane ($y \geq 0$) between Equation 6.1.8 (Figure 6.2a) and

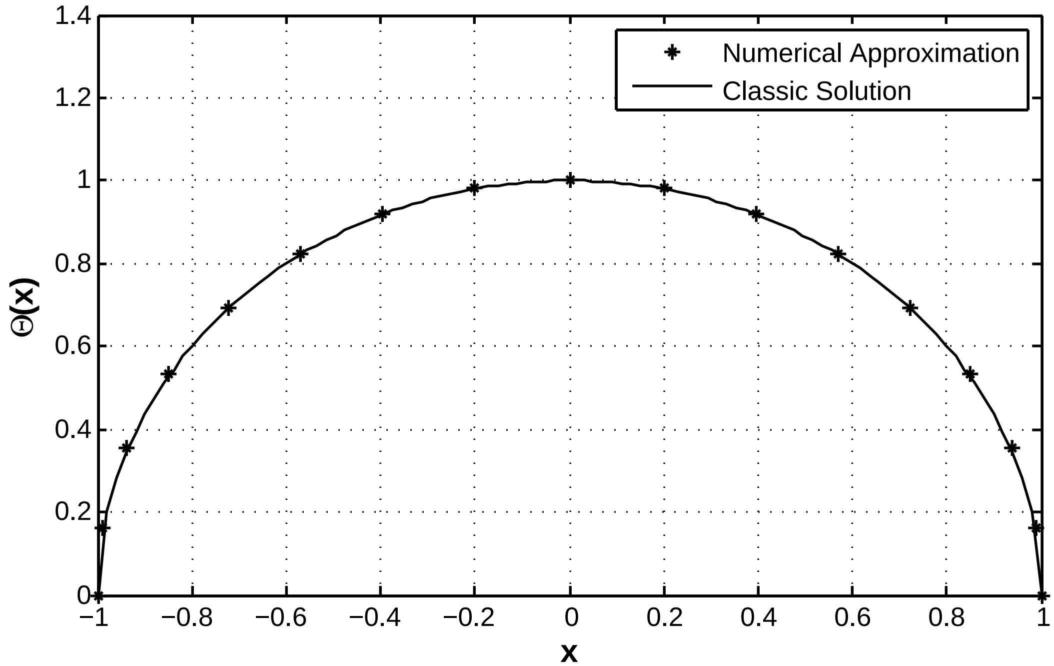

(a) Classical Solution from Equation 6.1.9 versus Approximated Displacement from Section 5.3 ($N = 16$)

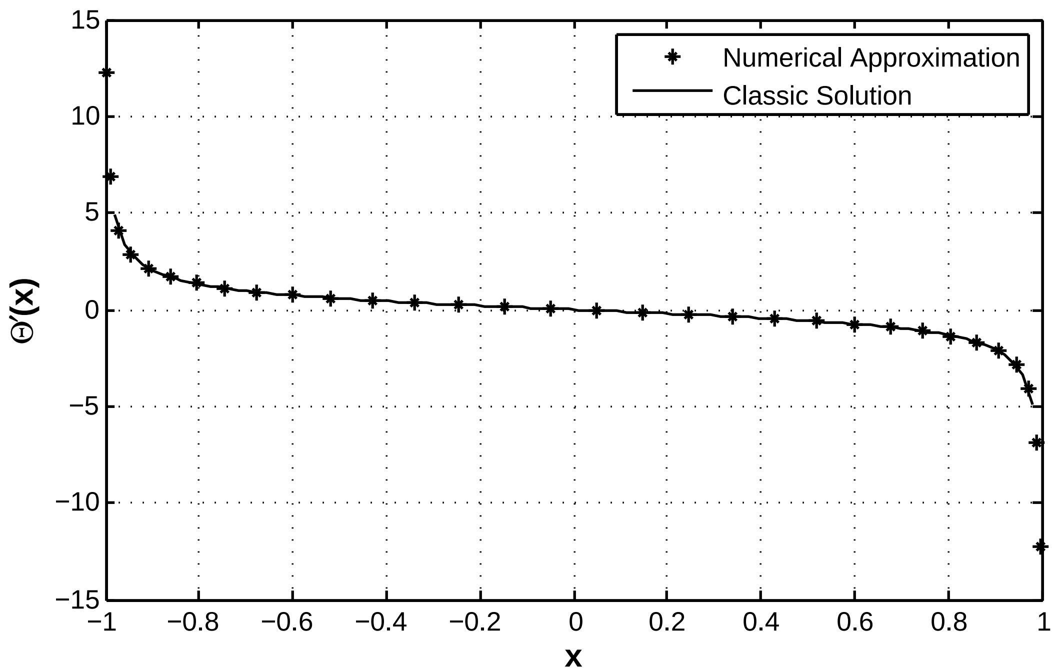

(b) Classical Solution from Equation 6.1.10 versus Approximated Slope from Section 5.4 ($N = 64$, endpoints not shown)

Figure 6.1: Displacement and Slope on Crack Face, where: $\tilde{P} = -1$, $\gamma = 0$

the numerical solution from Section 5.5 (Figure 6.2b). In this case, the difference between the plots is indistinguishable, which lends more validity to the numerical model formulations in Chapter 5. The solution in the negative complex plane ($y \leq 0$) is just the negative value of the positive plane ($u^+ = -u^-$) so this portion was not plotted here.

Using other input stress loads ($P \neq const$) for this comparison is assumed to correlate, however the analytical formulations of the integral from Equation 6.1.3 are difficult for anything other than an input stress on the crack face $\sigma_{23}(x, 0^{\pm}) = P(x) = const$ (or $\tilde{P}(x) = \pm 1$) and is beyond the scope of this study.

6.2 Effect of Input Load Profiles ($\tilde{P}(x)$)

Testing of the numerical model was done using various input loading profiles (and different values of γ). Figures 6.3 through 6.10 are plots of solutions from input stress profiles of increasing polynomial order and show reasonable results. The similarities included for each case are:

1. The displacement at the crack tips ($x = \pm 1$) is always zero (the boundary condition in Equation 4.4.17).

2. The maximum displacement is reduced when γ increases, which complies with the GM constitutive model from Section 2.3.

3. The slope function (hence the shear stress σ_{13}) at the crack tips ($\theta'(\pm 1)$) is reduced when γ increases and finite when $\gamma \neq 0$.

4. The area of the slope curves ($\theta'(x)$) above and below the x-axis is the same (the anti-symmetric condition in Equation 4.4.18).

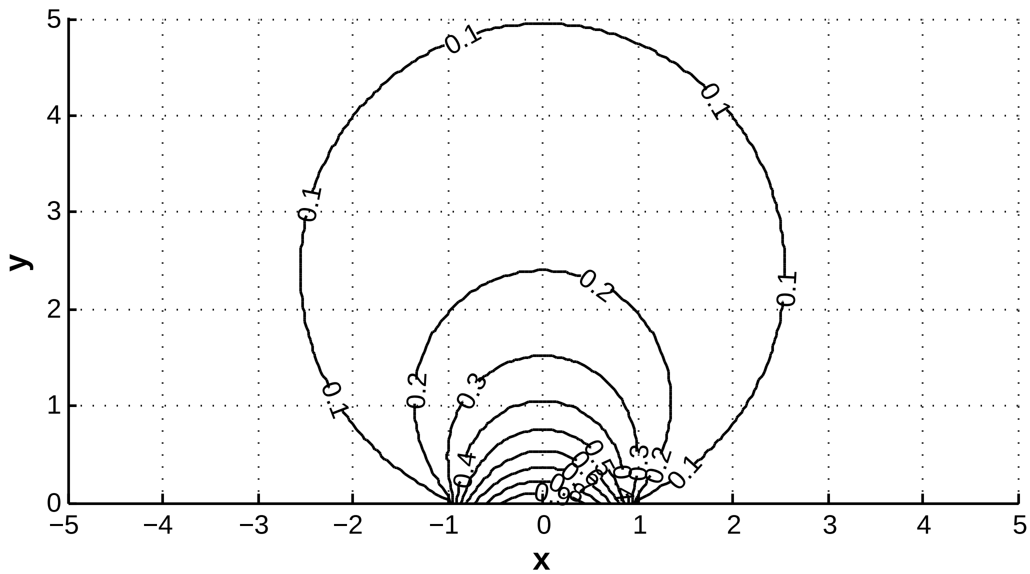

(a) Classical Solution from Equation 6.1.8

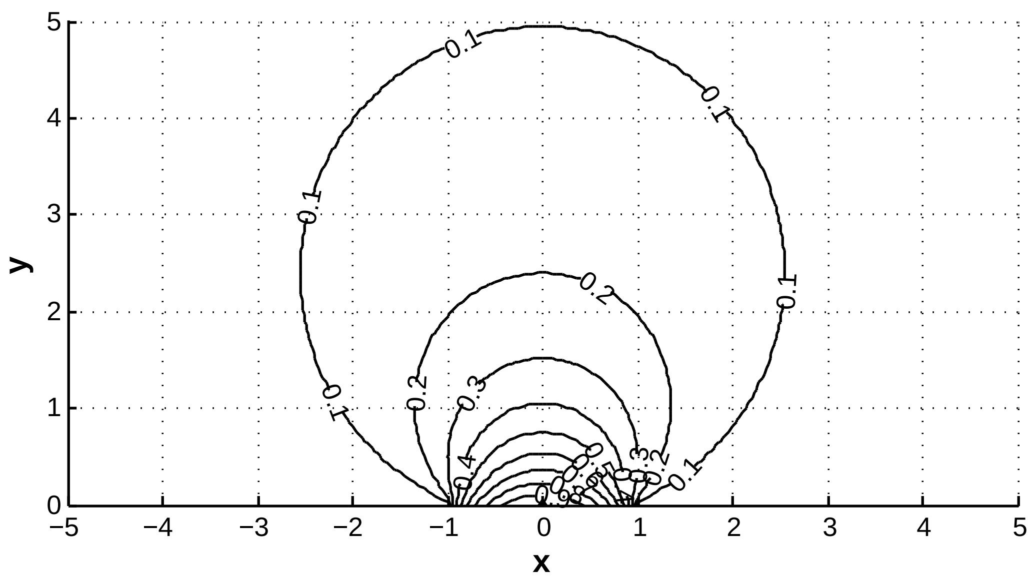

(b) Numerical Solution from Equation 5.5.4 using 50 elements along the crack face.

Figure 6.2: Comparison of classic anti-plane crack displacement and the numerical solution with no surface effects ($\gamma = 0$), where: $P_o = -1$

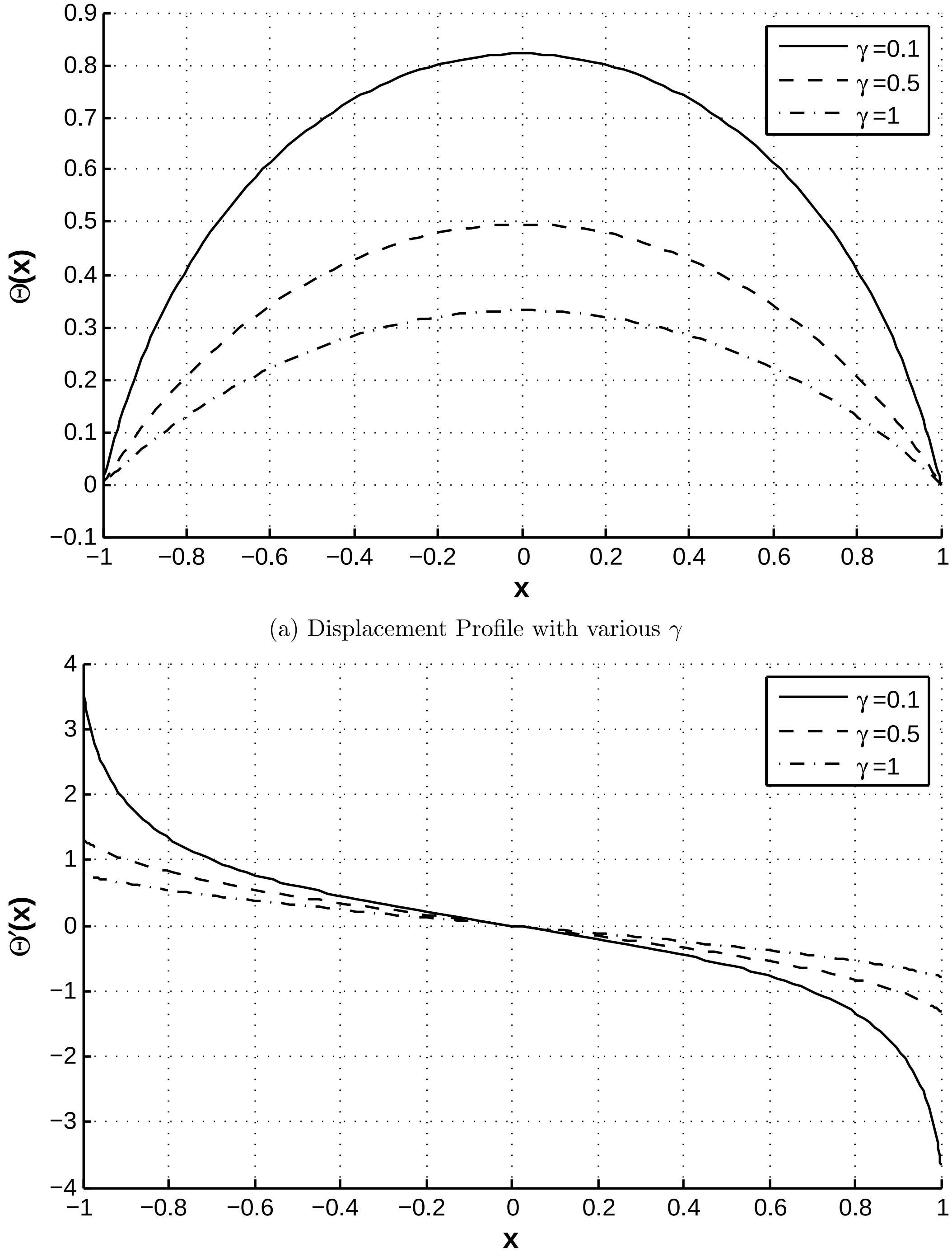

(a) Displacement Profile with various γ

(b) Slope Profile with various γ

Figure 6.3: Crack face displacement and slope ($\tilde{P} = -1$ and various γ)

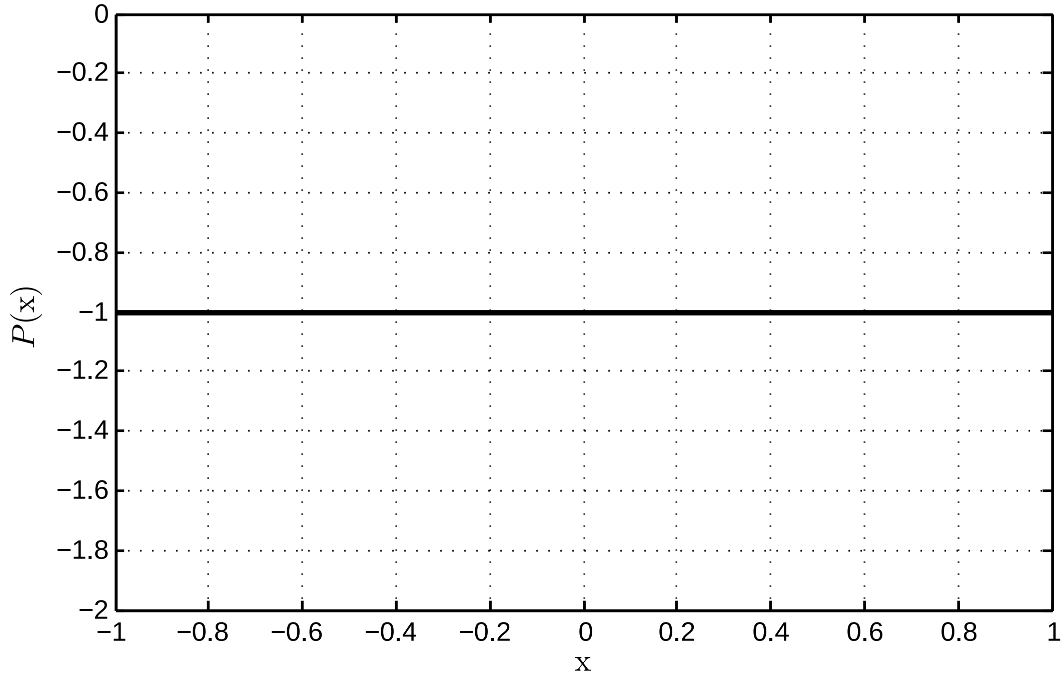

(a) Input Stress Function ($\tilde{P}(x)$)

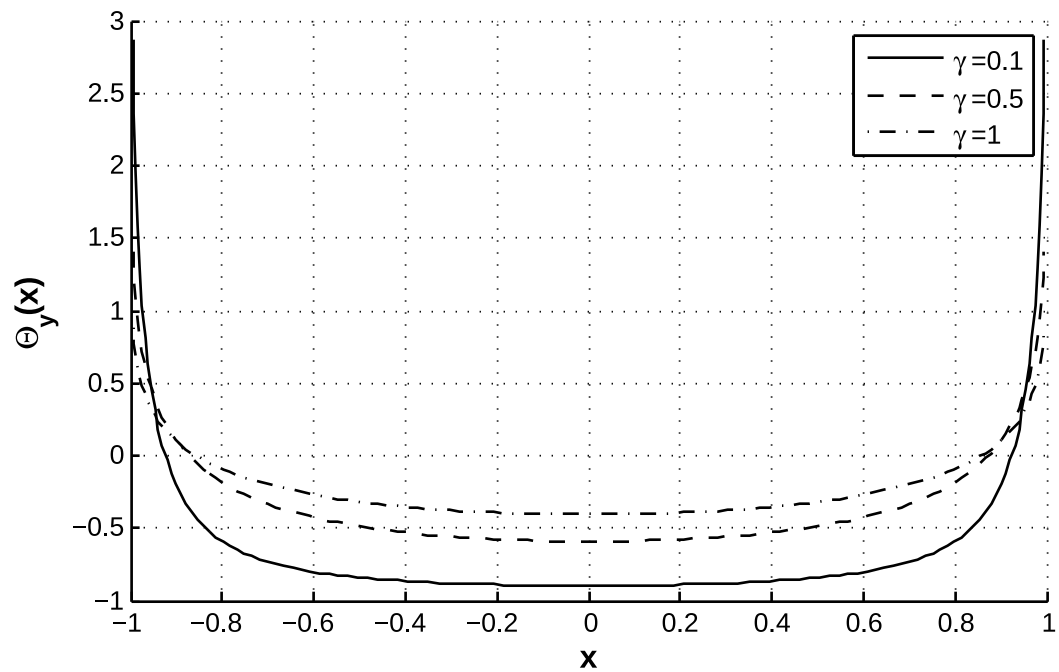

(b) Adjusted Input Stress Function ($\theta_y(x)$), end points not shown

Figure 6.4: Applied and Adjusted Input Stress ($\tilde{P} = -1$ and various γ)

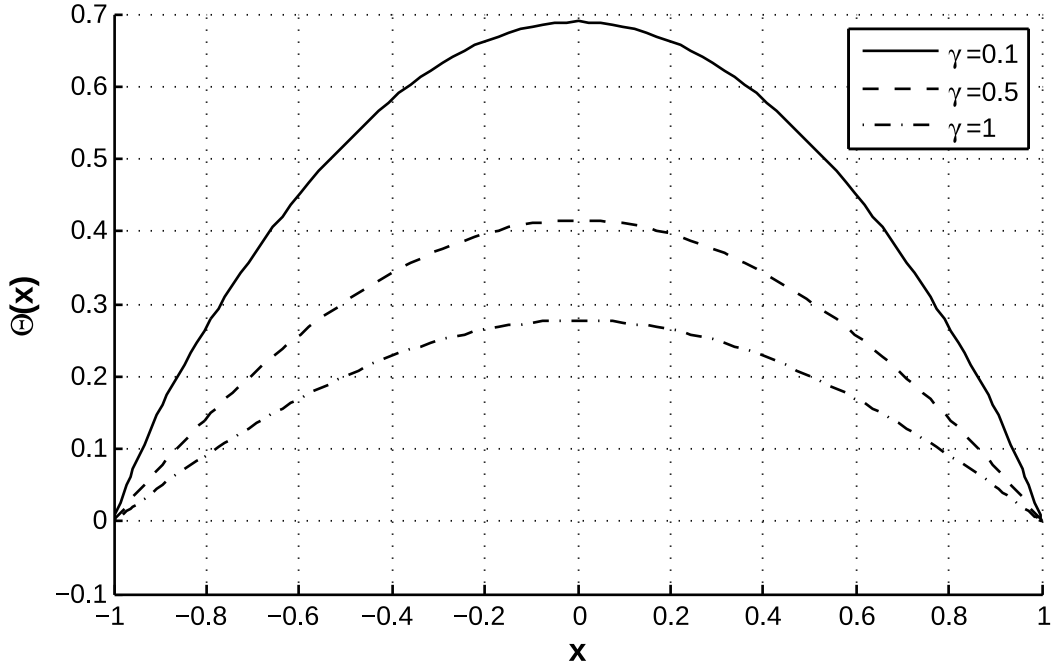

(a) Displacement Profile with various γ

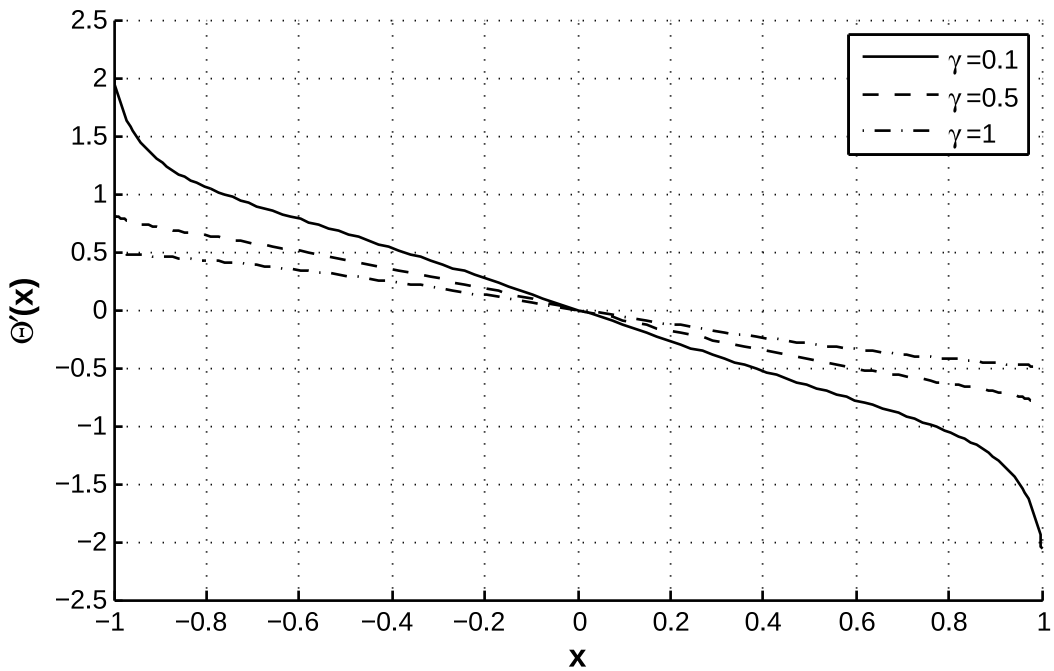

(b) Slope Profile with various γ

Figure 6.5: Crack face displacement and slope ($\tilde{P} = x^2 - 1$ and various γ)

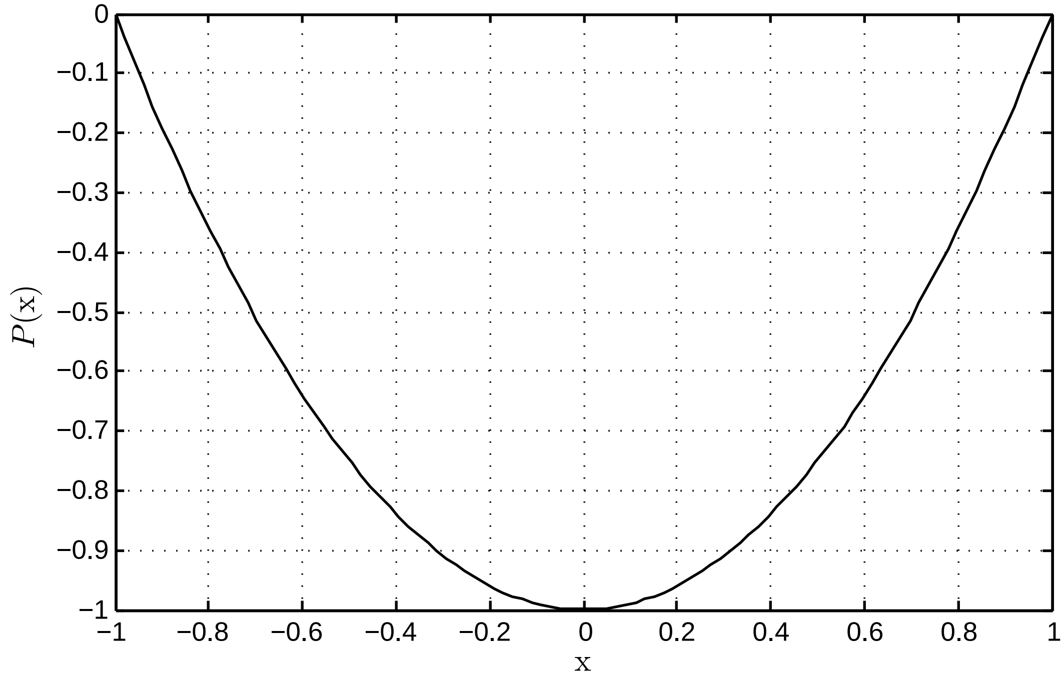

(a) Input Stress Function ($\tilde{P}(x)$)

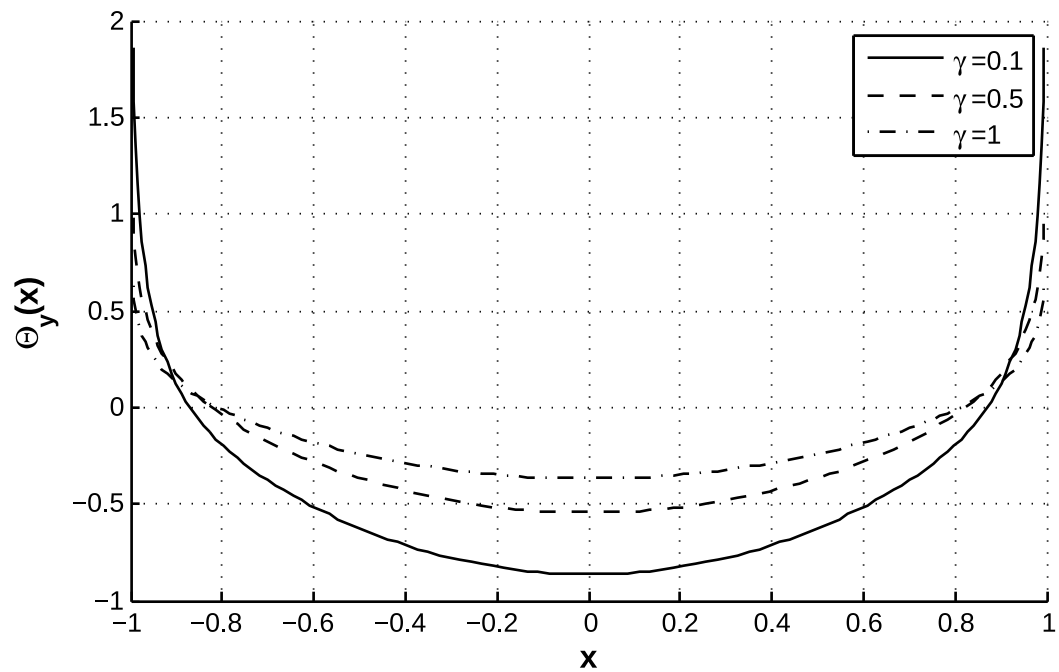

(b) Adjusted Input Stress Function ($\theta_y(x)$), end points not shown

Figure 6.6: Applied and Adjusted Input Stress ($\tilde{P} = x^2 - 1$ and various γ)

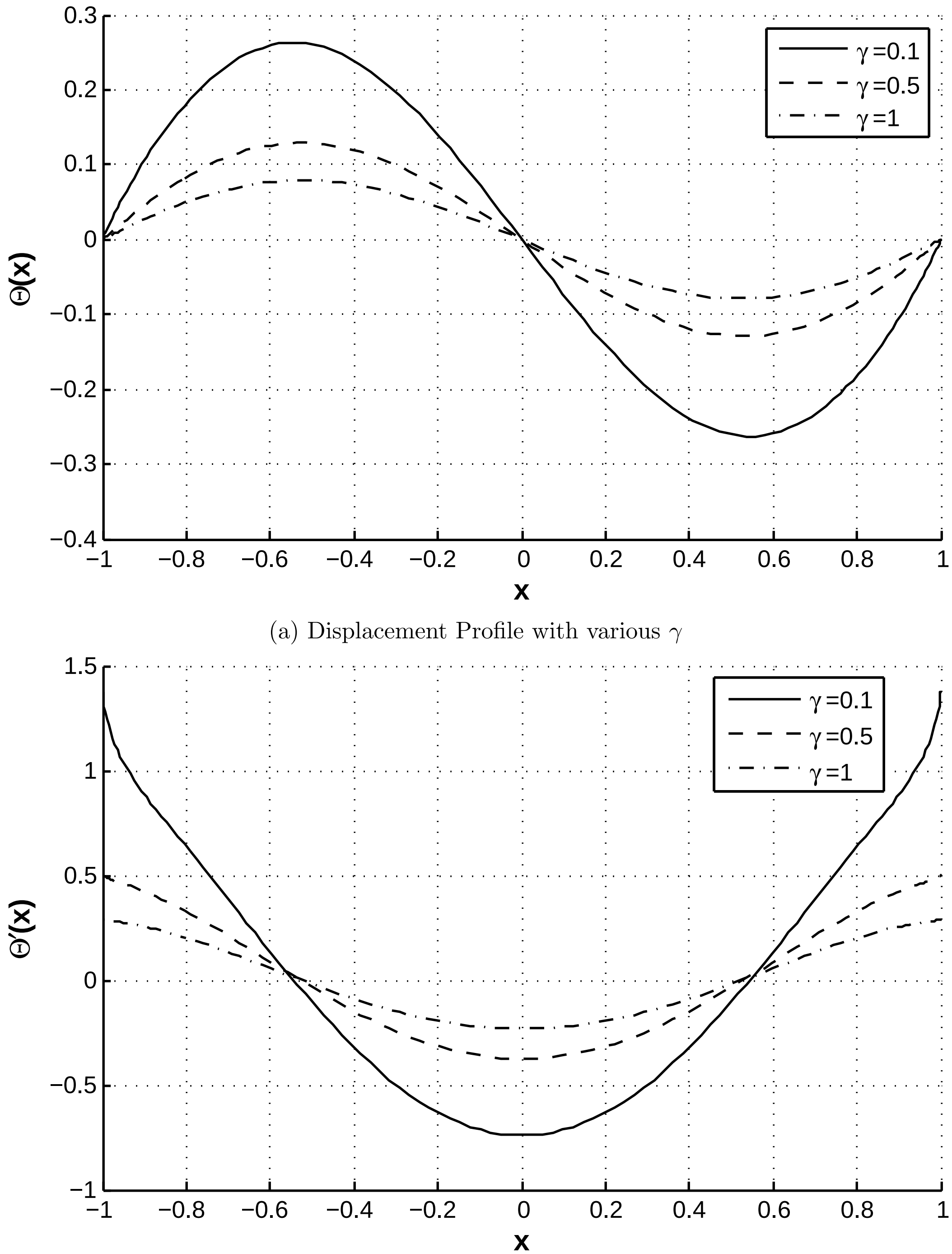

(a) Displacement Profile with various γ

(b) Slope Profile with various γ

Figure 6.7: Crack face displacement and slope ($\tilde{P} = -\frac{3\sqrt{3}}{2}x(x-1)(x+1)$ and various γ)

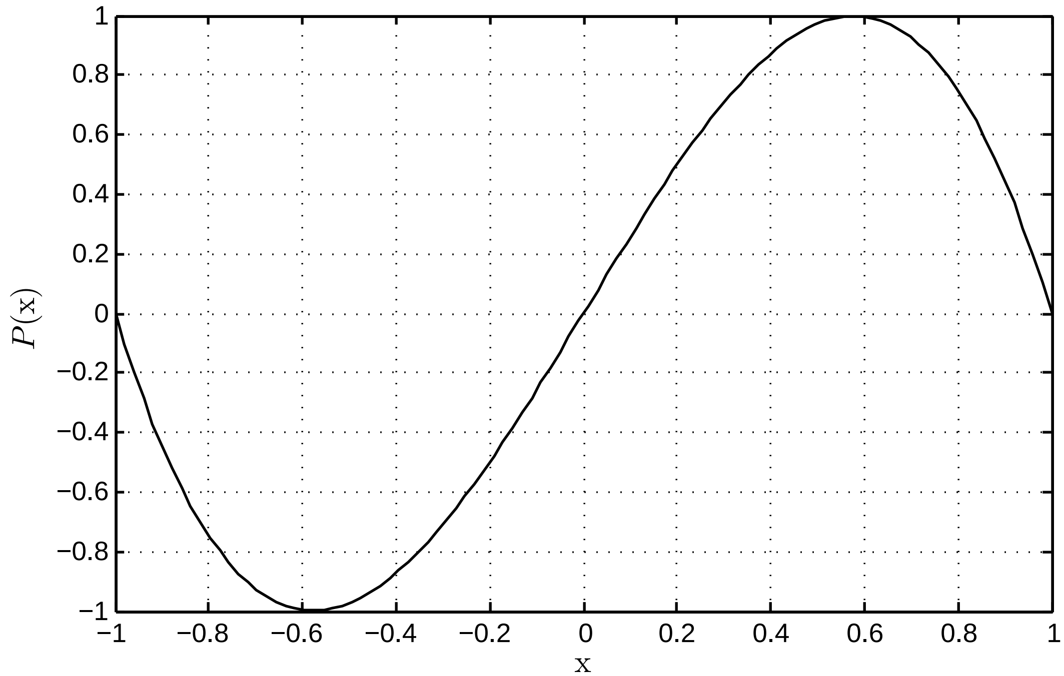

(a) Input Stress Function ($\tilde{P}(x)$)

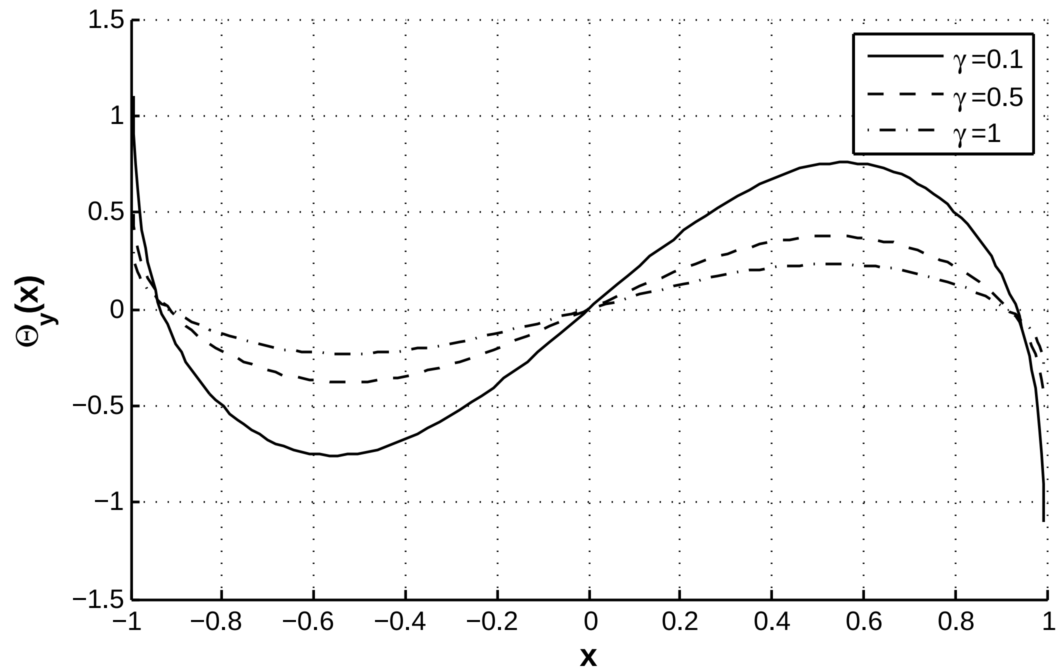

(b) Adjusted Input Stress Function ($\theta_y(x)$) , end points not shown

Figure 6.8: Applied and Adjusted Input Stress ($\tilde{P} = -\frac{3\sqrt{3}}{2}x(x-1)(x+1)$ and various γ)

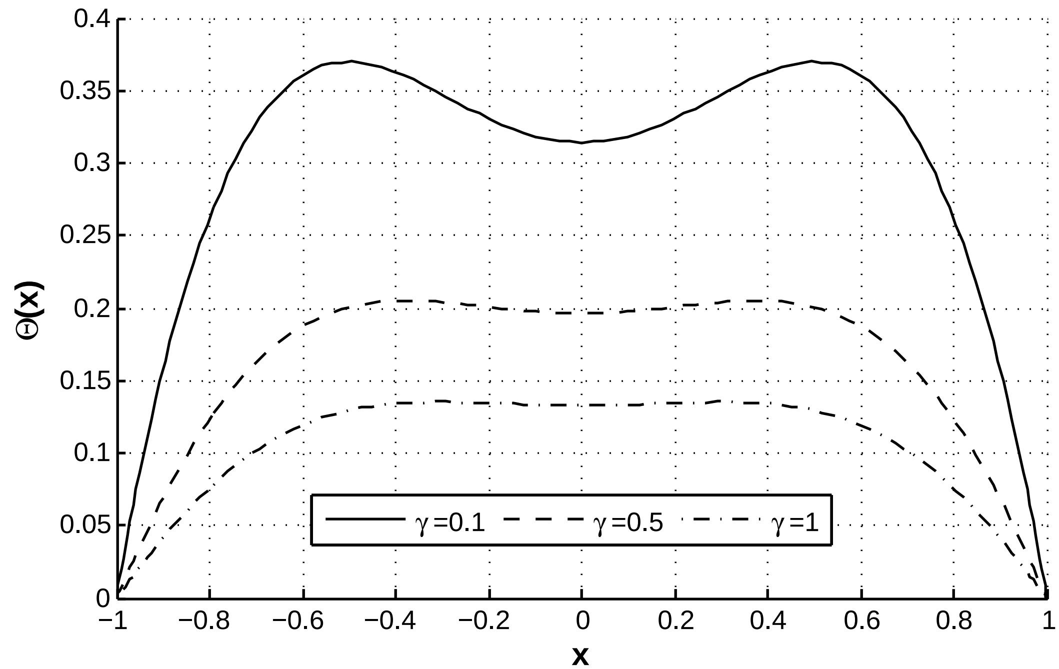

(a) Displacement Profile with various γ

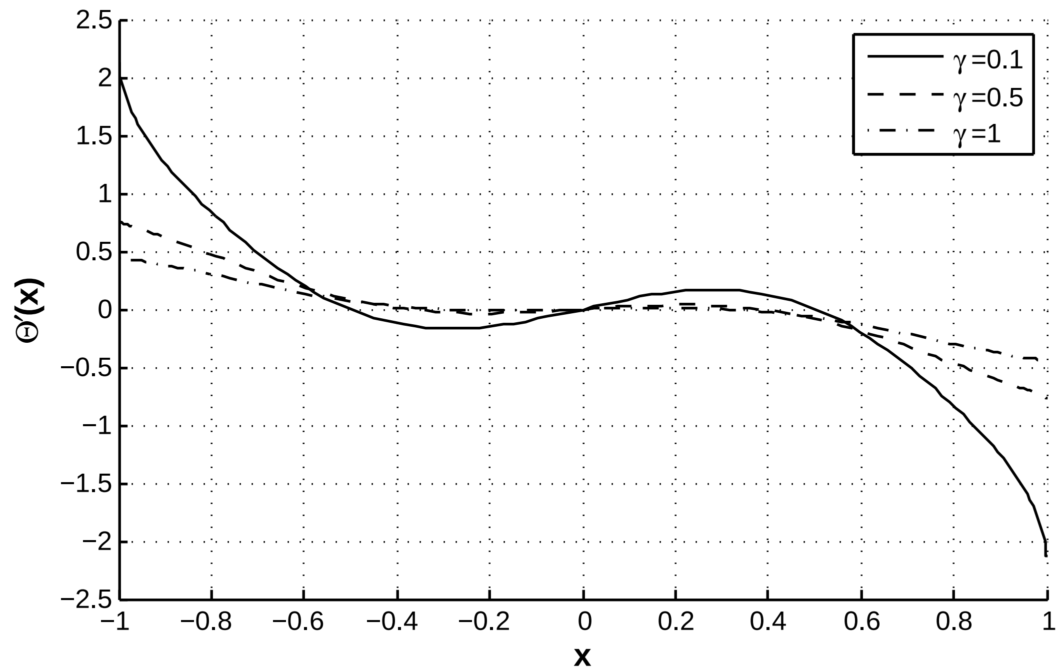

(b) Slope Profile with various γ

Figure 6.9: Crack face displacement and slope ($\tilde{P} = x^2 (x-1)(x+1)$ and various γ)

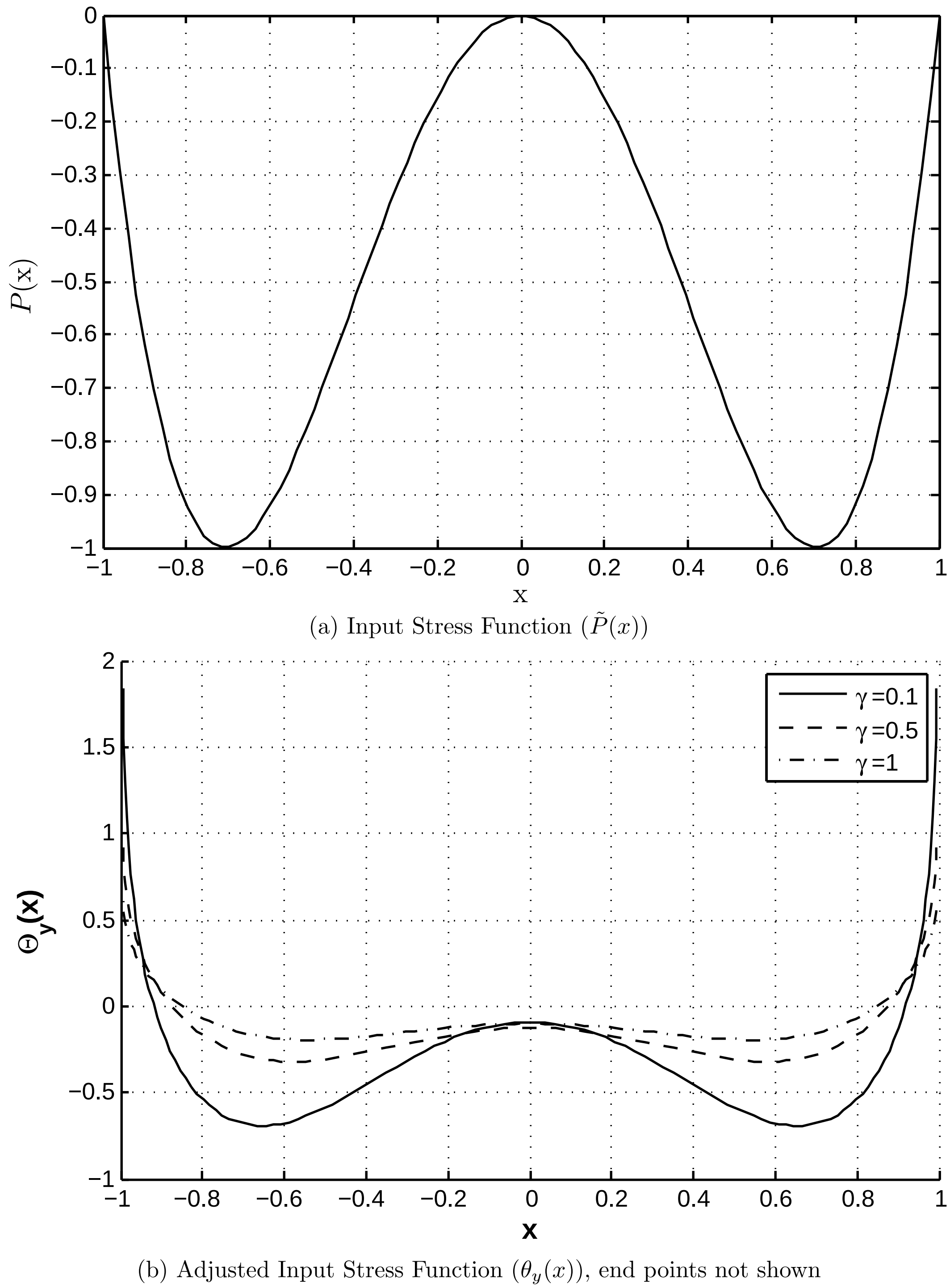

(a) Input Stress Function ($\tilde{P}(x)$)

(b) Adjusted Input Stress Function ($\theta_y(x)$), end points not shown

Figure 6.10: Applied and Adjusted Input Stress ($\tilde{P} = 4x^2\,(x-1)\,(x+1)$ and various γ)

5. The slope profiles ($\theta'(x)$) correlate to the displacement profiles ($\theta(x)$).

6. The displacement ($\theta(x)$) follows the direction of input traction.

7. The adjusted unit input stress ($\theta_y(x)$) magnitude across the crack face is lower than the input stress magnitude ($\tilde{P}(x)$) except for the endpoints.

8. Singularities (divergent computations) of the adjusted unit input stress (θ_y) exist at the crack tips for any value of γ (this was proven in Section 4.4).

For further testing of the numerical model, take an extreme case when $\tilde{P} = -1 + 2H(x)$, where $H(x)$ is the Heaviside Step Function. Figures 6.11 and 6.12 show the effect of this input with $\gamma = 0.1$. Figure 6.11a shows the displacement($\theta(x)$), slope ($\theta'(x)$) and adjusted input stress ($\theta_y(x)$) profiles across the crack face. Note that there is a cusp at $x = 0$, which is expected given the discontinuity of the input load ($\tilde{P}$). The body displacement plot (Figure 6.11b) shows inverted displacement across the x axis (matching the conditions that $u^+ = -u^-$) as well as the y axis (matching the direction of the input function). The body gradient plots (Figures 6.12a and 6.12b) also show expected results given that:

$$\frac{\partial u^+}{\partial x} = -\frac{\partial u^-}{\partial x} \quad \text{and} \quad \frac{\partial u^+}{\partial y} = \frac{\partial u^-}{\partial y}$$

6.3 Effect of Surface Parameter (γ)

Even though the numerical model can handle different input load profiles ($\tilde{P}(x)$), this is not necessarily required. If the crack length is "small," then the assumption that the input stress loading on the crack face is constant

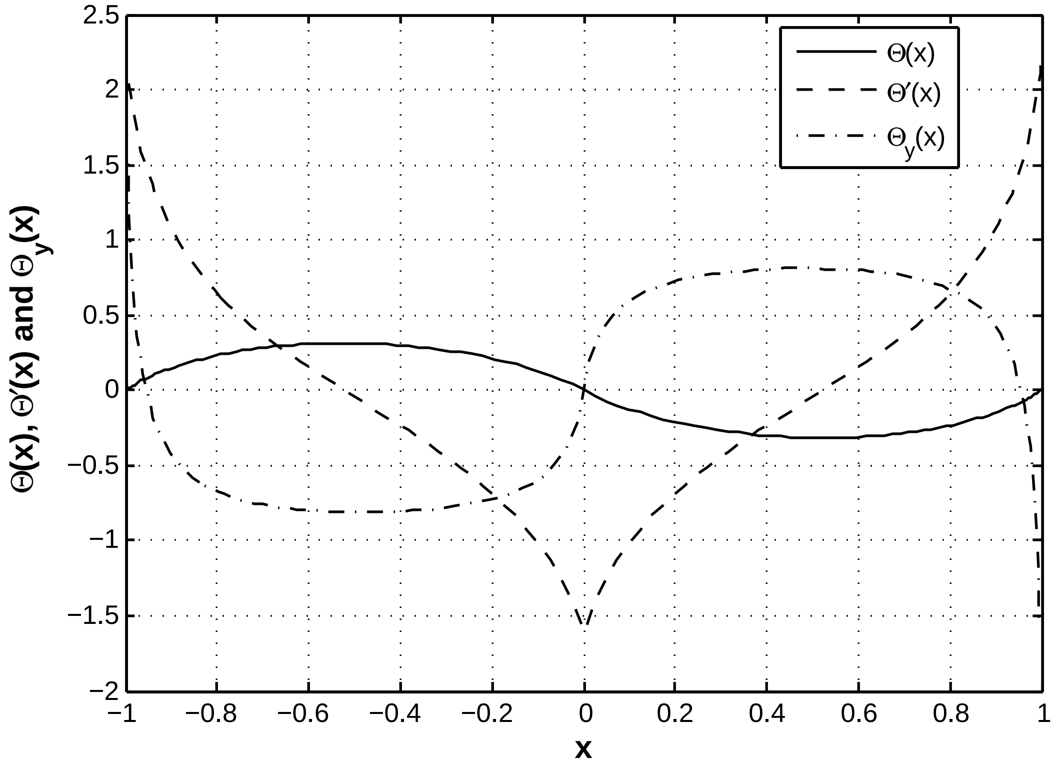

(a) $\theta(x)$), $\theta'(x)$, and $\theta_y(x)$ (end points not shown).

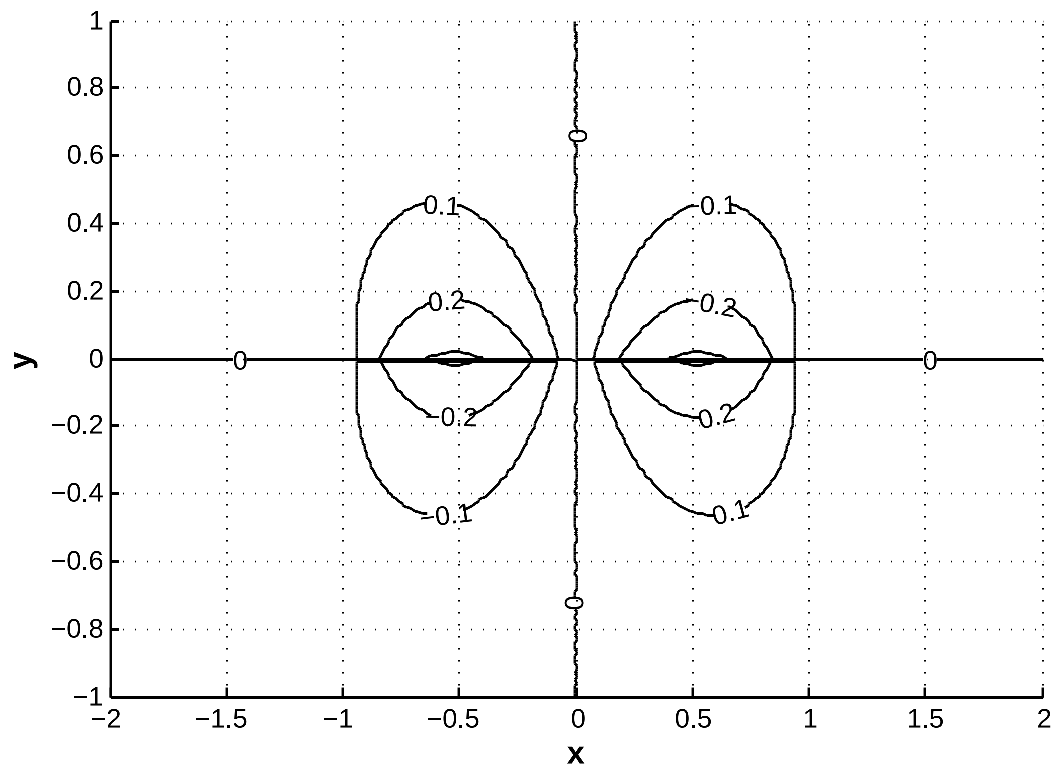

(b) Body displacement

Figure 6.11: Crack Face and Body Displacement ($\tilde{P} = -1 + 2H(x)$, $\gamma = 0.1$, $N = 128$)

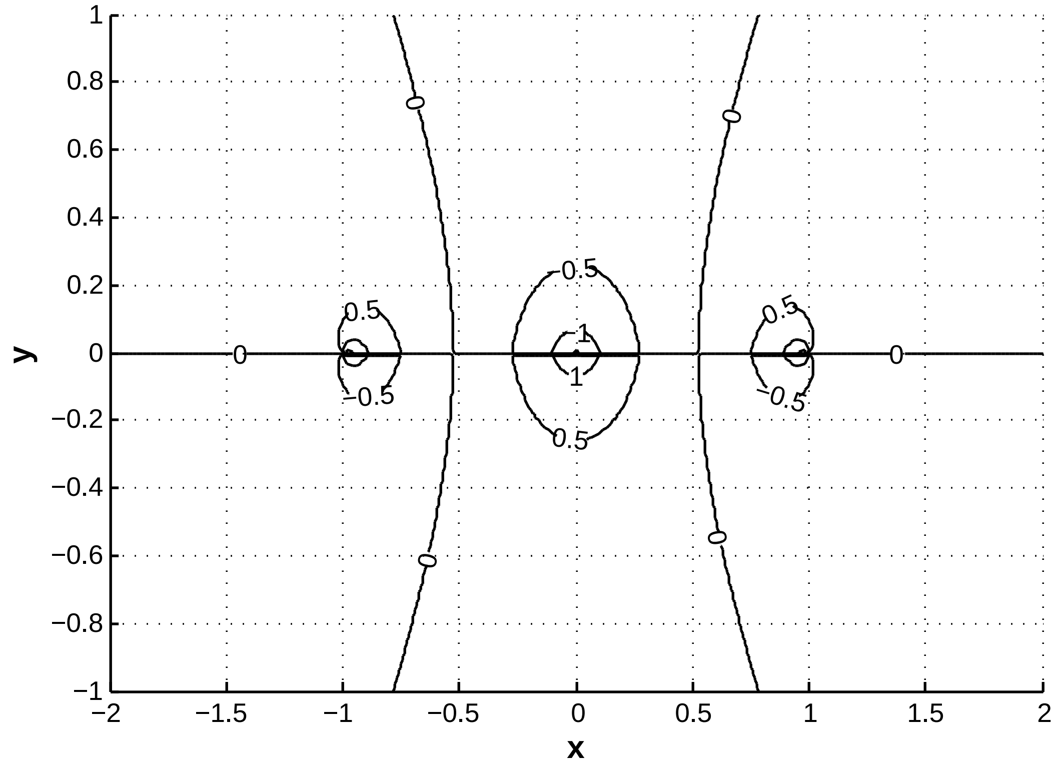

(a) $\frac{\partial u}{\partial x}$ in body.

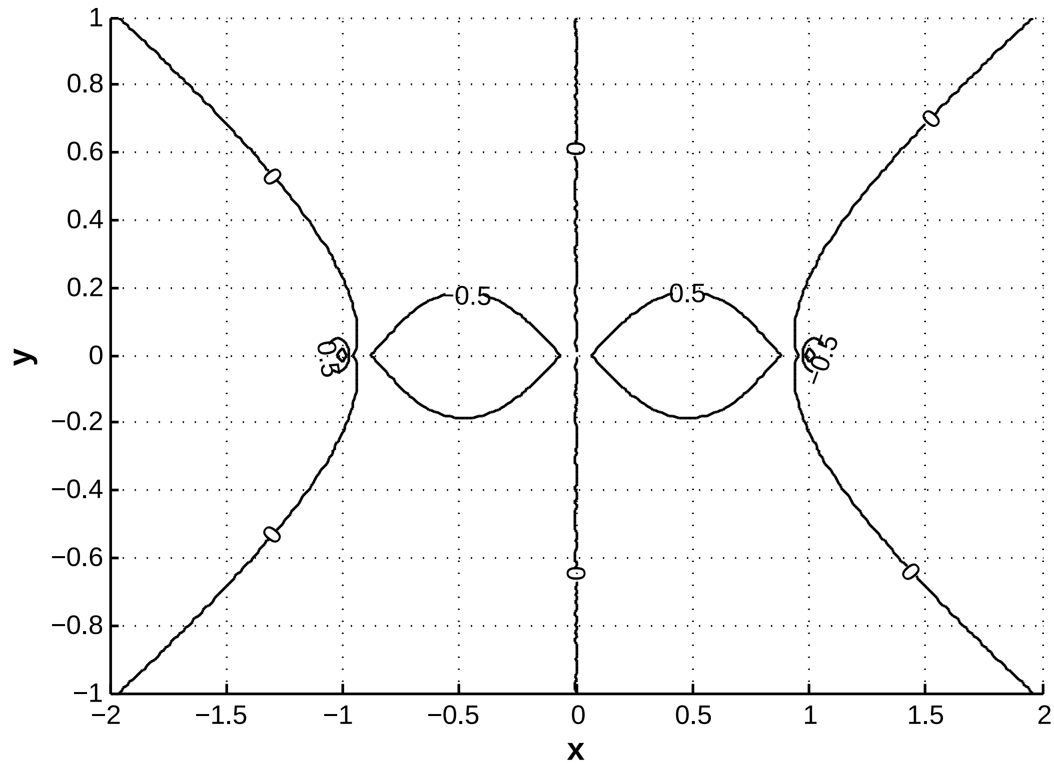

(b) $\frac{\partial u}{\partial y}$ in body.

Figure 6.12: Gradient components in body ($\tilde{P} = -1 + 2H(x)$, $\gamma = 0.1$, $N = 128$)

($\therefore \tilde{P} = \pm 1$) is adequate.

Figure 6.13 shows the reduced unit displacement ($\theta_{max} \equiv \theta(0)$) versus surface parameter (γ) using 50 elements ($N = 50$) and a constant stress input function ($\tilde{P} = \pm 1$). As shown in Figure 6.13a, when γ increases there is a reduction of maximum unit displacement on the crack face. This plot indicates that:

$$\lim_{\gamma \to \infty} \theta(0) = 0$$

When taking the inverse of the values in Figure 6.13a and re-plotting (Figure 6.13b), there is a very strong linear correlation ($R^2 = 0.9999765$) which resembles:

$$\theta_{max} \equiv \theta(0) \simeq \frac{1}{2\gamma + 1} \tag{6.3.1}$$

Figure 6.13c shows the absolute difference (Δ) from this data set between the numerically computed values and Equation 6.3.1, where:

$$\Delta(\gamma) \equiv \left| \theta_{max} - \frac{1}{2\gamma + 1} \right| \tag{6.3.2}$$

The maximum difference of this data set was found to be 0.0121 (or 1.21%) when $\gamma = 0.069$. This estimate is quite reasonable and noting that $\theta_o(0) = 1$, then Equation 6.3.1 is an acceptable estimate for maximum displacement reduction ($\theta(0)/\theta_o(0)$) as a function of γ.

As γ increases, the displacement profile across the crack also changes from an elliptic/circular shape to one resembling a quadratic function. This leads

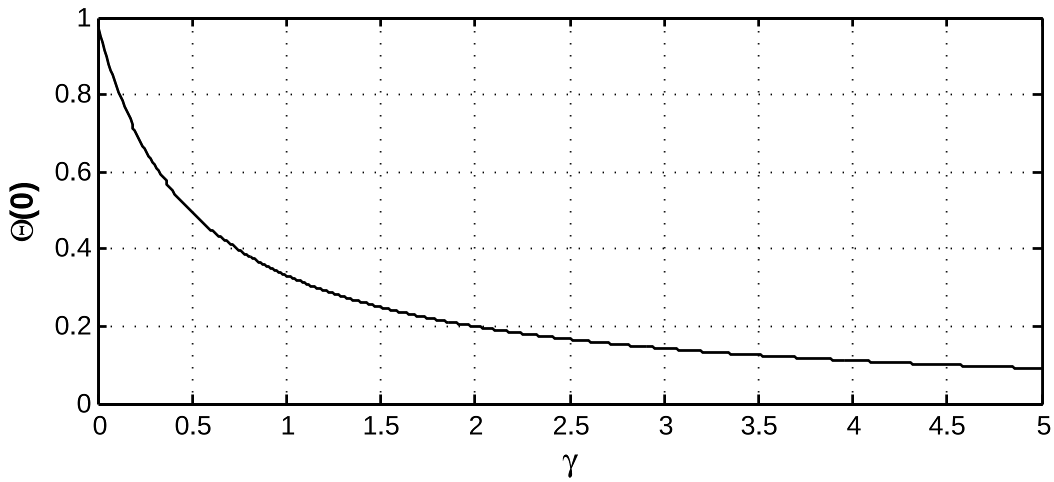

(a) $\theta(0)$ versus γ

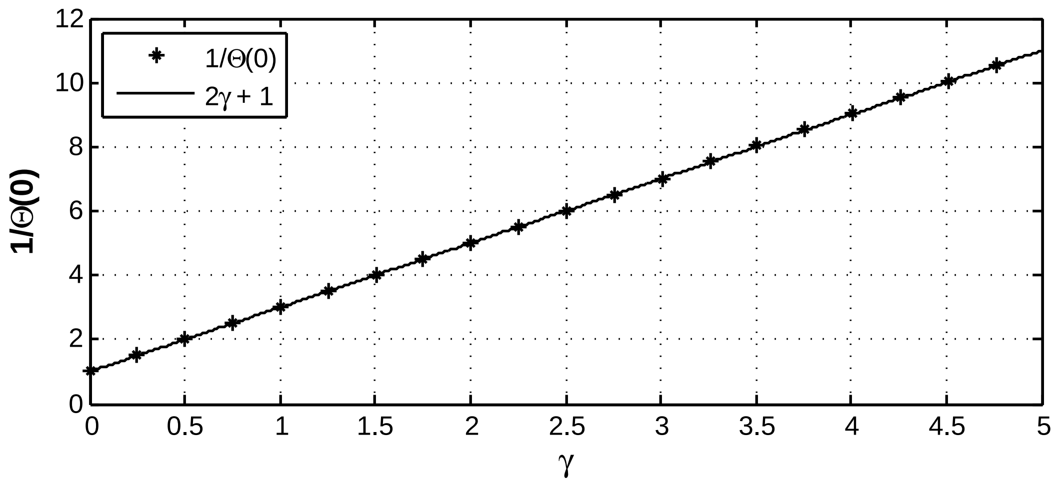

(b) $1/\theta(0)$ versus γ with linear fit.

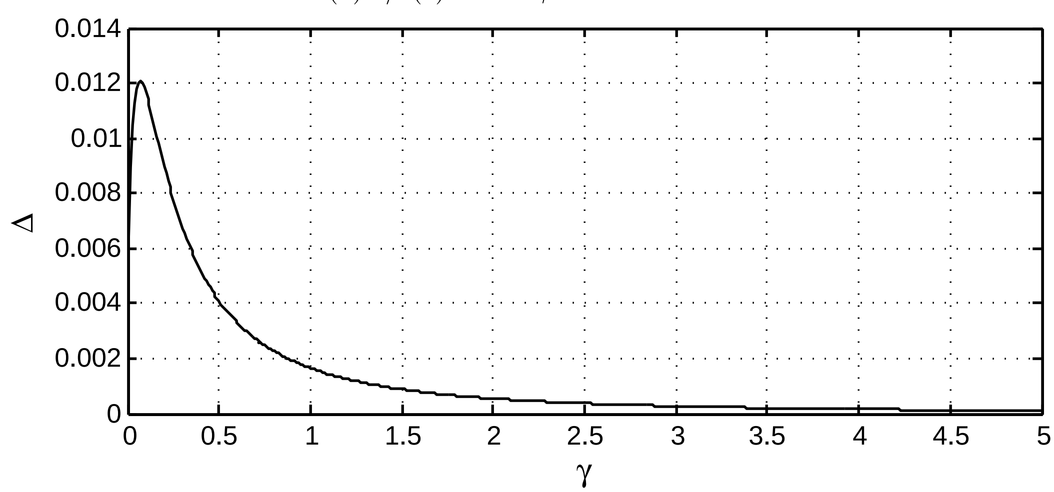

(c) Difference between numerical data and linearized approximation versus γ

Figure 6.13: Effect of Surface Parameter (γ) on maximum crack face displacement with constant stress input ($\tilde{P} = \pm 1$).

to the following hypothesis for an approximation anywhere along the crack face:

$$\theta(x) \simeq \theta_{max} \left[\theta_o(x)\right]^K \tag{6.3.3}$$

To linearize this equation, take the natural log of each side:

$$\ln(\theta) = K \ln(\theta_o) + \ln(\theta_{max})$$

By taking a series of linear interpolations a data set of K versus γ is retrieved and this plot set is shown in Figure 6.14. Figure 6.14a shows K versus γ directly (using 500 points). This plot set appears to have an asymptote at $K = 2$, and given that $K = 1$ when $\gamma = 0$ the following approximation is assumed:

$$\frac{1}{2-K} - 1 \simeq m\gamma \tag{6.3.4}$$

Figure 6.14b shows this plot set and m (a linear slope) is found to be approximately 13.8362 with an R^2 value of 0.99924 - indicating a strong linear fit. Solving for K in Equation 6.3.4 yields the following approximation:

$$\theta(x) \simeq \frac{\left(1-x^2\right)^{\left(\frac{2m\gamma+1}{2m\gamma+2}\right)}}{2\gamma+1} \tag{6.3.5}$$

Note that using this approximation:

$$\lim_{\gamma \to 0} K = \frac{1}{2}$$

$$\lim_{\gamma \to \infty} K = 1$$

Which matches what the proposed form of Equation 6.3.3. The relative

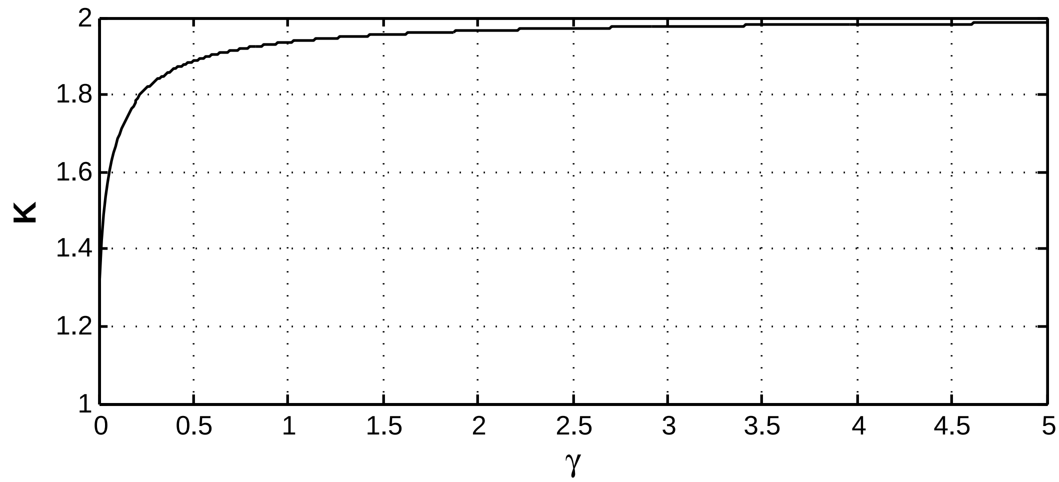

(a) K versus γ

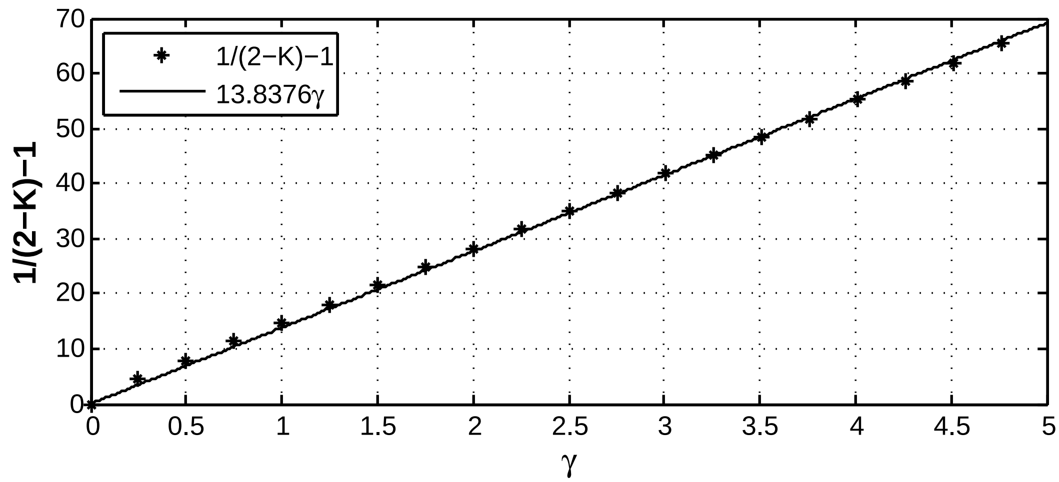

(b) $1/(2-K)-1$ versus γ

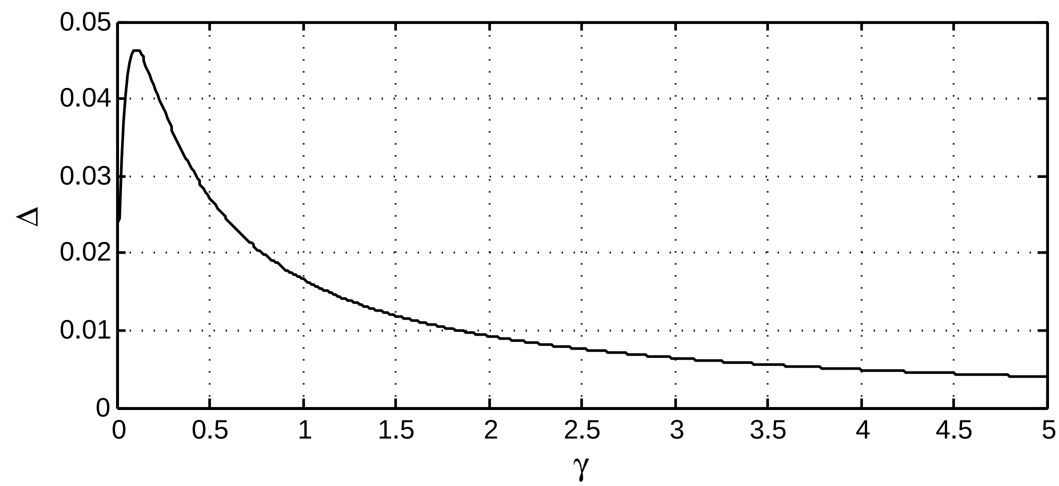

(c) Error in linearized approximation versus γ

Figure 6.14: Effect of Surface Effect Parameter (γ) on crack face displacement (shape) with constant stress input ($\tilde{P} = \pm 1$).

absolute difference (in %) between the approximation in Equation 6.3.5 is defined as:

$$\Delta(\gamma) \equiv \left| \frac{\theta(x)}{\theta_{max}} - \theta_o^K(x) \right|_{max}$$

This difference versus γ is plotted in Figure 6.14c and indicates a maximum relative difference to be approximately 4.53%. Given this, Equation 6.3.5 is an acceptable approximation for the crack shape profile with constant input load.

The effect of γ on the maximum slope of the crack face ($\theta'_{max} \equiv \theta'(-1)$) is plotted in Figure 6.15 with prescribed convergence error less than 1% (error is explained in Section 6.4). Noting that the slope is infinite at the crack tips with no surface effects ($\gamma = 0$), a plot of the inverse of this slope is shown in Figure 6.15a. Note that the plot is asymptotic to a linear function as γ increases. A reasonable curve fit approximation for the range of $\gamma < 1$ could not be found (see Figure 6.15b), however a linear fit for values of $\gamma > 1$ with an R^2 value of 0.99999 is given by:

$$\theta'_{max} \simeq \frac{1}{1.0057\gamma + 0.2863}, \qquad \gamma > 1 \tag{6.3.6}$$

Noting the result from Figure 6.15b, an inequality for any value of γ is:

$$\theta'_{max} \geq \frac{1}{1.0057\gamma + 0.2863} \tag{6.3.7}$$

The effect of γ on maximum adjusted input stress ($\theta_y(x)$) was not quantifiable due to the singularities in the model at the crack tips (discussed in Section 4.4). However, away from the crack tips there is a definite reduction of

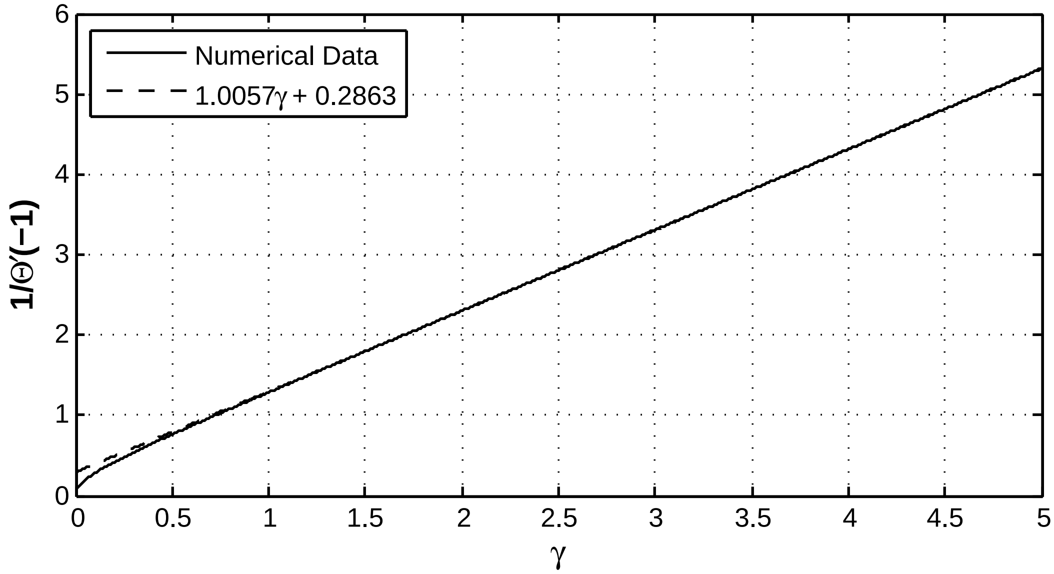

(a) $1/\theta'(-1)$ versus γ with asymptote

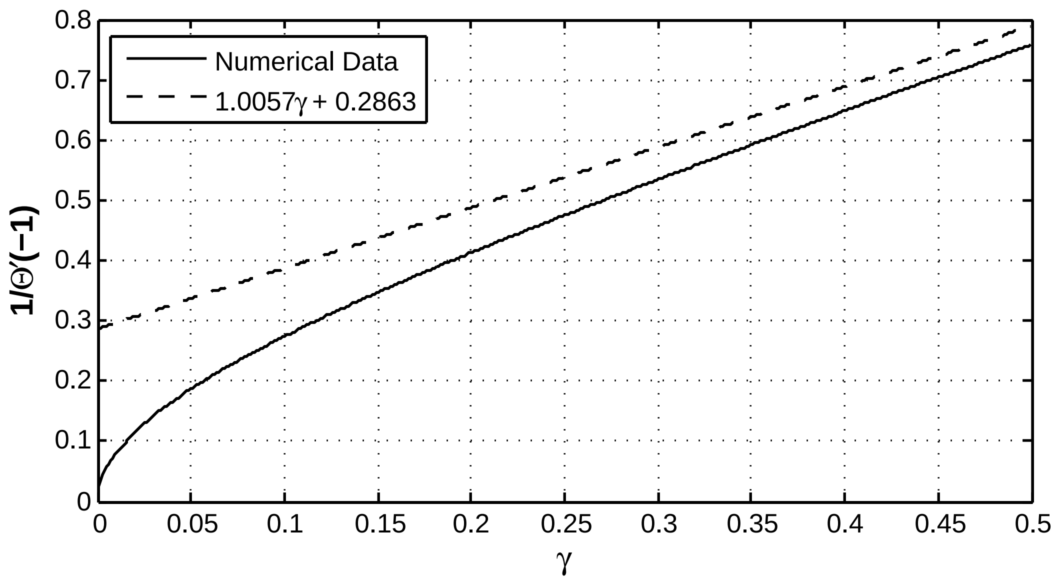

(b) $1/\theta'(-1)$ versus γ with asymptote ($\gamma < 0.5$)

Figure 6.15: Plot of the inverse of maximum slope versus surface effect parameter

input loading due to the surface effect. This can be seen in the previously presented Figures 6.4, 6.6, 6.8, 6.10 and 6.11a.

Figures 6.16 through 6.19 were constructed to quantify the effect of γ on the bulk material with a constant stress input ($\tilde{P} = -1$). When γ increases, there is a reduction in both the bulk material displacement and the total unit shear stress magnitude(τ), defined as:

$$\tau \equiv |\nabla u| = \sqrt{\left(\frac{\partial u}{\partial x}\right)^2 + \left(\frac{\partial u}{\partial y}\right)^2} = \frac{1}{P_o}\sqrt{\sigma_{13}^2 + \sigma_{23}^2} \qquad (6.3.8)$$

Clearly in each case, there are stress concentrations at the crack tips (which is expected). However, the radius of effect from these stress concentrations diminishes as γ increases. This reduction can be also quantified using linear curve fitting. Define the displacement variable ξ as a linear transformation along the x axis such that when $x = 1$, $\xi = 0$. So:

$$\xi(x) \equiv x - 1, \qquad\qquad x > 1$$

As shown in Figures 6.16a, 6.17a, 6.18a and 6.16a, as ξ increases ($x > 1$) the total stress reduces. Also, as γ increases, the distance from the crack tip (ξ) to any given value of unit shear stress decreases. Figure 6.20a shows this effect more clearly which shows plots of stress magnitude (τ) as a function of increasing ξ and γ. Note that the values of stress magnitude are infinite (and non-convergent) when $\xi \to 0$. Taking the square root and inverse of the data in Figure 6.20a provides very linear profiles except for the region very close to the crack ($\xi < 1$) - see Figure 6.20b.

Taking multiple linear curve fits of different values of γ (where $0 \leq \gamma \leq 5$),

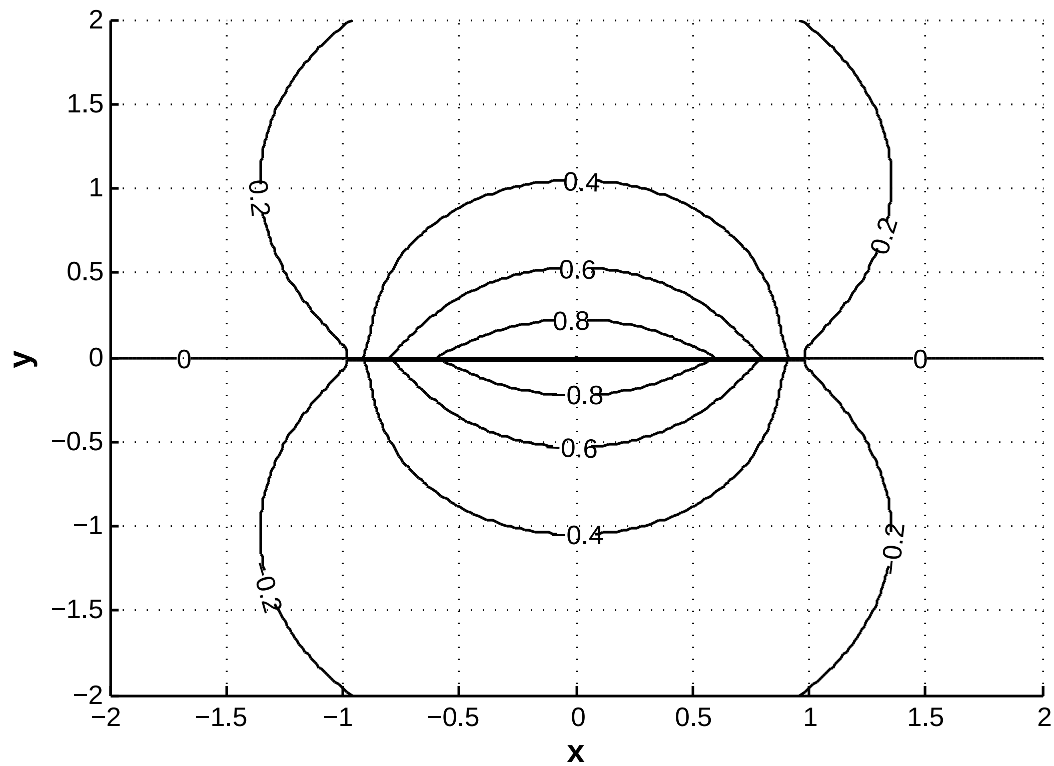

(a) Body Displacement

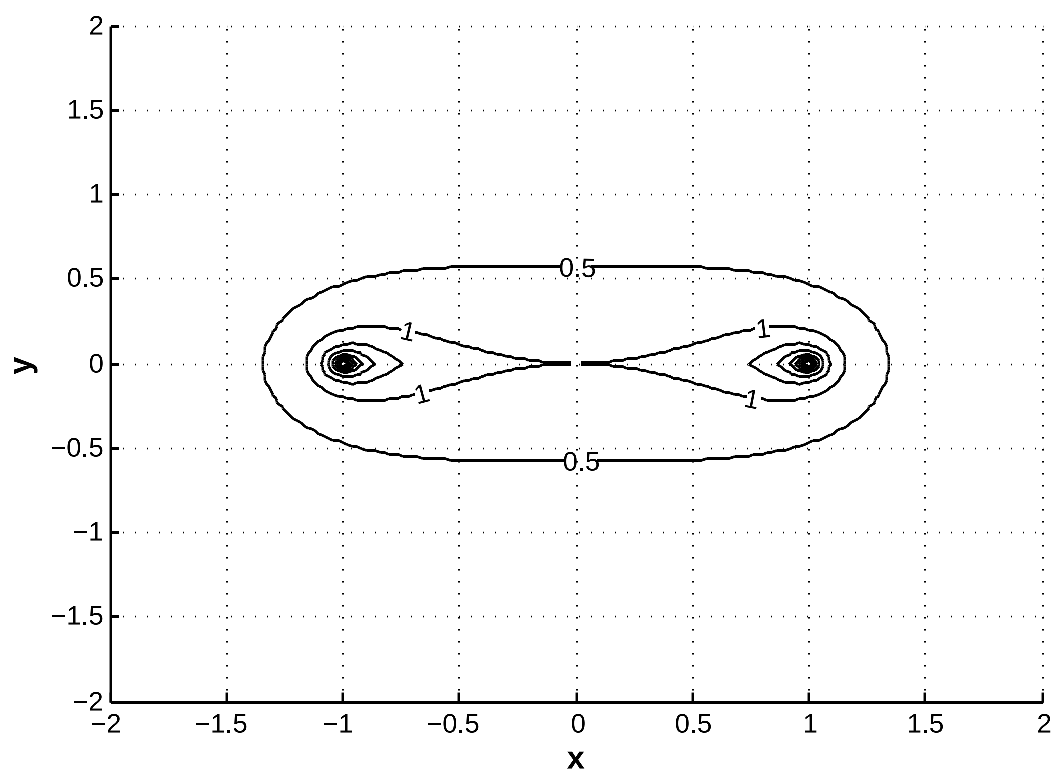

(b) Body Unit Stress Magnitude (τ)

Figure 6.16: Displacement and Unit Stress Magnitude in Body Material ($\tilde{P} = -1,\ \gamma = 0,\ N = 128$)

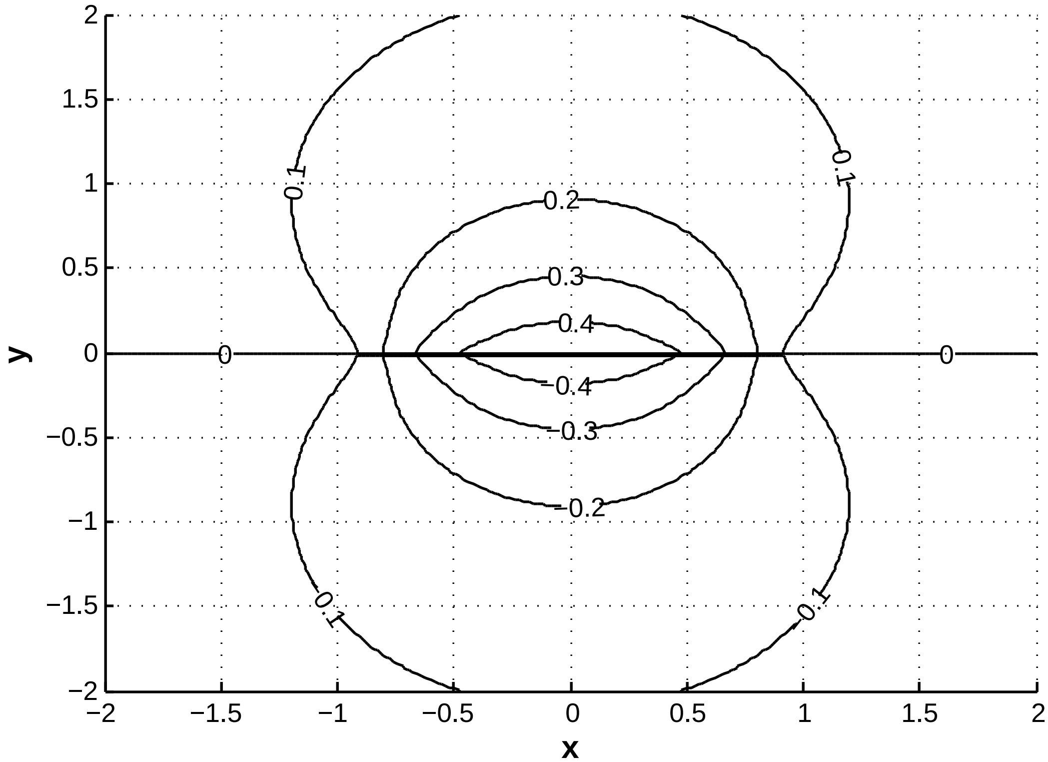

(a) Body Displacement

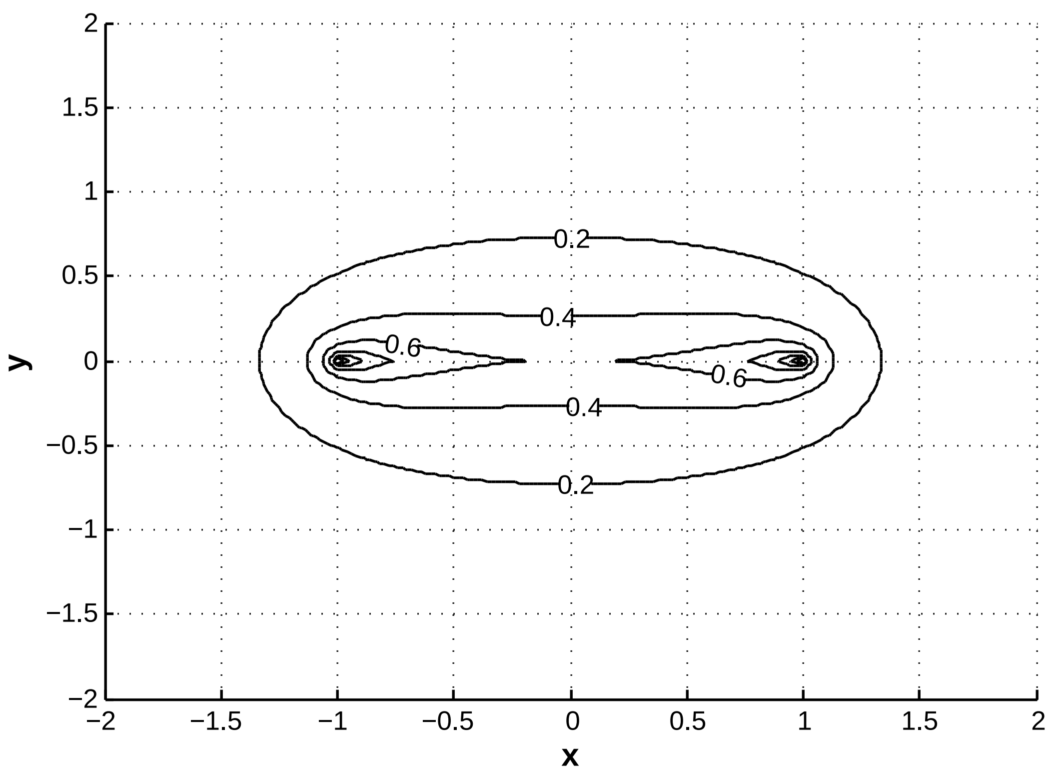

(b) Body Unit Stress Magnitude (τ)

Figure 6.17: Displacement and Unit Stress Magnitude in Body Material ($\tilde{P} = -1$, $\gamma = 0.5$, $N = 128$)

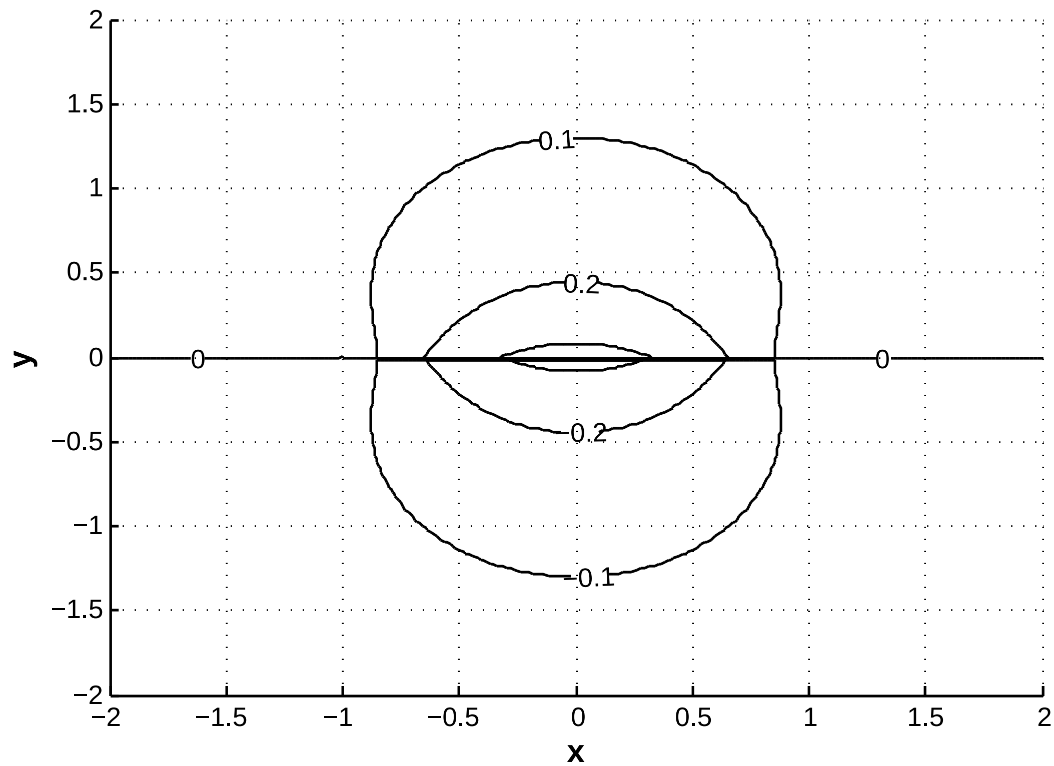

(a) Body Displacement

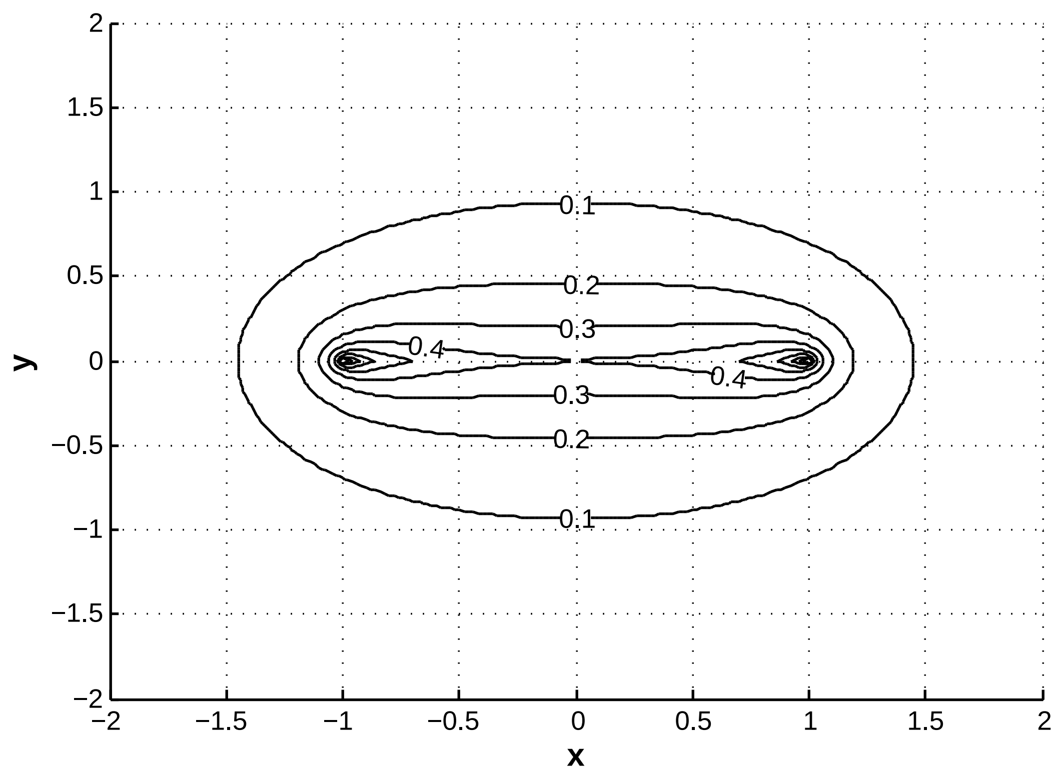

(b) Body Unit Stress Magnitude (τ)

Figure 6.18: Displacement and Unit Stress Magnitude in Body Material ($\tilde{P} = -1,\ \gamma = 1,\ N = 128$)

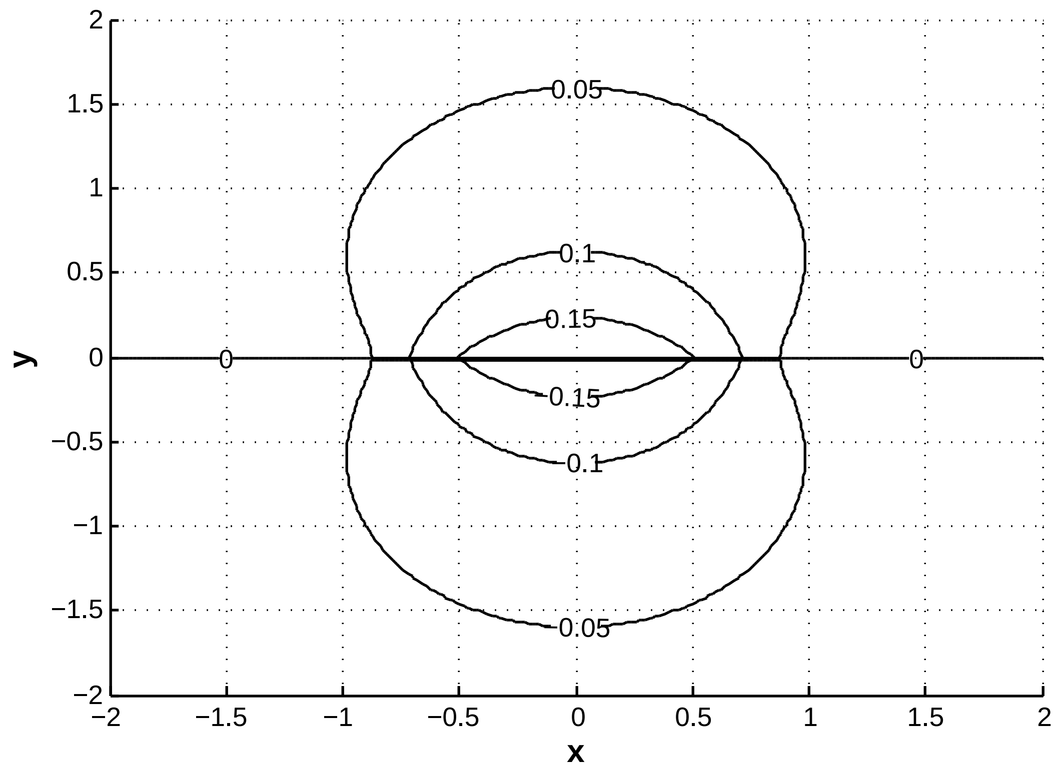

(a) Body Displacement

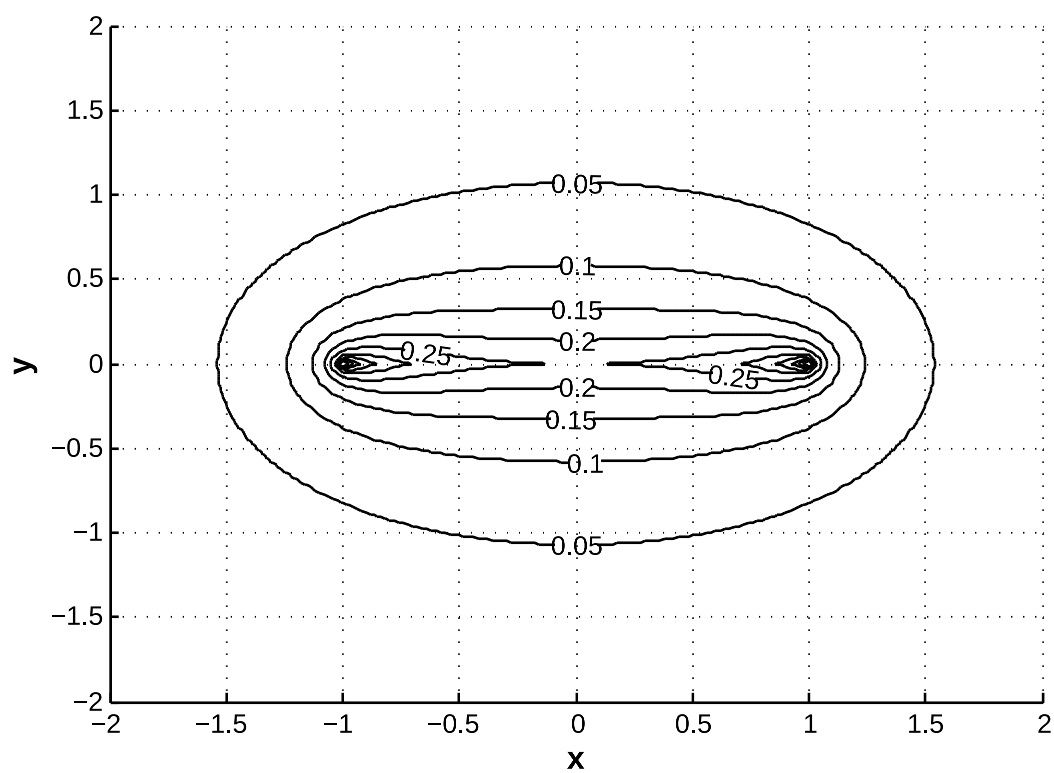

(b) Body Unit Stress Magnitude (τ)

Figure 6.19: Displacement and Unit Stress Magnitude in Body Material ($\tilde{P} = -1$, $\gamma = 2$, $N = 128$)

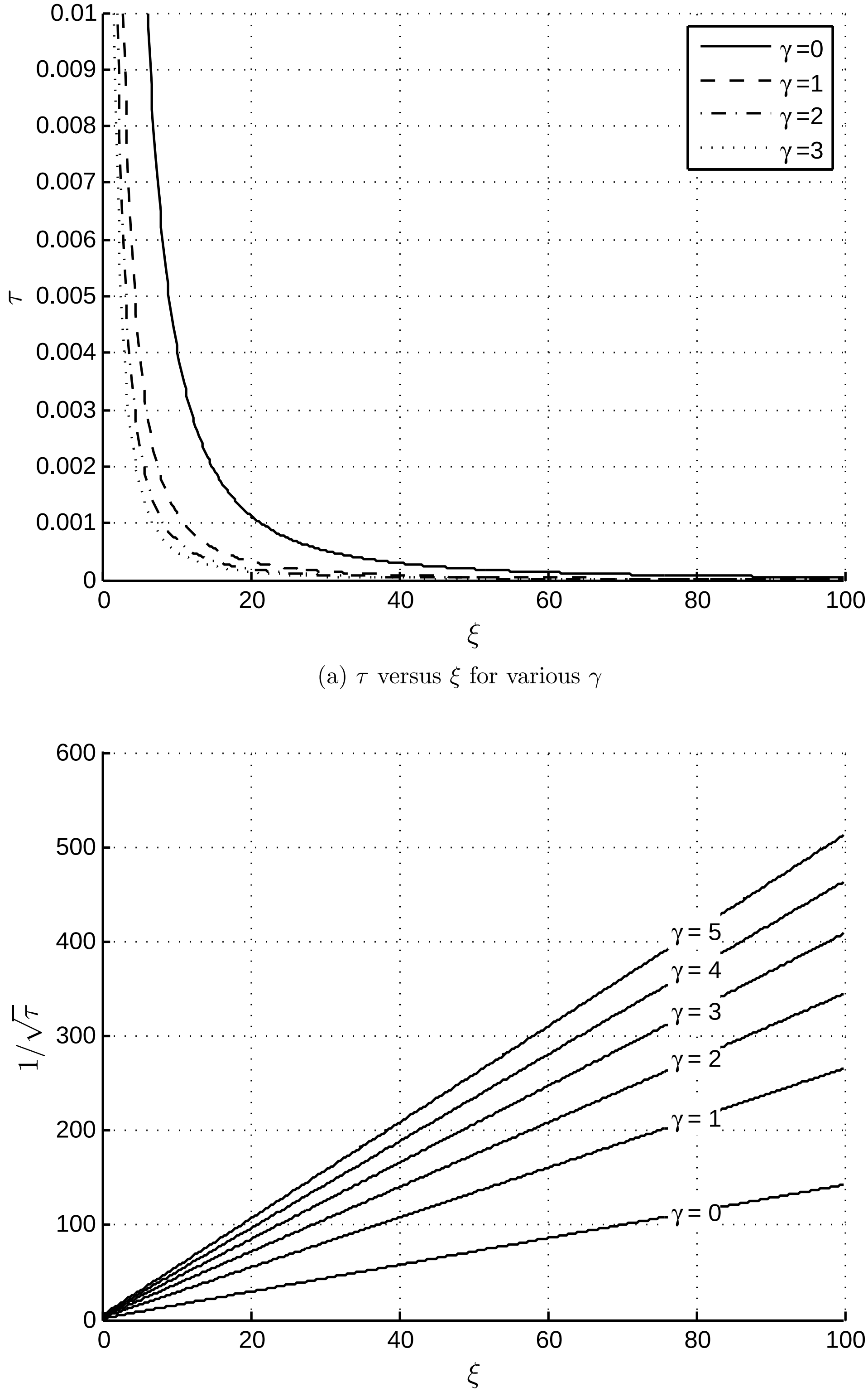

(a) τ versus ξ for various γ

(b) $1/\sqrt{\tau}$ versus ξ for various γ

Figure 6.20: Effect of γ on the Stress Outside a Crack Tip

and ignoring the regions close to the crack (in this data set, all values with $\xi > 1$ were used) provides linear approximations in the form:

$$\frac{1}{\sqrt{\tau}} \simeq m\xi + b \tag{6.3.9}$$

Figure 6.21 shows the squared values of m and b plotted against γ. These linearized plots produced R^2 values of 0.99999 for both m and b. Hence, m and b as functions of γ are approximated to be:

$$m(\gamma) \simeq \sqrt{4.7270\gamma + 2.1906}$$
$$b(\gamma) \simeq \sqrt{4.6078\gamma + 2.1288}$$

Define the Unit Radius of Effect ($\overline{R}$) as the distance from the origin with a given maximum stress magnitude - which in the present case can be found on the x axis, hence:

$$\overline{R}(\tau) \equiv \xi + 1 \tag{6.3.10}$$

Using the approximations for m and b and solving for τ and ξ in Equations 6.3.9 and 6.3.10 respectively yields an approximation for maximum unit stress magnitude at any given unit radius ($\overline{R} > 2$):

$$\tau(\overline{R}) \simeq \frac{1}{\left((\overline{R}-1)\sqrt{4.7270\gamma + 2.1906} + \sqrt{4.6078\gamma + 2.1288}\right)^2} \tag{6.3.11}$$

Alternatively, this equation can be inverted (for $\overline{R}$) to estimate the radial extent of a given unit stress magnitude, such that:

$$\overline{R}(\tau) \simeq \frac{1}{\sqrt{\tau\,(4.7270\gamma + 2.1906)}} - \sqrt{\frac{4.6078\gamma + 2.1288}{4.7270\gamma + 2.1906}} + 1$$

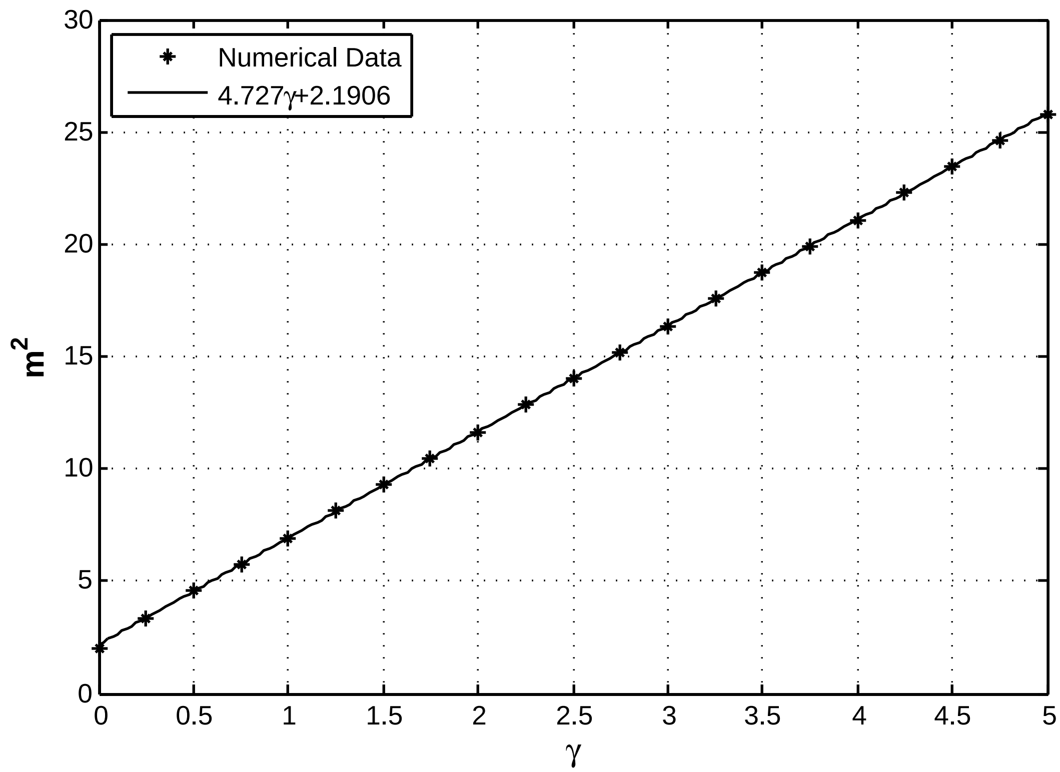

(a) Linear Slope of Stress Radius Versus γ

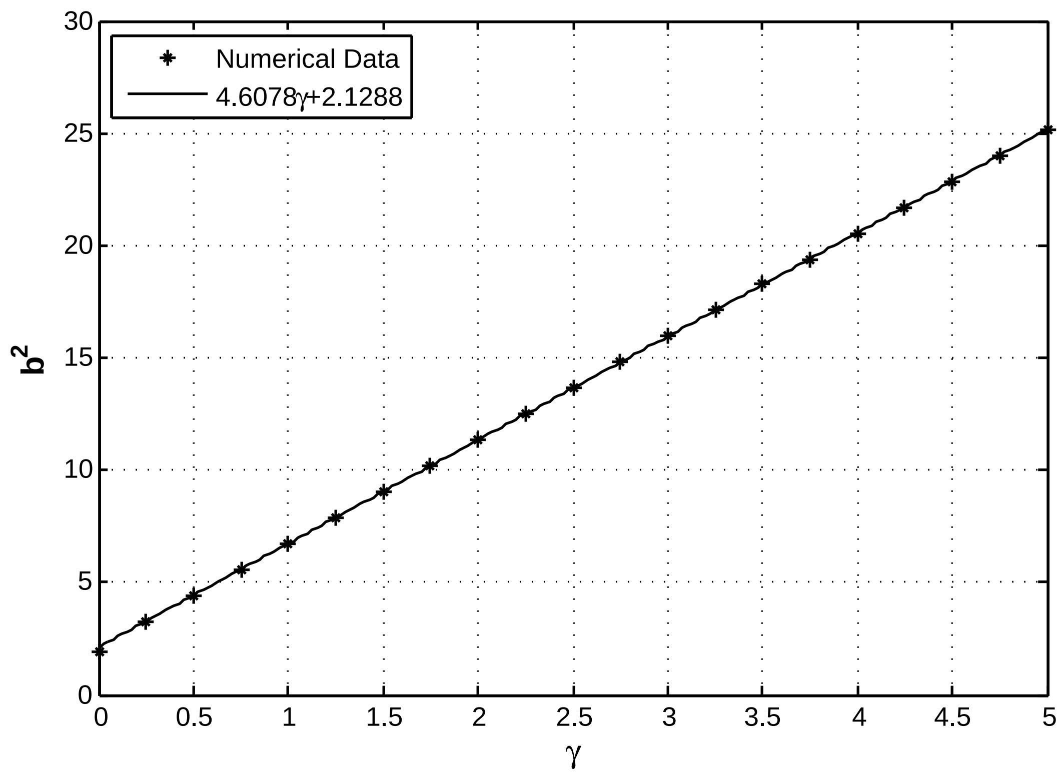

(b) Linear Intercept of Stress Radius Versus γ

Figure 6.21: Curve Fit Coefficients From the Effect of γ on the Stress Outside a Crack Tip

Note that the ratio of b/m is always approximately 1 (within 0.02), so this expression can be simplified further:

$$\overline{R}(\tau) \simeq \frac{1}{\sqrt{\tau\,(4.7270\gamma + 2.1906)}} \tag{6.3.12}$$

Since $\overline{R} > 2$, to use the approximation in Equation 6.3.12 it is required that:

$$\tau < \frac{1}{m^2 + b^2 + 2mb} < \frac{1}{9.3348\gamma + 4.3194} \tag{6.3.13}$$

6.4 Numerical Convergence and Accuracy

The numerical solutions of integral Equations 4.4.15 and 4.4.16 were computed using an increasing number of elements to show convergence. Convergence plots for the values of θ_{max} and θ'_{max} with a constant stress input are shown in Figure 6.22, where the number of elements was increased in each run by powers of 2 ($N = 2, 4, 8, 16, \ldots, 4096$).

Figure 6.22a shows a trend for $\theta(0)$ ($\equiv \theta_{max}$) with increasing N (the number of elements) using different values of the surface effect parameter (γ). These approximations all showed stiff convergence with less than 50 elements.

Refinement convergence of the slope at the endpoints ($\theta'(-1) \equiv \theta'_{max}$) is shown in Figure 6.22b. There is convergence here, however more elements are required as the surface parameter decreases in value. This makes sense because as the surface parameter goes to zero (the classical model) the stresses on the crack tips (which is linearly proportional to the slope) becomes infinite - see Equation 6.1.10. This leads to the introduction of two accuracy refinement parameters (Υ and Υ' for $\theta(x)$ and $\theta'(x)$ respectively) which

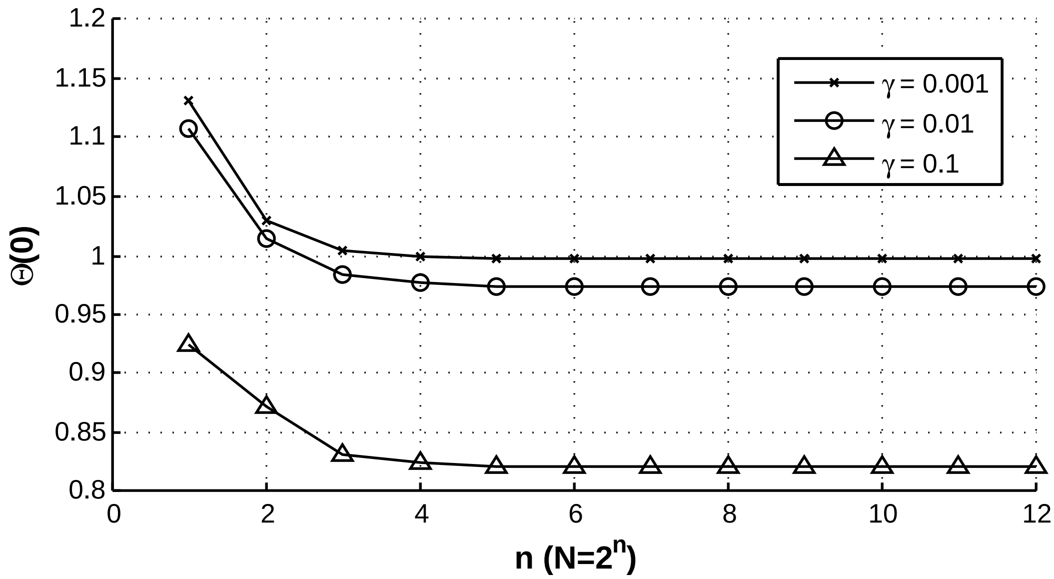

(a) Numerical Convergence of the point $\theta(0)$ using h-refinement

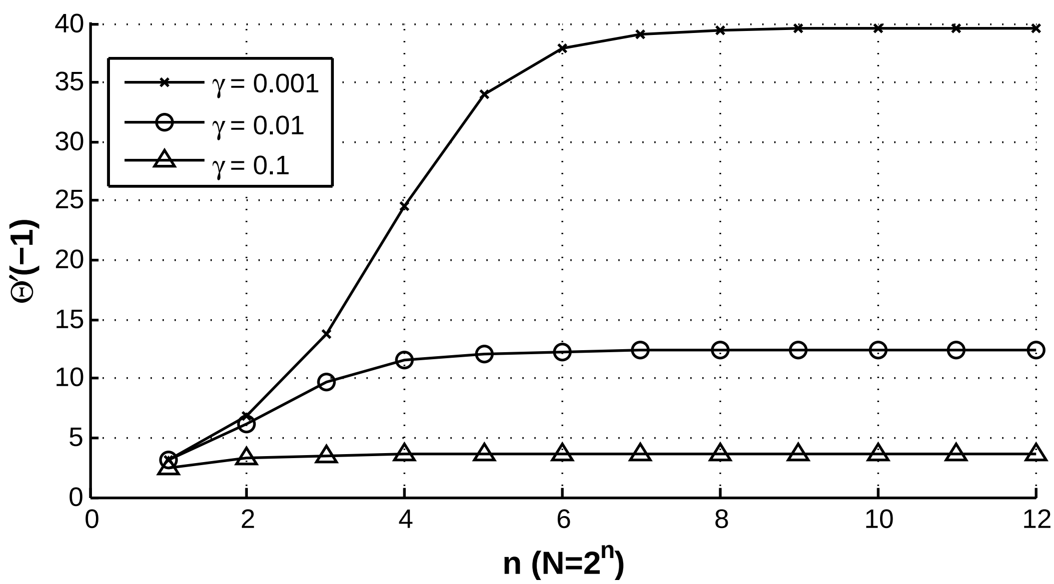

(b) Numerical Convergence of the point $\theta'(-1)$ using h-refinement

Figure 6.22: Numerical Convergence With Constant Stress Input ($\tilde{P} = -1$) and various values of γ.

represent the desired accuracy in percent. Define relative error between approximations for $\theta(x)$ and $\theta'(x)$ as $\tilde{\varepsilon}$ and $\tilde{\varepsilon}'$ respectively:

$$\tilde{\varepsilon}(n) \equiv \left| \frac{\mathbf{\Theta}_{MAX}(N = 2^{n+1}) - \mathbf{\Theta}_{MAX}(N = 2^{n})}{\mathbf{\Theta}_{MAX}(N = 2^{n+1})} \right| \tag{6.4.1}$$

$$\tilde{\varepsilon}'(n) \equiv \left| \frac{\mathbf{\Theta}'_{MAX}(N = 2^{n+1}) - \mathbf{\Theta}'_{MAX}(N = 2^{n})}{\mathbf{\Theta}'_{MAX}(N = 2^{n+1})} \right| \tag{6.4.2}$$

Then, simply refine the element size until the desired accuracy is reached, or when $\tilde{\varepsilon} < \Upsilon$ and $\tilde{\varepsilon}' < \Upsilon'$. An example plot is shown in Figure 6.23a, which shows the number of elements used to calculate the maximum slope in the computation of Figure 6.15 with $\Upsilon' = 0.1\%$.

The adjusted stress input function ($\theta_y(x)$) never converges numerically at the endpoints, which is expected (and proven in Section 4.4). However, away from the crack tips the values are convergent. Insight can be found by evaluating the function $\theta''(x)$ (which is linearly proportional to $\theta_y(x)$). In order to explore convergence of the function $\theta''(x)$ in a controlled manner, again the Heaviside Step function is used. Figure 6.23b shows plots of refinement on the cusp (previously plotted in Figure 6.11a). Similar to the values of $\theta'(x)$, convergence of it's derivative is slower and heavily dependent on γ. Beyond 4096 elements was not possible due to lack of computer memory.

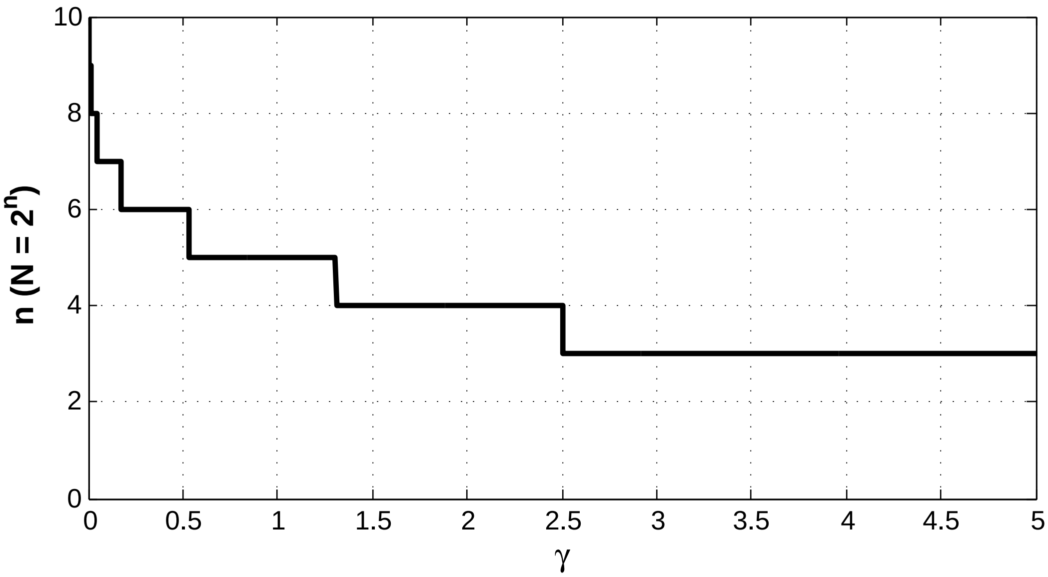

(a) Number of elements ($N = 2^n$) required for convergence of θ'_{max} versus surface effect parameter (γ) with error ($\tilde{\varepsilon}'$) less than 0.1% and constant input stress load ($\tilde{P} = \pm 1$)

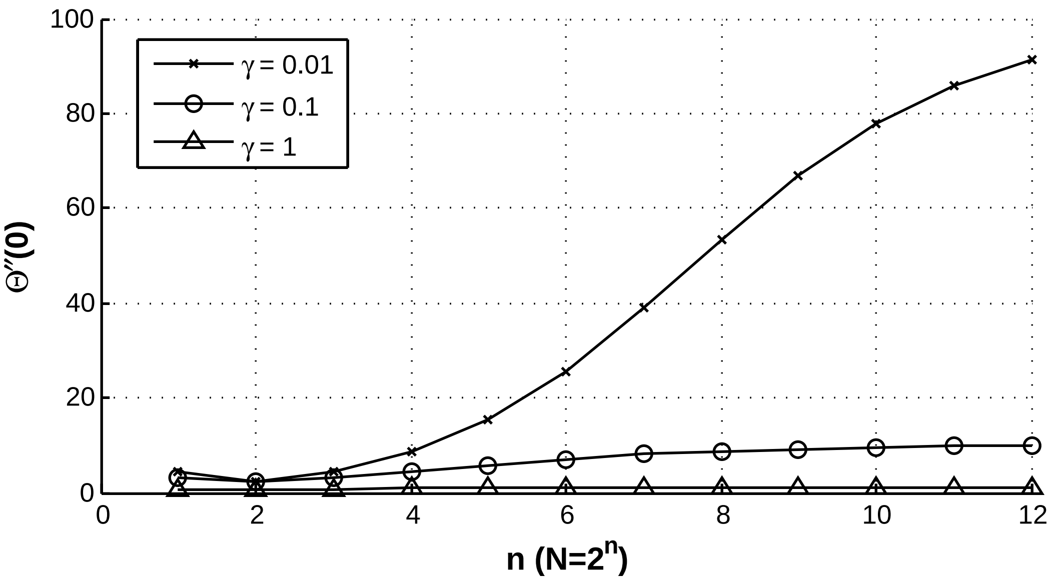

(b) Convergence Tests for $\theta''(0)$ ($\theta_y(x) = \tilde{P}(x) - \gamma\theta''(x)$) near the cusp of a Heaviside Step Function input.

Figure 6.23: Accuracy of θ'_{max} and Convergence of θ_y on the Crack Face

Part IV

Conclusions

7 - Conclusions

This chapter summarizes the contributions, applicable conclusions and shortcomings of the models formulated in this study.

7.1 Boundary Value Problem

The anti-plane displacement problem given in Equations 3.3.7 through 3.3.9:

$$\begin{aligned}
&\frac{\partial^2 w}{\partial x_1^2}+\frac{\partial^2 w}{\partial x_2^2}=0 && \text{in } \mathbb{R}^2\backslash L\\
&\mu\frac{\partial w}{\partial x_2}^{\pm}=P(x_1)\mp\beta\frac{\partial^2 w}{\partial x_1^2}^{\pm} && \text{on } L\\
&\left|\frac{\partial w}{\partial \boldsymbol{n}}\right|\to 0 && \text{as } |x|\to\infty
\end{aligned}$$

Has a unique solution and is well posed. Given this, the dimensionless equivalent problem in Equations 3.5.7 through 3.5.9 is also well posed since the transformations in Section 3.5 are all invertible for any point of interest. Setting the surface effect constant (β) to zero (or $\gamma \to 0$) collapses the boundary value problem to the classical case given by Equations 3.2.7 through 3.2.9.

The displacement on the crack face is found to be the solution ($\theta(x)$) of the Fredhholm Integral Equation 4.4.16. The derivatives of $\theta(x)$ ($\theta'(x)$ and $\theta''(x)$) are the solutions of the similar Fredholm Equations 4.4.15 and 4.4.21.

The x and y gradient components on the crack face are given as the functions $\theta'(x)$ and $\theta_y(x)$ respectively and these functions are linearly proportional to the stresses (σ_{13} and σ_{23}) along the crack face. The y component of the displacement gradient on the crack face is also linearly proportional to the function $\theta''(x)$ and is given by Equation 4.4.20. The full system of equations is given below:

$$\begin{aligned}
&\gamma\theta(x) - \frac{1}{\pi}\int_L \theta(t)\ln|t-x|dt = \zeta_2(x) - C_1 x - C_2 \\
&\gamma\theta'(x) - \frac{1}{\pi}\int_L \theta'(t)\ln|t-x|dt = \zeta_1(x) - C_1' \\
&\gamma\theta''(x) - \frac{1}{\pi}\int_L \theta''(t)\ln|t-x|dt = \tilde{P}(x) - \left[\frac{1}{\pi}\theta'(t)\ln|t-x|\right]_{t=-1}^{t=1} \\
&\theta_y(x) = \tilde{P}(x) - \gamma\theta''(x)
\end{aligned}$$

Where the constants C_1, C_1' and C_2 require the crack tip and anti-symmetric conditions from Equations 4.4.17 and 4.4.18:

$$\begin{aligned}
&\theta(-1) = \theta(1) = 0 \\
&\int_{-1}^{1} \theta'(x)dx = 0
\end{aligned}$$

The unit displacement and gradient components in the body material are given by Equations 4.5.4, 4.5.5 and 4.5.6:

$$\begin{aligned}
u(x,y) &= \mathfrak{Im}\left\{\frac{1}{\pi}\int_L \frac{\theta(t)}{t-z}dt\right\} \\
\frac{\partial u}{\partial x}(x,y) &= \mathfrak{Im}\left\{\frac{1}{\pi}\int_L \frac{\theta'(t)}{t-z}dt\right\} \\
\frac{\partial u}{\partial y}(x,y) &= \mathfrak{Re}\left\{\frac{1}{\pi}\int_L \frac{\theta'(t)}{t-z}dt\right\}
\end{aligned}$$

Where the complex coordinate $z \equiv x + iy$. The final solution then requires the inverse transformations from Section 3.5, where:

$$
\begin{aligned}
w(x_1, x_2) &= \frac{aP_o}{\mu} u(x, y) = \frac{aP_o}{\mu} u(x_1/a, x_2/a) \\
\sigma_{13}(x_1, x_2) &= P_o \frac{\partial u}{\partial x}(x_1/a, x_2/a) \\
\sigma_{23}(x_1, x_2) &= P_o \frac{\partial u}{\partial y}(x_1/a, x_2/a)
\end{aligned}
$$

7.2 Approximations from This Study

The magnitude of unit displacement anywhere across the crack can be approximated using Equation 6.3.5:

$$\theta(x) \simeq \frac{(1 - x^2)^{\left(\frac{2m\gamma+1}{2m\gamma+2}\right)}}{2\gamma + 1}$$

For the actual displacement use the transformation relation from Equation 3.5.6, such that:

$$w(x_1, 0^+) \simeq a \left(\frac{P_o}{\mu}\right) \frac{(1 - (x_1/a)^2)^{\left(\frac{2m\gamma+1}{2m\gamma+2}\right)}}{2\gamma + 1}, \qquad |x_1| \leq a \qquad (7.2.1)$$

This approximation has less than 5% error in the range of $\gamma \leq 5$ and can be used as a quick estimate of crack shape with a constant stress input.

The maximum magnitude of $\theta'(x)$ is on the crack tips ($\theta'_{max} = \theta'(\pm 1)$) and is finite. With a constant stress input, the value of θ'_{max} follows the inequality relation from Equation 6.3.7:

$$\theta'_{max} \geq \frac{1}{1.0057\gamma + 0.2863}$$

Using the inverse transformation from Section 3.5, it is concluded that the maximum opposing shear stress ($\sigma_{13,max}$) at the crack tips ($x_1 = \pm a$) for a constant load input ($\sigma_{23}(x,0) = \pm P_o$) is:

$$\sigma_{13,max} \geq \frac{P_o}{1.0057\gamma + 0.2863} = \frac{aP_o\mu}{1.0057\beta + 0.2863a\mu} \tag{7.2.2}$$

When $\gamma \geq 1$ the relation above becomes a more precise approximation and the inequality becomes an equality.

The maximum unit shear stress magnitude (τ) at a distance outside the crack can be approximated using Equation 6.3.11:

$$\tau(\overline{R}) \simeq \frac{1}{\left((\overline{R}-1)\sqrt{4.7270\gamma + 2.1906} + \sqrt{4.6078\gamma + 2.1288}\right)^2}$$

Using the inverse transformation from Section 3.5 again, $|\boldsymbol{\sigma}| \equiv P_o\tau$ and $R_s \equiv a\overline{R}$, which yields:

$$|\boldsymbol{\sigma}|(R_s) \simeq \frac{P_o}{\left[(R_s/a - 1)\sqrt{4.7270\gamma + 2.1906} + \sqrt{4.6078\gamma + 2.1288}\right]^2} \tag{7.2.3}$$

Where: $R > 2a$. To find the radius outside a crack with a given maximum shear stress magnitude, use the same transformations from Section 3.5 and the relation from Equation 6.3.12:

$$R_s(|\boldsymbol{\sigma}|) \simeq \frac{a\sqrt{P_o}}{\sqrt{|\boldsymbol{\sigma}|\,(4.7270\gamma + 2.1906)}} \tag{7.2.4}$$

Which is an accurate estimate of the radius in the plane for a given maximum stress when:

$$|\boldsymbol{\sigma}| < \frac{P_o}{9.3348\gamma + 4.3194} \tag{7.2.5}$$

7.3 Summary of Surface Effect Model

The physics of the GM model was interpreted as follows:

1. Energy is dispersed on the boundary, reducing the input shear stress (compare the functions θ_y to $\tilde{P}$). This can be seen in Figures 6.4, 6.6, 6.8, 6.10 and 6.11a. In each case (with exception of the region near the crack tips) the adjusted input stress magnitude shows a reduction when γ increases. The singularities on the crack tips are already there in the classical model, however this model does not have a jump discontinuity from the value of input stress ($\tilde{P}$) to $\pm\infty$ like the classical case.

2. From this reduction of input shear stress, the displacement (w) and opposing stress (σ_{13}) are reduced and finite across the crack face. Figures 6.3, 6.5, 6.7, 6.9 and 6.11a show this trend conclusively for both displacement ($\theta \propto w$) and slope ($\theta' \propto \sigma_{13}$).

3. The displacements and stress magnitudes are also reduced. This can be seen in Figures 6.16 through 6.19.

4. With the presence of the surface effect, the radius of effect in the body material is also reduced.

It is assumed that the GM model is not "adding in" another element to the model, but it does not ignore surface effects. Given the convergent plots in Figures 6.22 and 6.23b, it is apparent that the function $\theta(x)$ along with it's derivatives $\theta'(x)$ and $\theta''(x)$ are convergent across the crack face. The function $\theta''(x)$ does not converge near the crack tips, however all three functions showed a reduction and convergence across the crack tip when γ increased. Comparing this to the classical model (without surface effects), it is concluded that the GM model is more stable and convergent.

7.4 Effect of Input Parameters

Using the relationships and approximations from the previous sections, the effects of various input parameters (all defined as constants in the boundary value problem) are quantified. Table 7.1 provides a summary of the effect on displacement, stresses, strains and radius of effect as each input parameter is increased. If the input parameter is decreased, simply reverse the trends given in the table.

Table 7.1: Effect of Parameters on Displacement, Stresses, Strains and Radius of Effect

	Description	w	σ	ϵ	R_s
$\gamma \uparrow$	Surface Parameter	$\downarrow$	$\downarrow$	$\downarrow$	$\downarrow$
$a \uparrow$	Half Crack Length	$\uparrow$	$\uparrow$	$\uparrow$	$\uparrow$
$\beta \uparrow$	Surface Effect Constant	$\downarrow$	$\downarrow$	$\downarrow$	$\downarrow$
$\mu \uparrow$	Modulus of Rigidity	$\downarrow$	$\uparrow$	$\downarrow$	$\uparrow$
$P_o \uparrow$	Input Stress Value (RMS)	$\uparrow$	$\uparrow$	$\uparrow$	$\uparrow$

8 - Suggested Future Work

This chapter is a discussion of possible model refinements and future problems of interest.

8.1 Clamped Ends and Natural Boundary Condition

The dimensionless boundary value problem from Equations 3.5.7 through 3.5.9 has the equivalent form:

$$\frac{\partial^2 u}{\partial x^2} + \frac{\partial^2 u}{\partial y^2} = 0 \qquad \text{in } A(= \mathbb{R}^2 \backslash L) \tag{8.1.1}$$

$$\frac{\partial u}{\partial \boldsymbol{n}} = \tilde{P}(x) - \gamma \frac{\partial^2 u}{\partial x^2} \qquad \text{on } L \tag{8.1.2}$$

$$\left| \frac{\partial u}{\partial \boldsymbol{n}} \right| \to 0 \qquad \text{on } \Gamma_\infty \tag{8.1.3}$$

Where the total boundary is $\partial A = L \bigcup \Gamma_\infty$. Multiplying each equation by the solution (u) and integrating yields a form of the energy residual equation:

$$\int_A u \nabla \cdot (\nabla u) \, dA - \int_L u \left(\frac{\partial u}{\partial \boldsymbol{n}} - \tilde{P} + \gamma \frac{\partial^2 u}{\partial x^2} \right) ds - \int_{\Gamma_\infty} u \frac{\partial u}{\partial \boldsymbol{n}} ds = 0 \tag{8.1.4}$$

Using the divergence theorem:

$$\int_A u \nabla \cdot (\nabla u) \, dA = \int_{\partial A} u \frac{\partial u}{\partial \boldsymbol{n}} ds - \int_A |\nabla u|^2 \, dA$$

$$\int_L u \frac{\partial^2 u}{\partial x^2} ds = \pm \left[u \frac{\partial u}{\partial x} \right]_L - \int_L \left(\frac{\partial u}{\partial x} \right)^2 ds$$

After simplification, this yields the result:

$$\int_A |\nabla u|^2 \, dA - \int_L u\tilde{P} ds - \gamma \int_L \left(\frac{\partial u}{\partial x} \right)^2 ds \pm \gamma \left[u \frac{\partial u}{\partial x} \right]_L = 0 \qquad (8.1.5)$$

This is similar to the finite element weak form [29, 30] and implies the natural boundary conditions [33] at the crack tips:

$$\lim_{x \to \pm 1} \left(u \frac{\partial u}{\partial x} \right) = 0 \qquad (8.1.6)$$

Which suggest that the BVP has two separate natural boundary conditions at the crack tips (four combinations in total). In the problem studied in this work, it was assumed that $u(\pm 1, 0) = 0$ due to the condition $u^+ = -u^-$. However, a crack with a clamped end would require the displacement gradient ($\frac{\partial u}{\partial \boldsymbol{n}}$) at the endpoint to be zero. Kim et el. solved a similar problem of this work for the stresses (with surface effects) utilizing the boundary condition $\frac{\partial u}{\partial x}(\pm 1, 0) = 0$ [9, 10] to achieve finite stresses everywhere.

The convergence of the adjusted unit input shear stress (θ_y) at the crack tips was not possible using the displacement conditions $u(\pm 1, 0) = 0$. However, using the condition that the slopes are zero at the crack tips ($\frac{\partial u}{\partial x}(\pm 1, 0) = \theta'(\pm 1) = 0$) should yield stable and convergent results. Recall Equations 4.4.21 and 4.4.20 from Section 4.4:

$$\gamma \theta''(x) - \frac{1}{\pi} \int_L \theta''(t) \ln |t - x| dt = \tilde{P}(x) - \frac{1}{\pi} \, \theta'(t) \ln |t - x| |_{t=-1}^{t=1}$$

$$\theta_y(x) \equiv \frac{\partial u}{\partial y}(x, 0^+) = \tilde{P} - \gamma \theta''(x)$$

If the values of $\theta'(\pm 1) \to 0 + O(x)$, then:

$$\lim_{t \to \pm 1} \theta'(t) \ln |t - x| = 0$$

Given this, the solution of $\theta''(x)$ should be stable and convergent at the crack tips, leading to the conclusion of finite stress magnitudes on the crack tips.

When evaluating the two problems with clamped and un-clamped conditions, Vardoulakis et. al concluded that solutions were more convergent in the clamped case [13] (or when $\frac{\partial u}{\partial \boldsymbol{n}}(\pm 1, 0) = 0$). It would be of interest to formulate the clamped problem using the GM model used in this work to see how it compares to Vardoulakis' findings (which utilized a different surface energy model) and how the crack face (and body) displacement changes with the clamped condition.

8.2 Realistic Values of γ for Various Materials

The surface parameter (defined in Equation 3.5.10) is:

$$\gamma \equiv \frac{\mu^s - \sigma_o}{a\mu}$$

Recall the transformation from Equation 2.3.8, being:

$$\mu^s = \mu \hat{h}$$

Knowledge of both the lattice spacing (the interface layer thickness $\hat{h}$ is approximately 1 to 2 times the lattice spacing) and the surface tension (σ_o) are outstanding requirements to determine appropriate values of the surface parameter. Molecular dynamics simulations could be done in order to estimate these values for various materials. Once this information is obtained, physical tests could be done in order to verify the results in this work. Alternatively, using precise instruments one could experimentally determine the surface parameter for a particular case by using approximation in Equation 6.3.5 and transformation in Equation 3.5.10.

As a first hypothesis to this study, assuming surface tension is negligible (or that $\sigma_o \ll \mu^s$) then:

$$\gamma \simeq \frac{\mu^s}{a\mu} = \frac{\hat{h}}{a}$$

If the crack length is of the order of millimeters ($10^{-3}m$) and the lattice spacing is of the order of angstrom ($10^{-10}m$), then a value of γ in the range of 10^{-7} is reasonable.

8.3 Analytical Solutions

Section 6.1 is a review of the classical problem and it's known analytical solution. Using a similar idea from Sections 4.3 and 4.4, the problem could be posed by defining the following:

$$[\phi'(t)]^+ + [\phi'(t)]^+ \equiv h(t) \tag{8.3.1}$$

$$[\phi''(t)]^+ - [\phi''(t)]^+ \equiv k(t) \tag{8.3.2}$$

Which have the known solutions [21, 19]:

$$\phi'(z) = \frac{1}{2\pi i} \int_L \sqrt{\frac{t^2-1}{z^2-1}} \left(\frac{h(t)}{t-z} \right) dt \tag{8.3.3}$$

$$\phi''(z) = \frac{1}{2\pi i}\int_L \frac{k(t)}{t-z}dt \tag{8.3.4}$$

Using the boundary condition from Equation 4.2.9, the following relation is found:

$$ih(t) + \gamma k(t) = 2\tilde{P}(t) \tag{8.3.5}$$

Also note that:

$$\frac{d}{dz}\left(\frac{1}{(t-z)\sqrt{z^2-1}}\right) = \frac{2z^2 - tz - 1}{(t-z)^2 (z^2-1)^{\frac{3}{2}}} \equiv \zeta(t,z) \tag{8.3.6}$$

Using this result, another form of the function $\phi''(z)$ is:

$$\phi''(z) = \frac{1}{2\pi i}\int_L h(t)\zeta(t,z)\sqrt{t^2-1}dt \tag{8.3.7}$$

Using Equation 8.3.4 and the Localization Theorem [28], a second relation between h and k is:

$$h(t)\zeta(t,z)\sqrt{t^2-1} - \frac{k(t)}{(t-z)} = 0 \tag{8.3.8}$$

Using Equations 8.3.5 and 8.3.8, $h(t)$ and $k(t)$ are determined to be:

$$k(t) = \frac{2\tilde{P}(t)\zeta(t,z)(t-z)\sqrt{t^2-1}}{i + \gamma\zeta(t,z)(t-z)\sqrt{t^2-1}} \tag{8.3.9}$$

$$h(t) = \frac{2\tilde{P}(t)}{i + \zeta(t,z)(t-z)\sqrt{t^2-1}} \tag{8.3.10}$$

Plugging these back into Equations 8.3.3 and 8.3.4 yields the direct expressions for $\phi'(z)$ and $\phi''(z)$:

$$\phi'(z) = \frac{1}{2\pi i}\int_L \sqrt{\frac{t^2-1}{z^2-1}}\left(\frac{2\tilde{P}(t)}{i+\gamma\zeta(t,z)\,(t-z)\,\sqrt{t^2-1}}\right)\frac{dt}{t-z} \tag{8.3.11}$$

$$\phi''(z) = \frac{1}{2\pi i}\int_L \left(\frac{2\tilde{P}(t)\zeta(t,z)\sqrt{t^2-1}}{i+\gamma\zeta(t,z)\,(t-z)\,\sqrt{t^2-1}}\right)dt \tag{8.3.12}$$

Integrate Equation 8.3.11 to get $\phi(z)$:

$$\phi(z) = \int_0^z \phi'(s)ds + C_1 \tag{8.3.13}$$

Which yields a final solution for displacement anywhere in the body:

$$u(x,y) = \mathfrak{Re}\left\{\phi(z)\right\} = \mathfrak{Re}\left\{\int_0^z \phi'(s)ds\right\} + D_1 \tag{8.3.14}$$

Where D_1 is the real part of the complex constant C_1. Using the additional boundary condition $u(\pm 1, 0) = 0$, the constant D_1 represents a rigid body displacement and is zero in this case. Hence:

$$u(x,y) = \mathfrak{Re}\left\{\int_0^z \phi'(s)ds\right\} \tag{8.3.15}$$

Unfortunately, the expression in Equation 8.3.15 is not overly useful given the complexity of the integral. Also, the fact that the integral is singular eliminates the possibility of conventional numerical integration. It would be of interest to find an analytical solution using the method presented in this section, or something similar from the known works of Muskhelishvili [21, 19].

8.4 Other Problems of Interest

8.4.1 Bonded Surface Problems

The GM model could be used to formulate bonding problems. In this case, the bonding material would act as the interface layer and could be projected on the material surface. Three examples of some bonding problems which are slight modifications of the study in this work are shown in Figure 8.1.

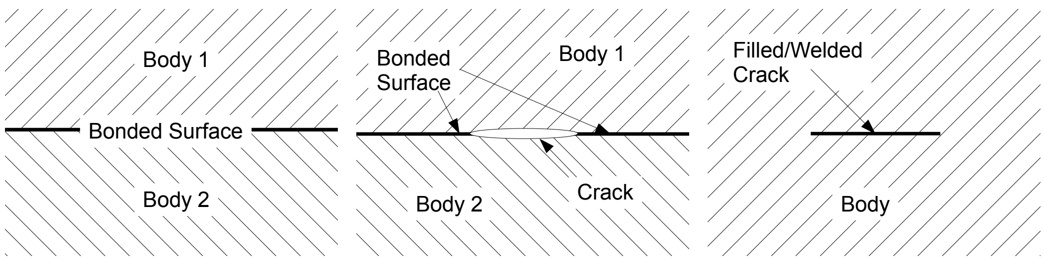

(a) Two body materials with different material characteristics bonded by some other material

(b) Two body materials with different material characteristics bonded by some other material and a crack

(c) Typical Crack problem, but with a bonding material, weld, repair, or glue on the crack

Figure 8.1: Plane Bonding Problems of Interest

The first example (Figure 8.1a) would consist of two different materials bonded with an interface layer. This interface layer could be modeled by projecting the properties of the tensile layer upon the boundaries, which is the same method used in this work.

Figure 8.1b shows two different materials bonded (like in the first example), but with a crack (or gap) in the bonding layer. This problem could be modeled with and without surface effects on the crack to predict failure (or tearing) of the bonding material under different stress loads.

A third problem of interest is where the crack has been "repaired" (Figure 8.1c). This would require determining realistic values of the surface parameter (γ), since a repair would make the crack surface much stiffer. A problem similar to the one posed in Figure 8.1c was posed and solved by Antipov and Shiavone [14] which yielded shapes and slope plots that were very similar to the problem posed in this work.

8.4.2 Three Dimensional Problem

In the formulation of the anti-plane/Mode-III displacement boundary value problem in Equations 3.3.7 through 3.3.9, it was assumed that the displacement (w) was not a function of the x_3 variable (or that thickness of the plane did not have an effect). If the problem is re-formulated using x_3 dependence, it would be of interest to know how this affects the stability and convergence of stresses and displacements using the GM model. Assuming such a model has a solution, a hypothesis is that the adjusted input stress component σ_{23} at the crack tip would be convergent numerically and definitively finite at the crack tips. Currently, this is the last outstanding issue with the planar model (and the solutions) presented in this work.

Unfortunately, dependence on the x_3 component eliminates the possibility of complex variable methods and would be much more difficult to solve analytically. However, a numerical model could be formulated for comparision.

8.4.3 Dynamic Problems

It is possible to use the GM model in dynamic plane wave propagation problems. This could be modeled similar to the anti-plane/Mode-III crack displacement case in this work, but with dynamic effects. Comparison to the classical case could be made and the effect of different surface parameters could be calculated. This would essentially be like adding a damping system to the surface of the crack. It would be of interest to note how different surface parameters would affect the natural frequency of the crack face and how this would change fatigue estimations near the crack tips. It would also be notable if the surface parameter changes any other effects, such as crack face modal shapes or possible sound emission from vibration.

Other dynamic problems, such as time dependence would also be of interest. Determining the effects of load velocity (such as a pulse stress or impact load) could bring clarity on impact type problems and how the GM model changes the results. This type of loading for the classical case was published by Broberg [32]. Taking a similar approach, but using the GM model could yield notable results.

Part V

References

Bibliography

[1] P. Chou and N. Pagano, *Elasticity; tensor, dyadic, and engineering approaches*. University series in basic engineering, Van Nostrand, 1967.

[2] I. Sokolnikoff, *Mathematical theory of elasticity*. R.E. Krieger Pub. Co., 1983.

[3] A. E. H. Love, *A Treatise on the Mathematical Theory of Elasticity*. Dover Publications, Inc., 2011.

[4] M. Gurtin, *An introduction to continuum mechanics*. Mathematics in science and engineering, Academic Press, 1981.

[5] A. H. England, *Complex Variable Methods in Elasticity*. Dover Publications, 2003.

[6] J. Wang, Z. Huang, H. Duan, S. Yu, X. Feng, G. Wang, W. Zhang, and T. Wang, "Surface stress effect in mechanics of nanostructured materials," *Acta Mechanica Solida Sinica*, vol. 24, no. 1, pp. 52 – 82, 2011.

[7] M. E. Gurtin and A. I. Murdoch, "A continuum theory of elastic material surfaces," *Arch. Ration. Mech. Anal.*, vol. 57, no. 4, 1975.

[8] M. E. Gurtin, "A general theory of curved deformable interfaces in solids at equilibrium," *Philosophical Magazine A-physics of Condensed Matter*

Structure Defects and Mechanical Properties, vol. 78, pp. 1093–1109, 1998.

[9] C. I. Kim, P. Schiavone, and C.-Q. Ru, "The effects of surface elasticity on an elastic solid with mode-iii crack: Complete solution," *Journal of Applied Mechanics*, vol. 77, no. 2, p. 021011, 2010.

[10] C. I. Kim, P. Schiavone, and C.-Q. Ru, "Analysis of a mode-III crack in the presence of surface elasticity and a prescribed non-uniform surface traction," *Zeitschrift Angewandte Mathematik und Physik*, vol. 61, pp. 555–564, June 2010.

[11] C. Q. Ru, "Simple geometrical explanation of Gurtin-Murdoch model of surface elasticity with clarification of its related versions," *Science in China G: Physics and Astronomy*, vol. 53, pp. 536–544, Mar. 2010.

[12] P. Sharma and S. Ganti, "Size-dependent eshelby's tensor for embedded nano-inclusions incorporating surface/interface energies," *Journal of Applied Mechanics*, vol. 71, 2004.

[13] I. Vardoulakis, G. Exadaktylos, and E. Aifantis, "Gradient elasticity with surface energy: mode-iii crack problem," *International Journal of Solids and Structures*, vol. 33, no. 30, pp. 4531 – 4559, 1996.

[14] Y. A. Antipov and P. Schiavone, "Integro-differential equation for a finite crack in a strip with surface effects," *The Quarterly Journal of Mechanics and Applied Mathematics*, vol. 64, no. 1, pp. 87–106, 2011.

[15] M. Patricio Dias and R. Mattheij, "Crack propagation analysis," *CASA Report*, vol. 07, no. 23, 2007.

[16] L. Milne-Thompson, *Antiplane Elastic Systems.* Academic Press, 1962.

[17] C. Green, *Integral equation methods*. Applications of mathematics series, Nelson, 1969.

[18] R. Kress, *Linear integral equations*. Applied mathematical sciences, Springer-Verlag, 1989.

[19] N. Muskhelishvili and J. Radok, *Singular Integral Equations: Boundary Problems of Function Theory and Their Application to Mathematical Physics*. Dover Books on Physics Series, Dover Publications, 2008.

[20] J. Brown and R. Churchill, *Complex Variables and Applications*. Complex variables and applications, McGraw-Hill Professional, 2008.

[21] N. Muskhelishvili, *Some basic problems of the mathematical theory of elasticity: fundamental equations, plane theory of elasticity, torsion, and bending*. P. Noordhoff, 1963.

[22] L. M. Delves and J. L. Mohamed, *Computational Methods for Integral Equations*. London: Cambridge University Press, 1985.

[23] K. E. Atkinson, *A Survey of Numerical Methods for the Solution of Fredholm Integral Equations of the Second Kind*. Philadelphia, Pennsylvania: Society for Industrial and Applied Mathematics, 1976.

[24] P. Chadwick, *Continuum mechanics: concise theory and problems*. Dover books on physics, Dover Publications, 1999.

[25] P. A. Krutitskii, "The neumann problem in a 2-d exterior domain with cuts and singularities at the tips," *Journal of Differential Equations*, vol. 176, no. 1, pp. 269 – 289, 2001.

[26] P. A. Krutitskii and N. C. Krutitskaya, "The harmonic dirichlet problem in a planar domain with cracks," *AUPC SM Annales Academiae Paedagogicae Cracoviensis, Studia Mathematica*, vol. 7, 2008.

[27] J. Knowles and T. A. Pucik, "Uniqueness for plan crack problems in linear elastostatics," *Journal of Elasticity*, vol. 3, no. 3, 1973.

[28] J. Stewart, *Calculus*. Canada: Thomson Brooks/Cole, 6e ed., 2009.

[29] T. Hughes, *The finite element method: linear static and dynamic finite element analysis*. Dover Publications, 2000.

[30] J. Reddy, *An introduction to the finite element method*. McGraw-Hill series in mechanical engineering, McGraw-Hill, 1993.

[31] G. Sih, "Boundary problems for longitudinal shear cracks," *Proc. 2nd Conf. Theor. Appl. Mech.*, 1964.

[32] K. Broberg, "Crack expanding with constant velocity in an anisotropic solid under anti-plane strain," *International Journal of Fracture*, vol. 93, pp. 1–12, 1998. 10.1023/A:1007465705225.

[33] I. Gelfand, S. Fomin, and R. Silverman, *Calculus of variations*. Dover Books on Mathematics, Dover Publications, 2000.